THE ULTRA LOW TEMPERATURE
MAGNETIC SUSCEPTIBILITY OF COPPER
TETRAPHENYLPORPHINE USING A
He- He DILUTION REFRIGERATOR

Thesis for the Degree of Ph. D. MICHIGAN STATE UNIVERSITY JEFFERY L. IMES 1974 C.2



MICHIGAN STATE UNIVERSITY
DEPARTMENT OF PHYSICS
EAST LANSING, MICHIGAN

LIBRARY Michigan State University MSU

RETURNING MATERIALS:
Place in book drop to
remain his hackage from

#### ABSTRACT

# THE ULTRALOW TEMPERATURE MAGNETIC SUSCEPTIBILITY OF COPPER TETRAPHENYLPORPHINE USING A $$^3$He-$^4$He DILUTION REFRIGERATOR$

By

#### Jeffrey L. Imes

An investigation into the magnetic behavior of a class of dilute paramagnetic solids is presently in progress. The ultralow temperature magnetic susceptibility of several metalloporphyrin and metallo-tetraphenylporphyrin compounds has been measured using a  $^3\text{He}-^4\text{He}$  dilution refrigerator. This thesis reports the results obtained for the first of these compounds, copper  $\alpha,\beta,\gamma,\delta$  - tetraphenylporphine (CuTPP), to be studied in both powder and single crystal form. The apparatus and techniques used are also presented in detail.

The <sup>3</sup>He-<sup>4</sup>He dilution refrigerator is capable of reaching 8.4 mK in the continuous mode of operation and 4.0 mK in the "single-shot", non-continuous mode of operation. Its mixing chamber was constructed in a unique dual-tail arrangement which allows a powdered sample and a powdered CMN thermometer to be in good thermal equilibrium with each other. Careful thermal calibrations of the refrigerator indicate the temperature of the two tails agree to within .5% at 4.0 mK. Besides the two conventional ac mutual-inductance magnetometers there is also a Superconducting Quantum Interference

Device (SQUID) magnetometer mounted on the dilution refrigerator. Measurements of the susceptibility parallel and perpendicular to the c axis of aligned 1 mm<sup>3</sup> single crystals of CuTPP were made with this magnetometer. The future of SQUID magnetometers as a means of carrying single crystal measurements to ultralow temperatures seems very promising in light of our results.

The parallel susceptibility of CuTPP was found to obey a Curie-Weiss law with  $\theta_{\parallel \parallel}$  = -1.54 mK to about 20 mK. Curie-Weiss theta was determined from the intermolecular dipolar interaction by carrying out the appropriate lattice summations. The susceptibility perpendicular to the c axis is expected, on a theoretical basis, to be dominated by the hyperfine interaction between the copper electronic and nuclear spins. The experimentally measured perpendicular susceptibility indicates the presence of this type behavior. Both the parallel and perpendicular susceptibility crystal data were corrected for demagnetization effects. The demagnetizing factors were determined by utilizing a room temperature technique involving a mock-up of the crystal made from mild steel. The results obtained for the powder susceptibility to 4.0 mK show no indication of a transition to the ordered state. Comparison of the single crystal and powder data indicates thermal equilibrium between the crystals and the dilute solution was maintained down to approximately 12 mK.

### 

Ву

Jeffrey L. Imes

#### A THESIS

Submitted to
Michigan State University
in partial fulfillment of the requirements
for the degree

DOCTOR OF PHILOSOPHY

Department of Physics

#### DEDICATION

This thesis is dedicated to my wife, Dana, whose encouragement and assistance during its preparation were greatly appreciated.

#### **ACKNOWLEDGMENTS**

My sincere thanks go to Dr. William P. Pratt, Jr.
who effectively guided me to the completion of this thesis.
A very special thanks is extended to Gary L. Neiheisel
and Paul R. Newman for the considerable time and effort
they spent helping me gather the necessary experimental
data. I would also like to express my appreciation to
Dr. Jerry A. Cowen, Dr. Thomas A. Kaplan, and Dr. Robert
D. Spence for their advice and suggestions concerning
various aspects of this thesis. I am also very grateful
for the wonderful people in the Machine Shop who were so
helpful during the construction of the apparatus.

#### TABLE OF CONTENTS

Pa	age
LIST OF FIGURES	'i
LIST OF TABLES X	i
INTRODUCTION	1
Chapter	
I. THE EXPERIMENTAL APPARATUS	5
A. History of the Dilution Refrigerator:	
Solutions of $^3$ He in $^4$ He	5
B. Theory and Operation of a Dilution Refrigerator	11
C. Design and Operation of this Dilution	
Refrigerator	21
An Overview	21
The Condensor, Heat Exchanger, and Still	24
The Mixing Chamber	28
D. Measurements of Magnetic Susceptibility	40
The Conventional Magnetic Susceptibility Coils	40
The SQUID Magnetometer	52
E. Thermometry and Thermal Equilibrium within the	
	61
	61
•	63
Background Suscentibility Measurements	78

Chapter	Page
II. THE MAGNETIC SUSCEPTIBILITY OF COPPER	
TETRAPHENYLPORPHINE	87
A. A General Survey of the Porphyrins	87
B. Copper $\alpha, \beta, \gamma, \delta$ - Tetraphenylporphine	94
Introductory Remarks	94
Purification and Crystal Growth	95
The Structure of CuTPP	99
C. Theory of the Magnetic Susceptibility of	
Tetraphenylporphine	112
III. THE EXPERIMENTAL DATA	124
A. Presentation of the Experimental Results for	
CuTPP	124
B. Factors Affecting the Measurement of Magnetic	
Susceptibility at Ultralow Temperatures	133
Demagnetization Corrections	133
Thermal Equilibrium of Single Crystals	140
IV. AN ANALYSIS OF THE EXPERIMENTAL RESULTS	143
A. Comparison of Theory and Experiment	143
B. Summary and Conclusions	154
LIST OF REFERENCES	157
APPENDIX A	162
APPENDIX B	169
APPENDIX C	175
APPENDIX D	184

#### LIST OF FIGURES

Figure		Pag	е
1.	The phase separation diagram at saturated vapor pressure for ${}^{3}\text{He}^{-4}\text{He}$ mixtures. The dotted line represents the phase separation of a 28% solution of ${}^{3}\text{He}$ in ${}^{4}\text{He}$	•	8
2.	A schematic diagram of a He-4He dilution refrigerator indicating the flow of He through the various components	•	13
3.	The <sup>3</sup> He concentration of the still as a function of still temperature assuming the mixing chamber to be at a temperature of 0.0 K	•	18
4.	An overall view of the cryostat. The dilution refrigerator components are enclosed within a vacuum space and interconnected by capillary tubing which carries the flowing <sup>3</sup> He	•	23
5.	A detailed drawing of a sintered copper heat exchanger showing the flow of liquid helium	•	26
6.	A schematic drawing of the dual tail mixing chamber. The arrows represent the flow of <sup>3</sup> He through the mixing chamber. For clarity only the upper half of one of the magnetic susceptibility and lating them.		20
	bility coils is shown	•	30

Figure		Page
7.	Results of a theoretical calculation of the expected thermal relaxation time of a dual-tail mixing chamber. Closed circles represent heat conduction through the coil foil and mixing chamber walls. Open circles represent heat conduction via the liquid helium. The total relaxation time is represented by a dashed line.	33
8.	A detailed view of the sample chamber design	38
9.	A block diagram of the ac mutual inductance bridge circuit. All resistances are in ohms	42
10.	A detailed drawing of the dilution refrigerator and susceptibility coils. A = copper flange with lead fusewire "O"-ring; B = stainless steel support tube sealed in epoxy; C = SQUID mounting port; D = copper inner vacuum can connected to the still; E = copper to epoxy joint; F = coil foil	45
11.	A top view of the dilution refrigerator and susceptibility coils. The letters refer to parts which are similarly labeled in Figure 10	47
12.	A close-up view of the mutual inductance magnetic susceptibility coils detailing their construction	48
13.	A block diagram of the SQUID magnetometer circuit. The SQUID sensor and sample coil are located inside the cryostat	55
14.	The SQUID sample chamber and its means of attachment to the mixing chamber's dilute solution	

58

return line . .

Figure	Pa	ge
15.	The results of the calibration of a germanium resistance thermometer against the absolute temperature in the range .3 K to 3.0 K	65
16.	Results of temperature calibrations of the refrigerator using 100% CMN thermometers. Open circles: $M_1 = .55570$ gm CMN; $M_2 = .55555$ gm CMN. Closed circles: $M_1 = .555555$ gm CMN; $M_2 = .555570$ gm CMN. The subscripts refer to tail #1 or tail #2	68
17.	A comparison of the mixing chamber temperature as determined by 100% CMN and LMN-CMN thermometers. Closed circles: M <sub>1</sub> = .75444 gm LMN-CMN; M <sub>2</sub> = .55555 gm CMN. Open circles represent an indirect comparison of .90891 gm LMN-CMN and .55570 gm CMN	71
18.	Results of a temperature calibration of the refrigerator using LMN-CMN thermometers (M <sub>1</sub> = .90837 gm LMN-CMN; M <sub>2</sub> = .90891 gm LMN-CMN)	74
19.	The inverse temperature at the SQUID magnetometer $(1/T_S^*)$ as a function of the inverse temperature as defined by the LMN-CMN thermometer $(1/T_2^*)$ . Dashed lines represent the theoretically estimated effects based on siphon tube impedance measurements	77
20.	The inherent background susceptibility of the mixing chamber. Open circles - tail #2; closed circles - tail #1. The coil constant used for coil #1 was .0833 emu/dial unit and for coil #2 was .0883 emu/dial unit	80

Figure		Page
21.	The background susceptibility of the SQUID sample chamber at an applied field of 2.5 gauss	83
22.	Structural representation of a porphine molecule. This structure forms the basis for all porphyrins	88
23.	A comparison between the structure of a metallo- porphyrin and metallo-tetraphenylporphyrin molecule. The site labeled M represents a metal ion; open circles are nitrogen atoms and closed circles are carbon atoms	90
24.	The structure of copper tetraphenylporphine.  The relative positions of the numbered atoms are indicated in the text and in Table 6	100
25.	The manner in which the 3d orbital energy splits in crystalline field environments of different symmetry	106
26.	A perspective view of a CuTPP single crystal showing its relation to the crystalline axes	107
27.	A unit cell of CuTPP. The small squares around each copper site represents the porphyrin ring plane	109
28.	The projection of one unit cell of CuTPP on the (001) plane. Each line structure represents a different plane perpendicular to the c axis	111
29.	The manner in which the single crystals were mounted in the SQUID magnetometer for measurements of the parallel and perpendicular susceptibilities	126

Figure		Page
30.	The magnetic susceptibility data for CuTPP.  The solid lines represent the theoretical susceptibilities without inclusion of the dipolar interaction and the dashed lines represent the theoretical susceptibilities including the effect of dipole coupling	130
31.	The magnetic susceptibility data for CuTPP corrected for demagnetization effects. Open symbols represent data further corrected for thermal equilibrium effects. The +'s and x's represent an "effective powder susceptibility" derived from the single crystal data	144
32.	The high temperature single crystal and powder magnetic susceptibility data. The g values determined from this data are also shown. The "effective powder susceptibility" was obtained from the crystal data after normalizing the perpendicular susceptibility to $g_{\perp} = 2.001$	149
A.1.	A "circuit diagram" representing thermal resistance to heat flow between the two tails of the mixing chamber. Path A refers to heat flow through the liquid $(R_d^-R_c^-R_d^-)$ and path B to heat flow through the coil foil $(R_K^-R_{Cu}^-R_K^-)$ .	163
B.1.	The response function of a SQUID magnetometer. The total flux $(\phi)$ through the superconducting loop is plotted as a function of the external applied field	172

#### LIST OF TABLES

<b>Table</b>		Page
1.	The Entropy, Thermal Conductivity, and Viscosity of Concentrated <sup>3</sup> He and a Dilute Solution of 6.3% <sup>3</sup> He in <sup>4</sup> He at Low Temperatures	10
2.	Coil #1 Background Correction Equations	84
3.	Coil #2 Background Correction Equations	84
4.	SQUID Background Equations (H = .25 gauss)	85
5.	Inverse SQUID Temperature as a Function of $1/T_2^*$	85
6.	The Nonplanarity of a CuTPP Molecule. The Deviations of Various Atoms from the (001) Plane Passing Through the Copper Ion are Listed. Some Relevant Bond Lengths are also Tabulated	102
7.	Principle Values of the Interaction Tensors Relevant to CuTPP Along the Crystalline Axes <sup>55</sup> . The Values in Parenthesis were Obtained During Our Investigations of CuTPP	118
D.1.	Results of the CR-100 Germanium Resistor Calibration	185
D.2.	The Magnetic Susceptibility Data for CuTPP Single Crystal, Parallel Axis (Not Corrected for Demagnetization Effects)	186
D.3.	The Magnetic Susceptibility Data for CuTPP Powder and Single Crystal, Perpendicular Axis (Not Corrected for Demagnetization Effects)	187

		;

Table		Page
D.4.	The Magnetic Susceptibility Data for CuTPP Single Crystal, Parallel Axis, (Corrected for	
	Demagnetization Effects)	188
D.5.		
	Powder and Single Crystal, Perpendicular  Axis (Corrected for Demagnetization Effects) .	. 189
D.6.	The Effective Powder Susceptibility as	
	Determined by the Demagnetization Corrected	
	Single Crystal Data	190

#### INTRODUCTION

Recent advances in refrigeration techniques have extended the range of temperatures which can be reached into the millikelvin region. The means of achieving the very lowest temperatures (~ 2 mK) is almost exclusively by the adiabatic demagnetization of a cerium magnesium nitrate (CMN) sample which is precooled by a  $^{3}\text{He}^{-4}\text{He}$ dilution refrigerator. This important low temperature salt is also used to define the temperature scale down to about 6 mK by Curie law extrapolation of its magnetic susceptibility. However, thermometry below this temperature is rather uncertain. 1 The property of CMN which makes it so useful in ultralow temperature applications is its small paramagnetic ion density. Only for compounds of high magnetic dilution is the separation of the paramagnetic ions sufficient that their interaction is essentially due to weak classical dipolar coupling. dipolar solids exhibit very low ordering temperatures; therefore a complete study of them must involve ultralow temperatures. Also, since the lowest temperatures attainable by adiabatic demagnetization is limited by the ordering temperature of the salt, dilute paramagnetic systems with ordering temperatures lower than CMN will be

necessary to attain lower temperatures.<sup>2,3</sup>

Interest in the properties of dilute paramagnetic solids has been further stimulated by the results of several ongoing investigations. For example, anomously good thermal contact between CMN and pure <sup>3</sup>He at ultralow temperatures has been observed recently (see J. H. Bishop et al. 4 and the references therein). This unusual phenomena is probably due to magnetic coupling between the <sup>3</sup>He atoms and cerium ions at the liquid-solid interface. For a complete understanding of this interaction surface studies must be undertaken between liquid <sup>3</sup>He and other dipolar solids. Another very important discovery has been made in relation to the properties of pure <sup>3</sup>He at ultralow temperatures. Liquid <sup>3</sup>He was found to form, under pressure, two different phases, both of which are superfluid. 5 However, a complete study of the superfluid properties of <sup>3</sup>He is very difficult because it occurs at about 2 mK, the limit of temperatures presently attainable, and because of the lack of a good, practical thermometer which can be used in the low millikelvin temperature range.6

These problems indicate a need for new dipolar solids.

Only a few such compounds are known at the present time. 7,8,9

It is therefore essential to expand our knowledge of the nature of dipolar solids and to discover new compounds which may be useful in the production of lower temperatures, in the clarification of the absolute temperature scale at

ultralow temperatures, and in the study of several important properties exhibited by pure <sup>3</sup>He at ultralow temperatures.

The magnetic systems presently under study are the metalloporphyrins; their zero-field magnetic susceptibility are being measured from about 4 mK to 4.2 K. Molecules of the porphyrins are characterized by a basic structure to which various ligands can be attached without changing the environment of the paramagnetic ion. The spin density of crystalline porphyrins can be varied from as low as approximately 10<sup>19</sup> spins/cm<sup>3</sup> to as high as approximately 10<sup>21</sup> spins/ cm<sup>3</sup> by attaching different liquids to the basic porphyrin structure. These spin densities imply that the porphyrins will be primarily dipolar solids. The manner in which the spin density of a porphyrin can be diluted is important. The normal procedure for diluting a paramagnetic system is to replace some ions at random with an isostructural diamagnetic ion. The resulting disordered system is difficult to analyse because of the random nature of the occupation of each paramagnetic site. However, the dilution of a porphyrin is not a random process because the ions are simply separated further by the addition of larger ligands and still maintain a well-defined crystal structure. This thesis presents the results of the magnetic susceptibility studies on the first porphyrin (Copper Tetraphenylporphine) for which we have completed both powder and crystalline measurements.

The <sup>3</sup>He-<sup>4</sup>He dilution refrigerator has been designed and constructed for the initial purpose of carrying out ultralow temperature zero-field magnetic susceptibility studies on dilute magnetic systems. Its mixing chamber is a unique side-by-side arrangement designed to provide good thermal equilibrium between a thermometer in one tail and a sample in the other. Simultaneous measurements of the magnetic susceptibility of powdered samples located in each tail are made with two conventional ac mutual-inductance susceptibility coils.

To obtain useful magnetic susceptibility information one must also make measurements along the magnetic axes of single crystals. A SQUID magnetometer is utilized to make susceptibility measurements on very small (~ 1 mm³), aligned single crystals. The difficulties encountered in the study of very small single crystals in the SQUID magnetometer due to their physical size and effects such as demagnetization corrections are more than compensated for by the low temperatures to which the single crystal measurements can be carried. The large surface-to-volume ratio of these crystals means that they can be cooled to lower temperatures than is possible with larger crystals. These studies have shown that SQUID magnetometers are extremely useful devices in ultralow temperature studies of single crystal samples.

#### CHAPTER I

#### THE EXPERIMENTAL APPARATUS

## A. <u>History of the Dilution Refrigerator: Solutions of</u> 3He in <sup>4</sup>He

In the original theoretical work on the properties of  $^3\text{He-}^4\text{He}$  mixtures, Landau and Pomeranchuk $^{10}$  describe the  $^3\text{He}$  particles as an impurity in the  $^4\text{He}$  with an energy contribution given by:

$$E_3 = -E_{30} + p^2/2m_3^*$$

In this manner the  ${}^3\text{He}$  atoms are treated as independent particles within the  ${}^4\text{He}$  sea, having a binding energy  ${}^-\text{E}_{30}$  and a quasiparticle momentum p. The effective mass  $\text{m}_3^{\star}$  is a result of the interaction between a moving  ${}^3\text{He}$  atom and the  ${}^4\text{He}$  background.

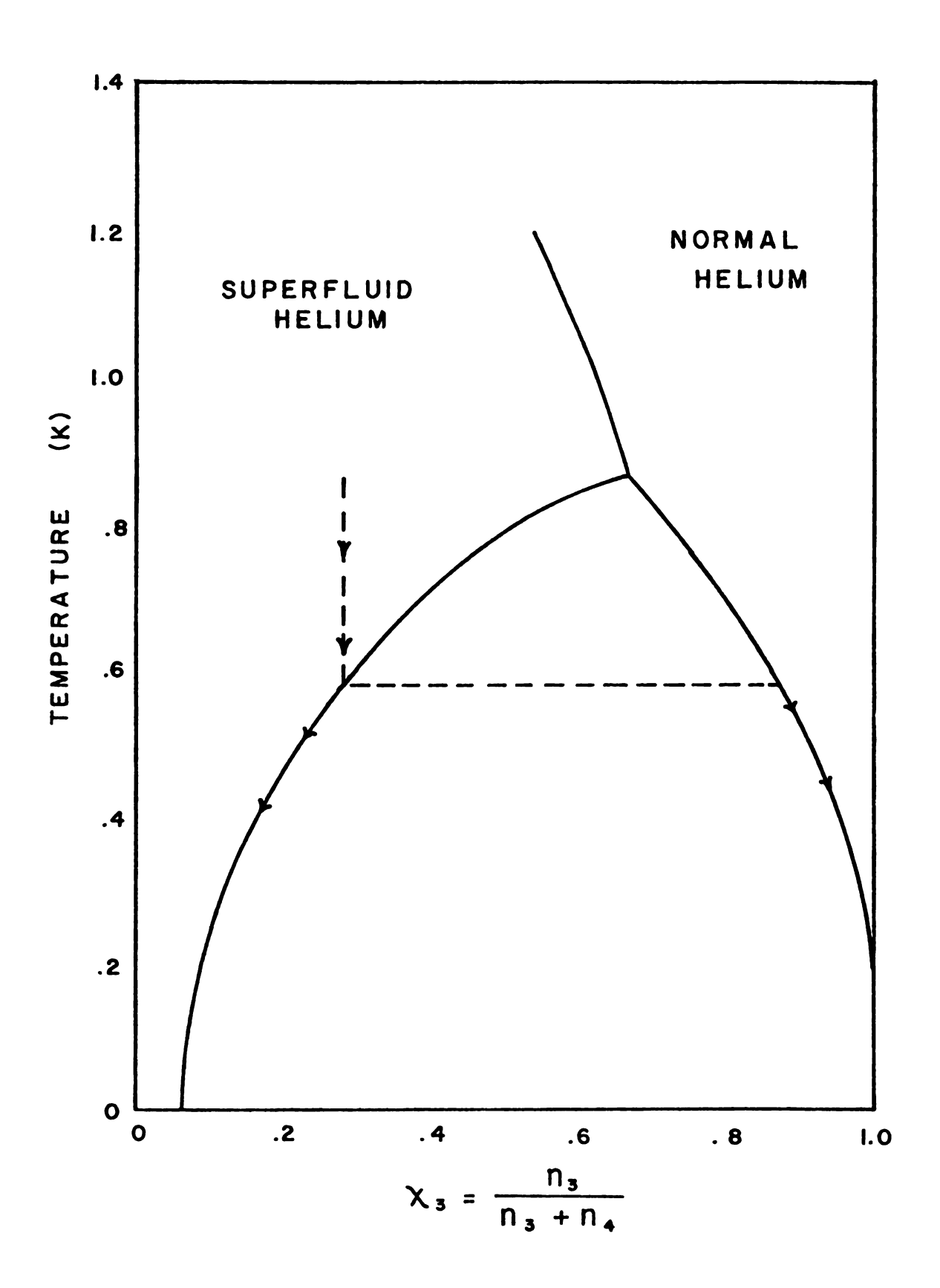
It was as a result of this theory that H. London  $^{11}$  later proposed that solutions of  $^{3}$ He and  $^{4}$ He be used to attain low temperatures. However, practical techniques for cooling with  $^{3}$ He- $^{4}$ He mixtures had to await the discovery of the existence of the phase separation phenomena in certain concentrations of  $^{3}$ He in  $^{4}$ He. This isotropic separation was first observed by Walters and Fairbank  $^{12}$  in 1956 and occurred at T = .83 K. Later specific heat measurements by

	::
	ä
	ć.
	:
	?.
	1
	i.
	E
	Ė
	:
	•••
	••
	•.
	::
	:
	:
	i <del>.</del>
	χ.
	:
	:
	3
	3
•	i;
	÷

Edwards, et al. 13 for various concentrations of 3He in 4He demonstrated the variation of phase separation temperature with <sup>3</sup>He concentration. The phase separation diagram has been determined experimentally by R. de Bruyn Ouboter, K. W. Taconis, et al. 14 and is shown in Figure 1. These measurements were made at saturated vapor pressure. finite solubility of <sup>3</sup>He in <sup>4</sup>He in the <sup>4</sup>He-rich lower region at low temperatures, essential to the operation of a dilution refrigerator, is due to the binding energy of an individual <sup>3</sup>He atom being greater in pure <sup>4</sup>He than in pure  $^{3}$ He. Since the masses of  $^{3}$ He and  $^{4}$ He atoms are different, the phase separation results in the lighter pure <sup>3</sup>He phase rising above the 4He-rich phase in the gravitational field. These developments led London, Clarke and Mendoza 15 to put forth the idea of attaining low temperatures by "evaporation" of the upper, <sup>3</sup>He-rich phase, into the lower, <sup>4</sup>He region. Also, it was suggested that the <sup>3</sup>He in the upper phase could be replenished, thereby allowing for the possibility of continuous refrigeration.

Since the operation of a dilution refrigerator is intimately connected with the properties of dilute solutions of <sup>3</sup>He in <sup>4</sup>He and of pure <sup>3</sup>He, much research was also being carried out to determine more about their properties. Some of the more important results, necessary for a better understanding of the operation of a dilution refrigerator, are presented here and will be referred to later. The entropy,

Figure 1. The phase separation diagram at saturated vapor pressure for  ${}^3\text{He}^{-4}\text{He}$  mixtures. The dotted line represents the phase separation of a 28% solution of  ${}^3\text{He}$  in  ${}^4\text{He}$ .



thermal conductivity, and viscosity (Table 1) are useful in explaining the actual cooling process and thermal equilibrium within a refrigerator. These properties are quoted for temperature ranges over which the expected Fermi-Dirac statistics are most obvious. More detailed discussions of these thermodynamic properties are presented by R. Radebaugh, 16 J. C. Wheatley, 17 and W. E. Keller. 18

The first dilution refrigerator was built by Hall, Ford, and Thompson. 19 Their refrigerator cooled to 65 mK under continuous operation. Within about a year the dilution refrigerator had been further perfected to the point where Viches and Wheatley 20 had built a refrigerator which cooled to 10 mK under continuous operation and 4.5 mK in the noncontinuous mode of operation.

The author and the research group he is associated with have recently built a dilution refrigerator capable of attaining temperatures of about 8.4 mK in the continuous operation mode and 4.0 mK in the "one-shot", noncontinuous mode.

Table 1. The entropy, thermal conductivity, and viscosity of concentrated <sup>3</sup>He and a dilute solution of 6.3% <sup>3</sup>He in <sup>4</sup>He at low temperatures.

ENTROPY per mole of He<sup>3</sup> (joules/mole-K)

 $s_c \approx 22 T$   $T \leq .15 K$ 

 $s_d \approx 102 \text{ T}$   $T \leq .10 \text{ K}$ 

THERMAL CONDUCTIVITY (erg/sec-cm)

 $K_c \approx \frac{18}{T}$  T  $\leq$  .04 K

 $\kappa_{\rm d} \approx \frac{30}{T}$ 

T ≤ .015 K

VISCOSITY (dyne-sec/cm<sup>2</sup>)

$$\eta_{\rm c} pprox \frac{2 \times 10^{-6}}{{
m T}^2}$$
 T \(\frac{2}{\cdot 0}\) K

$$\eta_{
m d} \, pprox rac{5 \, imes 10^{-7}}{
m T^2}$$
 T  $\leq$  .07 K

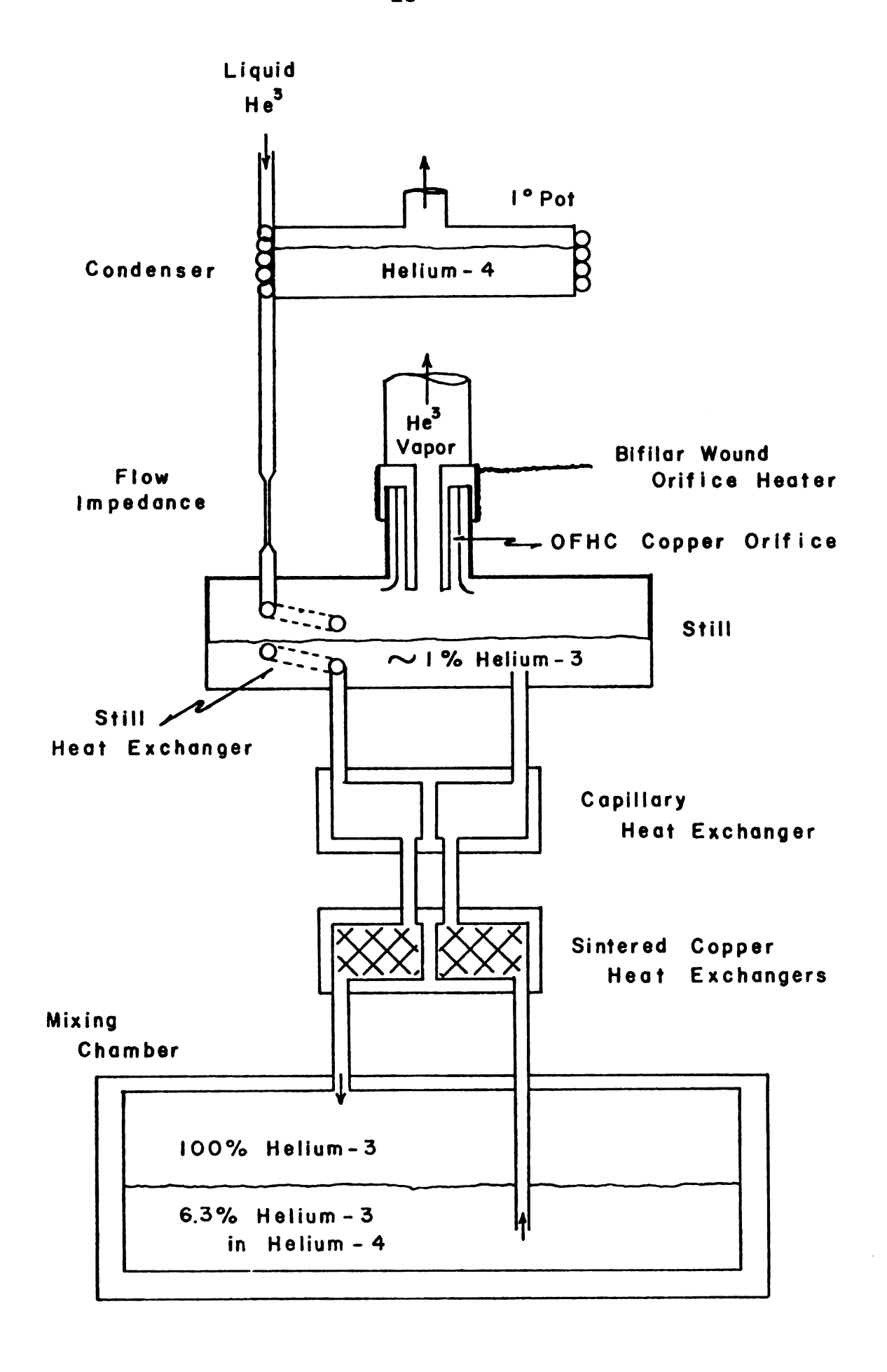
		:
		;
		;

#### B. Theory and Operation of a Dilution Refrigerator

Dilution refrigerators have become important to low temperature research not only due to their ability to achieve very low temperatures, but also because they may be operated continuously for extended periods of time. This continuous operation mode requires the circulation of <sup>3</sup>He atoms within the refrigerator. The path of <sup>3</sup>He flow through various parts of the refrigerator is shown in Figure 2, a schematic diagram of a dilution refrigerator. Gaseous <sup>3</sup>He is returned to the refrigerator through a condensing capillary which is thermally tied to the 1° pot. The 1° pot, actually a small <sup>4</sup>He evaporation refrigerator, is at a temperature of approximately 1.2°K. A flow impedance located immediately following the capillary maintains the incoming gas at a high enough pressure to cause its liquification at the condenser. The liquified <sup>3</sup>He is then allowed to pass through several stages of heat exchangers and then into the mixing chamber where the actual cooling occurs. The heat exchangers allow the incoming warm <sup>3</sup>He to be cooled prior to its introduction into the mixing chamber. The cold He then returns via the heat exchangers to the still where it is evaporated from the dilute solution, compressed, and returned to the condenser, thereby completing the cycle.

A <sup>3</sup>He-<sup>4</sup>He solution in a dilution refrigerator is cooled initially by operating the system as an evaporation refrigerator. The mixture cools by this method until it

Figure 2. A schematic diagram of a <sup>3</sup>He-<sup>4</sup>He dilution refrigerator indicating the flow of <sup>3</sup>He through the various components.



reaches the appropriate phase separation temperature. At this temperature an upper, <sup>3</sup>He-rich region will begin to form, ultimately reaching a concentration of 100% <sup>3</sup>He at lower temperatures. Concurrent with this is the formation of a <sup>4</sup>He-rich lower region which will eventually approach a concentration limit of 6.3% <sup>3</sup>He in a "bath" of <sup>4</sup>He. The relative volumes of the concentrated (<sup>3</sup>He-rich) and the dilute (<sup>4</sup>He-rich) sides of the refrigerator determine the <sup>3</sup>He concentration of the mixture to be used for a given refrigerator. It is important for the maximum efficiency to place the phase separation level inside the mixing chamber and not in the heat exchangers or interconnecting capillaries.

The cooling process which occurs within the mixing chamber can best be explained by referring to the properties of the concentrated and dilute phases (Table 1). We can see that at a given temperature the migration of a <sup>3</sup>He atom across the phase boundary must result in an increase in entropy for that atom. This increase in entropy is obtained by the absorption of heat from the dilute solution. The cooling process is made to be continuous by removing the <sup>3</sup>He atoms from the dilute solution and returning them to the concentrated <sup>3</sup>He region via the condenser. The great advantage of a dilution refrigerator over normal evaporation refrigerators, besides the possibility of continuous, long-term operation, can best be appreciated by comparing

the temperature dependence of the refrigeration capability of each system. The lowest temperature evaporation refrigerator, a liquid <sup>3</sup>He system, has a refrigeration capacity which is proportional to the <sup>3</sup>He vapor pressure. The vapor pressure is proportional to e , where L is the latent heat of the <sup>3</sup>He liquid and k is Boltzmann's constant. The ratio,  $L_{\Omega}/k$ , is 2.5 K for  $^{3}$ He so for temperatures on the order of .25 K the refrigeration capacity is already too small to be of much use because the vapor pressure is so low that the <sup>3</sup>He cannot be pumped away efficiently. However, the refrigeration capacity of a dilution refrigerator is approximately proportional to T2 at low temperatures due to the difference in the entropy per atom of pure <sup>3</sup>He and of a dilute solution of <sup>3</sup>He in <sup>4</sup>He. Since this entropy is proportional to T for both the pure  $^3\mathrm{He}$ and the dilute solution at low temperatures, their difference will also be proportional to T. This difference represents the entropy change of the <sup>3</sup>He as it migrates across the phase boundary. The entropy change can be related to the heat absorbed by the <sup>3</sup>He through the thermodynamic relation  $\Delta Q = T\Delta S$ . One immediately sees that the absorbed heat must be proportional to T<sup>2</sup>. Thus the dilution refrigerator can maintain a useful cooling capacity to much lower temperatures than is possible for a conventional evaporation refrigerator.

It is the purpose of the still to allow <sup>3</sup>He to be preferentially removed from the dilute solution and circulated

> jase jase Tar

:#<u>-</u>

ü<del>t</del>s

::E:

ite:

:: :

127 127

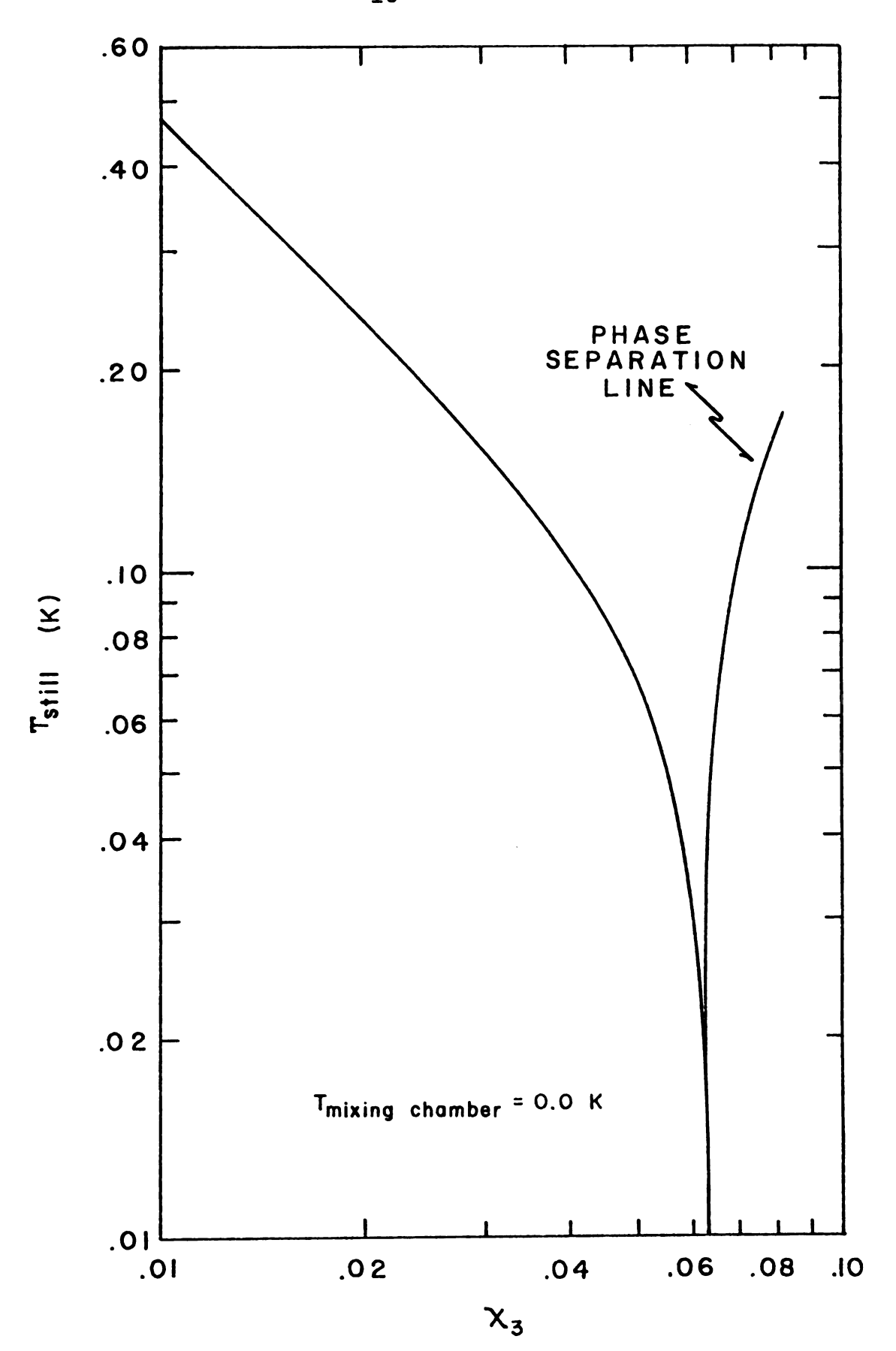
through the refrigerator. It generally operates at a temperature of about .65 K, which means the <sup>3</sup>He concentration in the still will be less than 1%. Although this would seem to contradict the concentration as predicted by the phase separation diagram, in reality it does not. phase diagram was determined at saturated vapor pressure with a uniform temperature throughout the mixture. Since there is a large temperature gradient between the mixing chamber and still, the phase separation diagram no longer applies in this portion of the refrigerator. The properties of the dilute solution in a thermal gradient, assuming the mixing chamber is held at T = 0.0 K, are shown in Figure 3. In order for thermal and mechanical equilibrium to be simultaneously maintained in the system (i.e. the Chemical potential of the <sup>4</sup>He to remain constant) there must be a concentration gradient in a thermal gradient. 21 The condition of constant chemical potential of the <sup>4</sup>He in the dilute solution return lines is required if there is to be no acceleration of the superfluid in this region. This Could result in convective heat flow from the still to the maxing chamber. In order to prevent any such heat flow, the dilute solution return lines are constructed from small capillary tubing which effectively blocks the flow f <sup>4</sup>He normal fluid. 22

Since it is desired that only <sup>3</sup>He be circulated through

the system during its operation, as will become apparent

later, this low <sup>3</sup>He concentration in the still would seem

Figure 3. The  $^3$ He concentration of the still as a function of still temperature assuming the mixing chamber to be at a temperature of 0.0 K.



		:
		:

to pose a problem. However it happens that due to the weak binding of the <sup>3</sup>He quasiparticles to the <sup>4</sup>He background in comparison to the binding of a <sup>4</sup>He atom to the <sup>4</sup>He background, the partial vapor pressure of <sup>3</sup>He above the liquid is much higher than the partial vapor pressure of <sup>4</sup>He.

Despite this fact there is another process which can work to decrease the high <sup>3</sup>He partial vapor pressure. The <sup>4</sup>He liquid in the dilute solution, being superfluid, can rise through the pumping-line orifice of the still by film flow and evaporate at a higher temperature inside the pumping line. This is the familiar thermo-mechanical or fountain effect observed in superfluid helium.

As the <sup>3</sup>He concentration in the still is lowered by evaporation of <sup>3</sup>He the system will replenish the lost <sup>3</sup>He atoms in order to maintain the required equilibrium concentration at that temperature. An osmotic pressure gradient will be produced between the still and mixing chamber by the removal of <sup>3</sup>He atoms at the still, thereby causing <sup>3</sup>He atoms to migrate from the mixing chamber into the still. The <sup>3</sup>He atoms subsequently removed from the dilute solution region of the mixing chamber can be replenished from the concentrated <sup>3</sup>He region above the phase boundary to keep the dilute solution at its proper low temperature concentration of 6.3% <sup>3</sup>He, and in the process will cool the mixture.

This flow of cold <sup>3</sup>He from the mixing chamber to the still is used to cool the incoming warm liquid <sup>3</sup>He through several stages of heat exchanging. The effectiveness of

)

on the ability of the refrigerator to prevent <sup>4</sup>He from being circulated with the <sup>3</sup>He. If <sup>4</sup>He is present in the incoming warm liquid, the heat exchangers besides having to cool the liquid will also have to absorb the heat liberated as the <sup>4</sup>He phase separates from the <sup>3</sup>He. Therefore the <sup>3</sup>He to <sup>4</sup>He ratio in the circulated gas should be as large as possible.

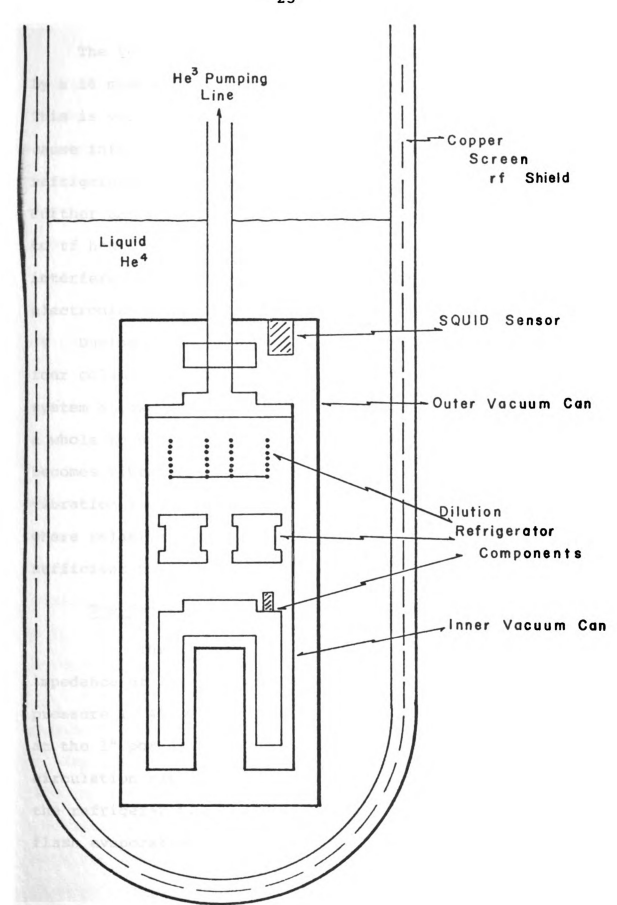
## C. Design and Operation of this Dilution Refrigerator

## An Overview

The dilution refrigerator built by this research group was designed initially for studies of the magnetic susceptibility exhibited by dilute magnetic systems. The apparatus contains two conventional mutual-inductance magnetic-susceptibility coils, one being used to monitor the refrigerator's temperature and the other to study a sample. A Superconducting Quantum Interference Device (SQUID) magnetometer was added for magnetic measurements on very small samples. A schematic view of the cryostat depicting the overall relationship of its major components is presented in Figure 4.

The refrigerator is contained within two vacuum cans which separate it from the surrounding bath of liquid  $^4\text{He.}$  The outer vacuum can also serves to support a magnetic shield arrangement necessary to isolate the susceptibility coils and SQUID magnetometer from external magnetic fields. This shield consists of an inner layer of sheet lead covered by an outer layer of  $\mu\text{-metal.}$  The  $\mu\text{-metal}$  reduces the effect of the earth's magnetic field at the SQUID position to approximately .07 gauss, while the lead shield in its superconducting state prevents any changing external magnetic field from being transmitted to the magnetometers.

Figure 4. An overall view of the cryostat. The dilution refrigerator components are enclosed within a vacuum space and interconnected by capillary tubing which carries the flowing <sup>3</sup>He.



The refrigerator is also shielded from rf interference by a 16 mesh copper screen attached to the helium dewar.

This is very important because rf induced eddy currents may cause internal heating within the metallic parts of the refrigerator, especially those constructed of copper.

Further and possibly more severe problems can develop due to rf heating of the carbon resistance thermometers and interference with the magnetic susceptibility bridge electronics.

During the operation the entire apparatus floats on four columns of compressed nitrogen gas. This support system allows the resonance frequency of the apparatus as a whole to be lowered to about 1 hertz so it effectively becomes vibrationally isolated from the building. This vibration isolation is necessary at the lowest temperatures where relative motion between refrigerator parts may be sufficient to cause internal heating.

#### The Condensor, Heat Exchanger, and Still.

The incoming  $^3$ He passes through a condensing impedance of 2 x  $10^{12}$ /cm $^3$  which produces a high enough pressure (~ 40 mm Hg) to insure liquification of the  $^3$ He at the 1° pot. This flow restriction requires a  $^3$ He circulation rate of at least 3.0 x  $10^{-5}$  moles/sec through the refrigerator. The 1° pot itself is patterned after the flash evaporation design of L. E. DeLong et al. $^{24}$ .

The transfer of heat between the incoming warm <sup>3</sup>He and the outgoing dilute solution is accomplished through five stages of heat exchanging. Initially this liquid is allowed to come into close thermal contact with the dilute solution in the still, which is operating at a nominal temperature of .65 K, by flowing through 100 cm of .025 cm inside diameter (.0075 cm wall thickness) cupro-nickel capillary tubing wound inside the still. The precooled liquid is then allowed to pass into the capillary exchanger. This heat exchanger is composed of two series connected sections each containing two concentric thinwall cupro-nickel capillary tubes. one section, which has an overall length of 150 cm, the inner tube has an inner diameter of .025 cm (wall thickness = .0075 cm) and the outer tube an inner diameter of .119 cm. The other section is 100 cm long with the inner tube diameter being increased to .036 cm (wall thickness = .0075 cm). incoming warm <sup>3</sup>He liquid is made to flow through the inner capillary, and thus is completely surrounded by the cold dilute solution which flows through the annular region between the capillaries.

The last three stages of heat exchange occur in identical exchangers made from sintered copper disks and interconnected by capillary tubing. The sizes of these capillaries are similar to those reported for other dilution refrigerators. 25 The basic design of these exchangers is shown in Figure 5. Both the incoming <sup>3</sup>He and outgoing dilute solution pass through a volume filled with sintered copper powder. <sup>26</sup> The

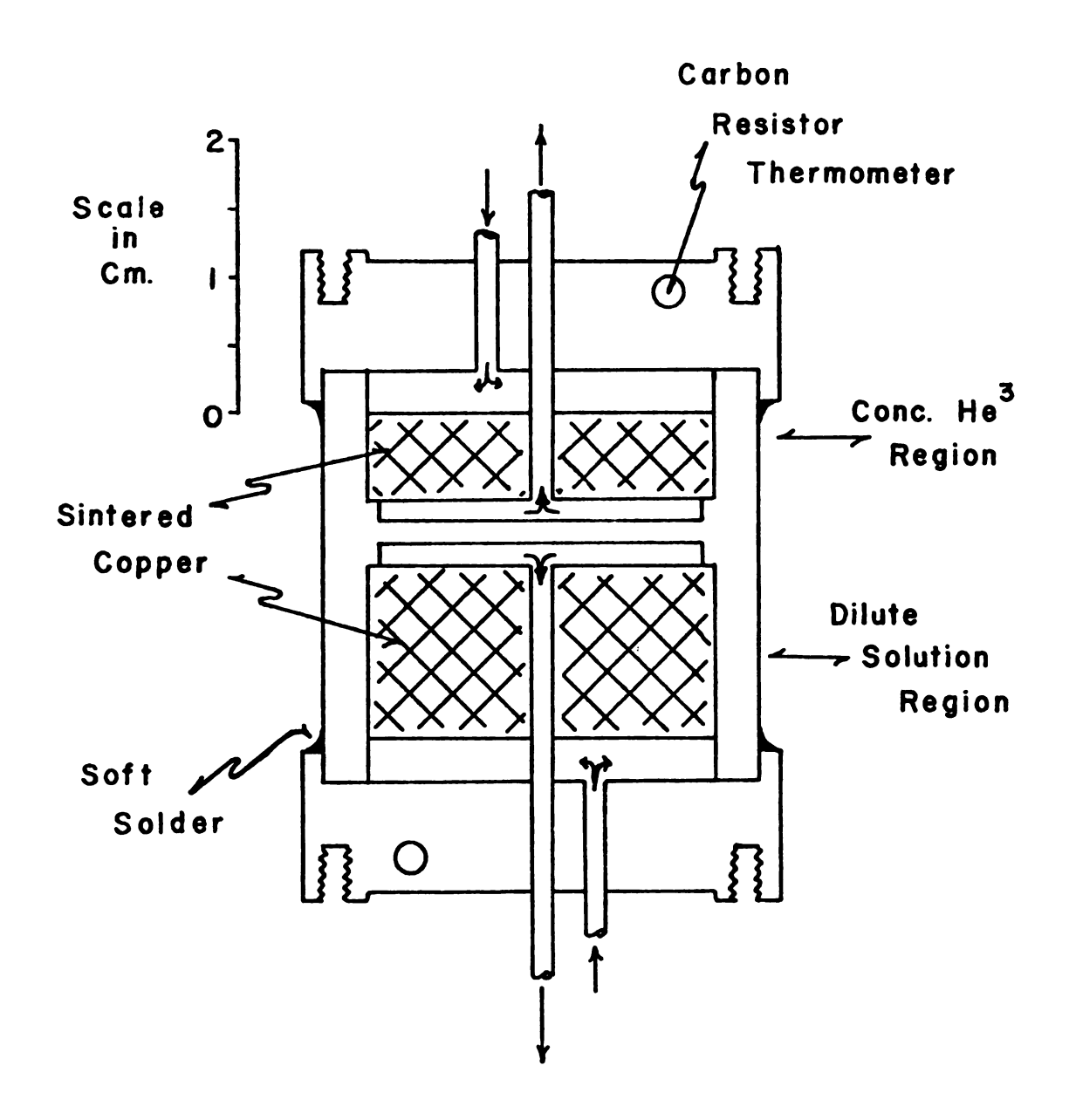


Figure 5. A detailed drawing of a sintered copper heat exchanger showing the flow of liquid helium.

heat exchanger volume must be relatively large (~ 1 cm<sup>3</sup>) in order to provide efficient exchange of heat between the <sup>3</sup>He quasiparticles and the 4He phonons in the dilute solution. The large surface area of this sintered copper facilitates the transfer of heat between the 4He phonons and the copper at low temperatures where Kapitza resistance becomes increasingly significant. This resistance  $(R_{K} = \frac{\Delta T}{\delta} \frac{K}{erg/sec})$ is due to acoustic mismatch between the copper and <sup>4</sup>He phonons at the interface of the dilute solution and copper metal. 27 To further enhance the heat flow between the sintered copper disks the body of each exchanger is constructed from high purity OFHC copper. The mechanism of heat transportation within the copper is via the conduction electrons. The disks were shrunk-fit into the bodies of the exchangers. At a mixing chamber temperature of 10 mK these exchangers operate at about 70 mK, 45 mK, and 20 mK respec-These components are mounted within the refrigerator tively. on a framework mainly constructed from pressed graphite. This material has enough strength to easily support the refrigerator components. It also provides a means of thermally isolating them from each other because of its very low thermal conductivity.

The problem of film flow into the still orifice and the subsequent circulation of <sup>4</sup>He seems to have been eliminated in our refrigerator. This process is countered by wrapping a heater around the pumping line orifice (see Figure 2).

112 ( 112 ) 122 ) 122 ( 123 ) 124 ( 124 ) 125 ( 126 )

> zálí Alo: see

> > in the

ite Dv

ia,

oa :

47.9

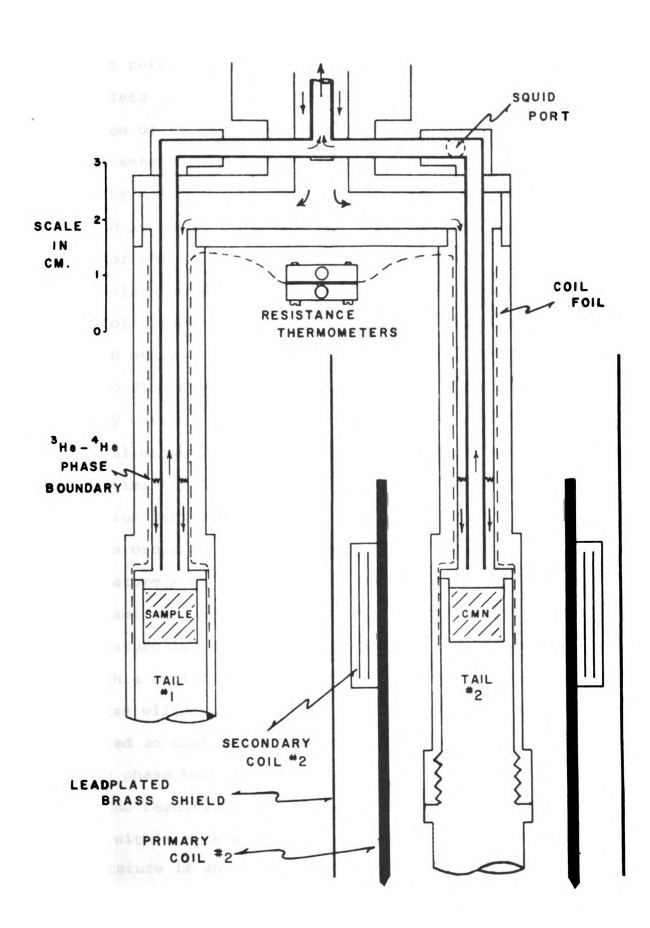
This orifice heater drives the ever-present superfluid <sup>4</sup>He film normal and effectively blocks its flow into the pumping line. By appropriate adjustment of the orifice heat, <sup>3</sup>He to <sup>4</sup>He ratios of 50:1 can easily be maintained in the circulating gases. This ratio can be measured during the operation of the refrigerator by a mass-spectrometer leak detector <sup>28</sup> allowing optimum <sup>3</sup>He-<sup>4</sup>He ratios to be established throughout the course of an experiment. This removal of the <sup>4</sup>He from the circulated gas allows our refrigerator to operate with less heat exchangers than would normally be required.

# The Mixing Chamber

The standard mixing chamber design has been modified in our apparatus to form a dual-tail arrangement which allows a cerium magnesium nitrate (CMN) thermometer (see page 61 for a discussion of thermometry) and a sample to be in close thermal contact with each other. The basic mixing chamber and susceptibility coil arrangement is shown in Figure 6. This sketch does not show the details of the mixing chamber, but is primarily for presenting the relative arrangement of components within the chamber. Also, the flow of <sup>3</sup>He within the system is indicated by arrows. During operation there are actually two phase separation boundaries located approximately 1.0 cm above the samples in each tail.

A Superconducting Quantum Interference Device (SQUID) magnetometer system has been installed above tail #2. The

Figure 6. A schematic drawing of the dual tail mixing chamber. The arrows represent the flow of <sup>3</sup>He through the mixing chamber. For clarity only the upper half of one of the magnetic susceptibility coils is shown.



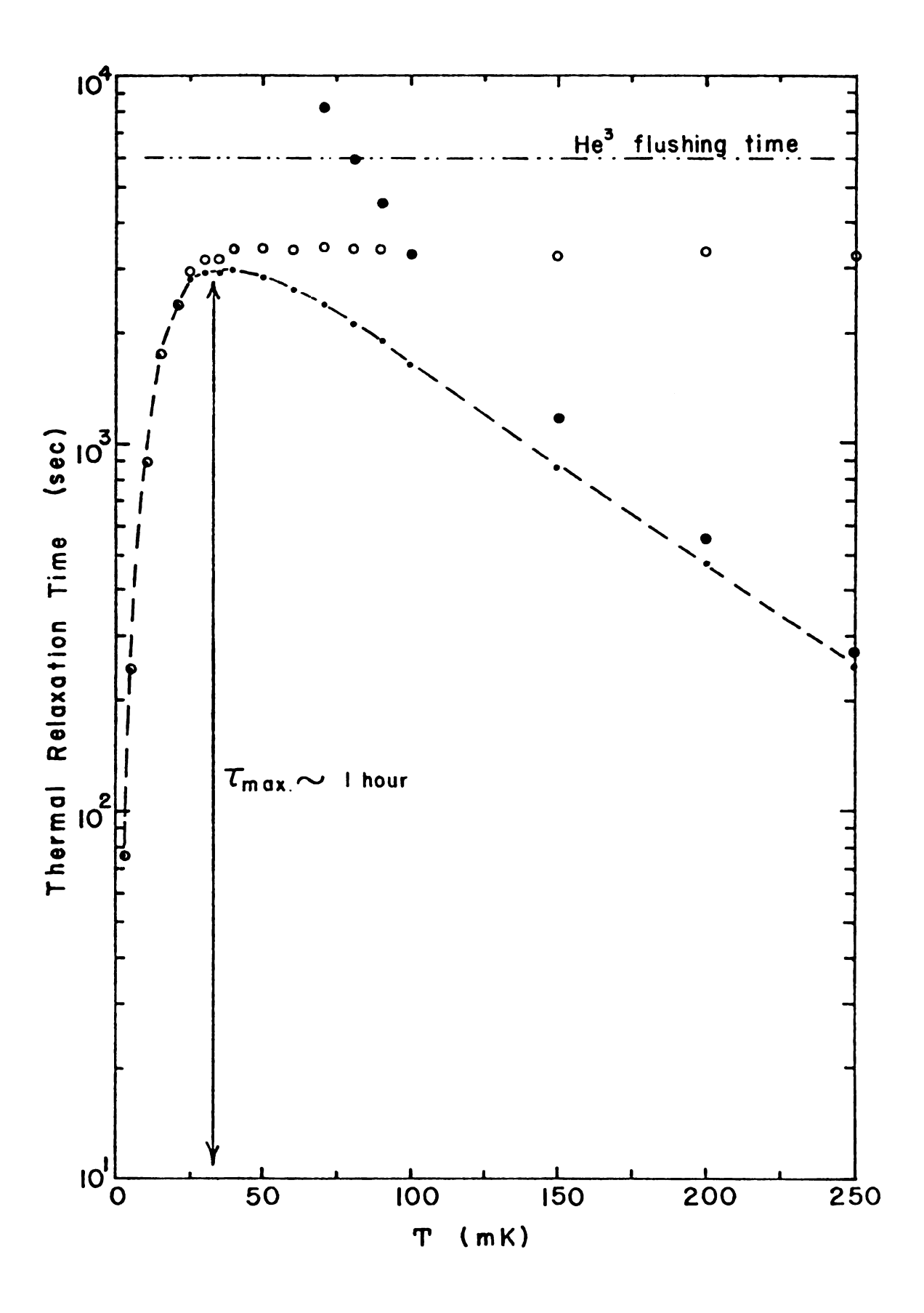
<u>:</u>
:
;
•
:
:
ï
i
:
;
ę
:
:
:
:
2
:
: :
;
:

dilute solution provides the means of maintaining thermal contact between the SQUID sample and the CMN thermometer. A complete discussion of the SQUID magnetometer and the question of thermal equilibrium between these parts will be presented later.

The mixing chamber parts were molded and machined from Epibond 100-A epoxy. 29 Copper coil-foil was molded into the interior walls of the upper half of each tail to present a low resistance thermal path at higher temperatures. The coil foil consists of strands of copper wire bonded parallel to each other so as to form flat sheets. This design allows heat to flow along the wires and avoids the possible formation of eddy currents within the copper due to time-varying external magnetic fields. The upper ends of this coil foil are intimately attached to a copper block containing a germanium resistance thermometer.

In order to take experimental data, the mixing chamber temperature must be stabilized and thermal equilibrium must be established between the tails. Stabilization of the temperature is accomplished by heating the <sup>3</sup>He as it flows through a capillary tube into the mixing chamber. The temperature will remain constant when the applied heat is adjusted so that it is exactly balanced by the cooling rate at the phase boundaries.

The results of an estimation of the thermal relaxation times within this system (see Appendix A) as a function of temperature is shown in Figure 7. As the mixing chamber Figure 7. Results of a theoretical calculation of the expected thermal relaxation time of a dual-tail mixing chamber. Closed circles represent heat conduction through the coil foil and mixing chamber walls. Open circles represent heat conduction via the liquid helium. The total relaxation time is represented by a dashed line.



is being cooled from one temperature to another, a thermal gradient may be produced between the two tails. Any such temperature difference must be allowed to become small before a susceptibility measurement can be made. Assuming the temperature difference will relax exponentially, the relaxation time is defined as the time necessary for the initial temperature difference to drop to 1/e of its original value (i.e.  $\Delta T = \Delta T_0 e^{-t/\tau}$  where  $\tau$  is the thermal relaxation time). This estimation was based on a calculation of the relaxation time for heat flow from one tail to another assuming parallel paths of heat flow through the coil-foil and liquid. This calculation does not take into account the flow of <sup>3</sup>He through the mixing chamber. results show that the longest relaxation times occur at approximately 30 mK with values on the order of one hour. At high temperatures the copper coil-foil path provides the least resistance to heat flow between the tails, while at low temperatures, where Kapitza resistance between the copper wires and the <sup>3</sup>He becomes appreciable, the dilute solution offers the path of least thermal resistance.

An alternative means of estimating the relaxation time between the tails can be made on the basis the <sup>3</sup>He flow rate. The time necessary for the <sup>3</sup>He liquid to divide, flow through each tail, and recombine in the siphon tubes is also a measure of the refrigerator's relaxation time. Calculations show that at temperatures above 10 mK and a flow rate

**::** 5

ίχ

: :e

<u>-11</u>

2

:::E

ř:

11:3

žŧ

iņ.

::<u>:</u>

Ė

it; i

it.

i. Lės

:::

:: t

ĊĮ.

: (1)

43

٠ ا

:

of 5 x 10<sup>-5</sup> moles/sec, this process requires about 6 x 10<sup>3</sup> sec. Of course in reality the relaxation time is a result of a combination of both <sup>3</sup>He flow through the mixing chamber and thermal conduction. Observations of the refrigerator in operation indicate that the relaxation times are on the order of two hours. In actual practice we find the major thermal relaxation problems are not caused by the relaxation times within the refrigerator, but are usually due to the relaxation times associated with Kapitza resistance at the surface of powders and crystals being studied.

In order to circulate the cold dilute solution around the samples and to maintain the positions of the phase separation levels near the samples, siphon-tube return lines were placed immediately above the sample sites (Figure 6). These tubes were machined from Epibond 100-A epoxy and constructed so as to minimize the total flow impedance presented to the mixture. The tubes have an inner diameter of .272 cm and an outer diameter of .406 cm. They are positioned concentrically inside the tails, which have a .635 cm inside diameter. The flow impedance in each annular region was measured by allowing nitrogen gas to flow through them at room temperature and utilizing the following expression for impedance:

$$Z = \frac{\Delta p}{n} (\frac{\Delta t}{\Delta v})$$
 (cgs units)

where  $\eta$  is the viscosity of the gas, and  $\Delta v/\Delta t$  is the volume flow rate for a pressure difference of  $\Delta p$ , which is assumed small compared to the total absolute pressure. It was found that the impedances were 2.92 x  $10^4/\text{cm}^3$  and 3.56 x  $10^4/\text{cm}^3$ .

Since the viscosity of both pure <sup>3</sup>He and dilute solutions of <sup>3</sup>He increases as 1/T<sup>2</sup> at low temperatures, these impedances become important in considering the question of viscous heating of the flowing solutions in the tails at low temperatures. An estimate of the thermal gradient which may be produced can be made by utilizing the following expression which relates the thermal gradient in the mixture (or pure <sup>3</sup>He) to the impedance presented to the flow of liquid:

$$\frac{\Delta T}{T} = K \left( \frac{Z}{10^8 \text{cm}^3} \right) \left( \frac{\mathring{n}_3 / \mathring{A}_0}{10^{-5} \text{moles/sec}} \right) \left( \frac{20 \text{ mK}}{T} \right)^4 \qquad \frac{\Delta T}{T} << 1$$

In this equation T is the temperature in mK and K is a constant which is .07 for pure <sup>3</sup>He flow amd .54 for the flow of dilute solution. With this expression we calculate that the temperature difference between the two tails with the phase separation levels at approximately 1.0 cm above each sample is at most only .1% at 10 mK as a result of impedance effects. The dividing of the mixing chamber into two tails and the resulting formation of two phase separation lines therefore would seem to present no serious thermal equilibrium problems between the tails. More will be said later about the effect of the impedance of the siphon tubes on the temperature of the SQUID.

The samples being studied are contained in sample chambers which were designed with two main criteria in mind; first to minimize the difficulty of changing samples in a leak tight system and second to make sure the mixing chamber would not be contaminated by the sample which had been previously studied. Both problems have been solved quite well. Figure 8 shows the details of the sample chamber construction. The samples are packed into independent, removable epoxy holders. They may either be packed directly into these holders, or, if a smaller mass of sample is desired while still retaining it in the shape of a right circular cylinder, packed into smaller units designed to slide inside the usual holders. The samples are covered with and placed on filter paper to trap all loose particles. To further avoid problems, no unit is used twice, a new one being made for each different sample.

The problems associated with installing and removing samples from the refrigerator and still maintaining the necessary leak tight joints have been solved by using a remarkable glue made from glycerine and Ivory soapflakes. 30 Both tails of the mixing chamber are threaded at the sample chamber to allow easy access when replacing samples. To assure a leak-tight fit, the female parts of the threads were tapped, then the male parts were cut with a lathe until a snug fit was obtained. The seal is made by warming the glue until it is a liquid, then coating the male thread with

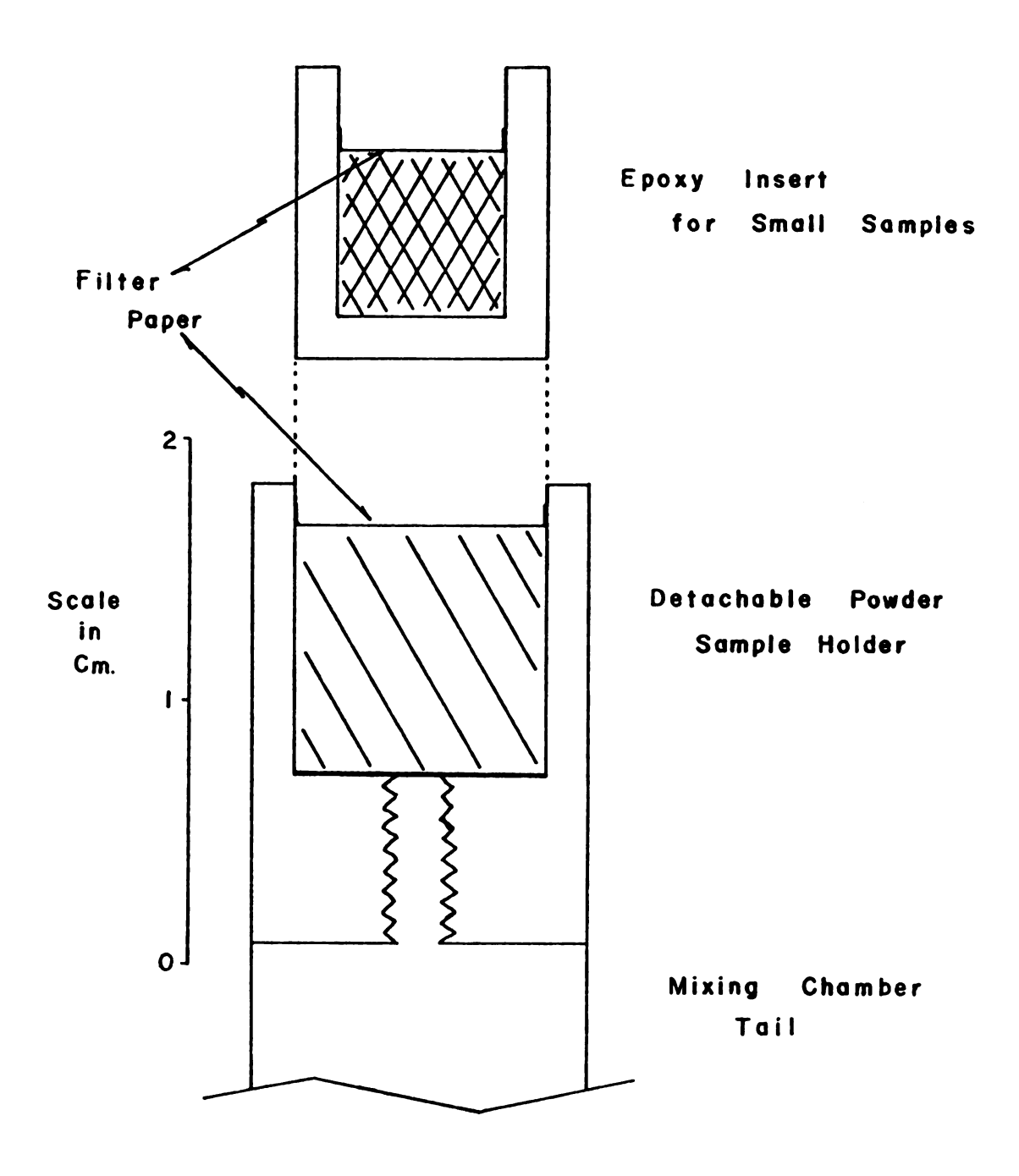


Figure 8. A detailed view of the sample chamber design.

the glue and screwing the entire unit, with the sample in place, into the refrigerator. After the glue sets it is possible to evacuate the refrigerator, but we usually wait until the apparatus is cooled to 0°C before evacuation. This type of seal has proven to be extremely reliable in this apparatus.

It should be mentioned also that equally reliable seals, although of the permanent type, were made during the construction of the mixing chamber by using Epibond 121 liquid epoxy. This epoxy is the standard glue used for joining pieces of Epibond 100-A epoxy. The convenience and versatility of these epoxy resins and the glycerine and Ivory soapflakes glue should not be underestimated in the building of low temperature refrigerators. Modular mixing chambers designed for various types of experiments are a realistic possibility through utilization of these materials.

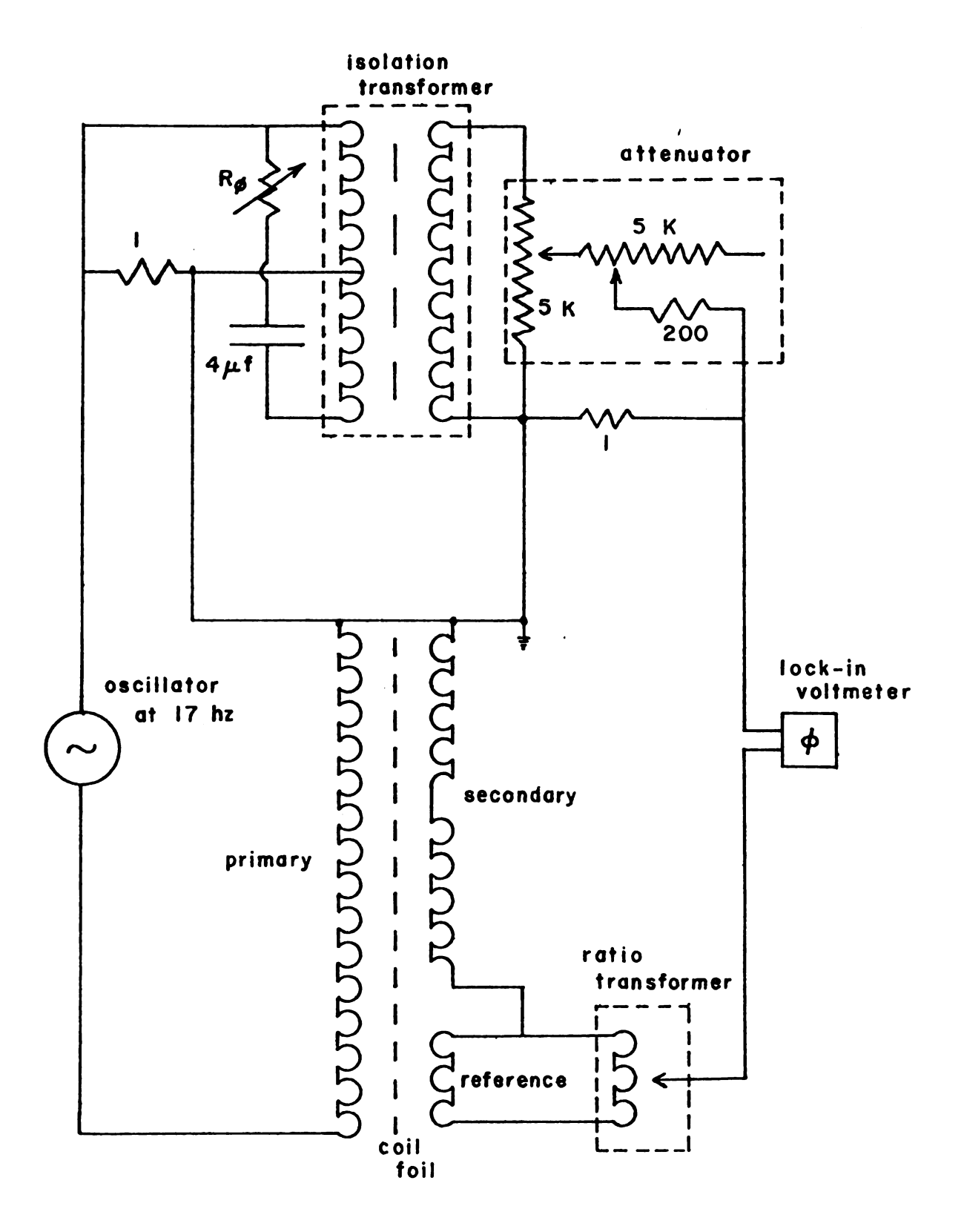
## D. Measurements of Magnetic Susceptibility

## The Conventional Magnetic Susceptibility Coils

The conventional methods of measuring the magnetic susceptibility of a substance are based on techniques where the sample's magnetization changes the mutual inductance between two coils. One coil, the primary, is used to produce a small ac magnetic field at the sample. The other coil, the secondary, is wound coaxial with the primary in two sections which are connected in series and are in opposition. Thus to first order the total primary-secondary mutual inductance is zero. The primary-secondary mutual inductance is influenced by the temperature dependent magnetization of the sample which is located within one of the secondary sections. In order that the epoxy mixing chamber tails do not couple magnetically to the secondary coil they extend below the samples so that equal amounts of epoxy are interior to each secondary coil. 31

A schematic diagram of a susceptibility coil and the associated mutual inductance bridge circuit necessary for these measurements is shown in Figure 9. A fraction of the reference mutual inductance signal is tapped by the ratio transformer and used to null the change in the primary-secondary mutual inductance produced by the magnetization of the sample. Since the complex susceptibility ( $\chi = \chi' + i\chi''$ ) has a resistive loss component as well as an

Figure 9. A block diagram of the ac mutual inductance bridge circuit. All resistances are in ohms.



inductive component, one must ensure that the reference mutual inductance signal is only being used to balance the signal produced in the secondary due to the inductive coupling between the paramagnetic sample and secondary coil windings. For this reason the primary and secondary circuits are coupled via an isolation transformer by which the resistive component can be nulled. The phase adjustment  $R_{\varphi}$  is used to ensure that the isolation transformer signal is indeed the "90° phase" resistive component.

The susceptibility coils, their placement relative to the refrigerator being shown in Figures 10 and 11, were patterned after those reported by A. C. Anderson, R. E. Peterson, and J. E. Robichaux. 32 One major addition which was made, because of the proximity of the two coils to each other, was to surround both coils with superconducting lead-plated brass shields. This is necessary to avoid interaction between the coils due to the primary of one coil coupling into the secondary of the other. A more detailed view of the coils, Figure 12, shows their construction much more clearly. The coils were carefully made to be as nearly identical as possible.

The primaries were wound on forms of Epibond 100-A machined to 3.175 cm outside diameter. The overall length of each primary is 10 cm, being composed of 2480 turns of #32 copper wire wound in six layers. Each layer is separated by .25 mil. mylar with 1.0 mil. mylar being used under the

Figure 10. A detailed drawing of the dilution refrigerator and susceptibility coils. A = copper flange with lead fusewire "O"-ring; B = stainless steel support tube sealed in epoxy; C = SQUID mounting port; D = copper inner vacuum can connected to the still; E = copper to epoxy joint; F = coil foil.

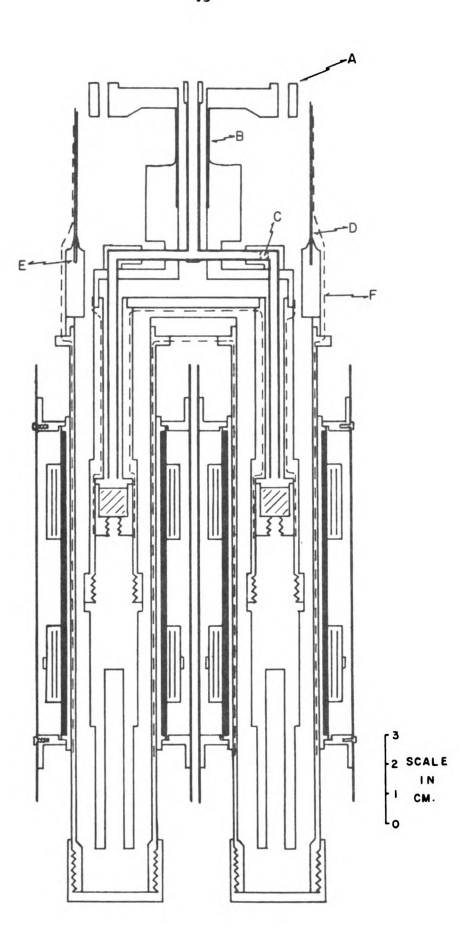
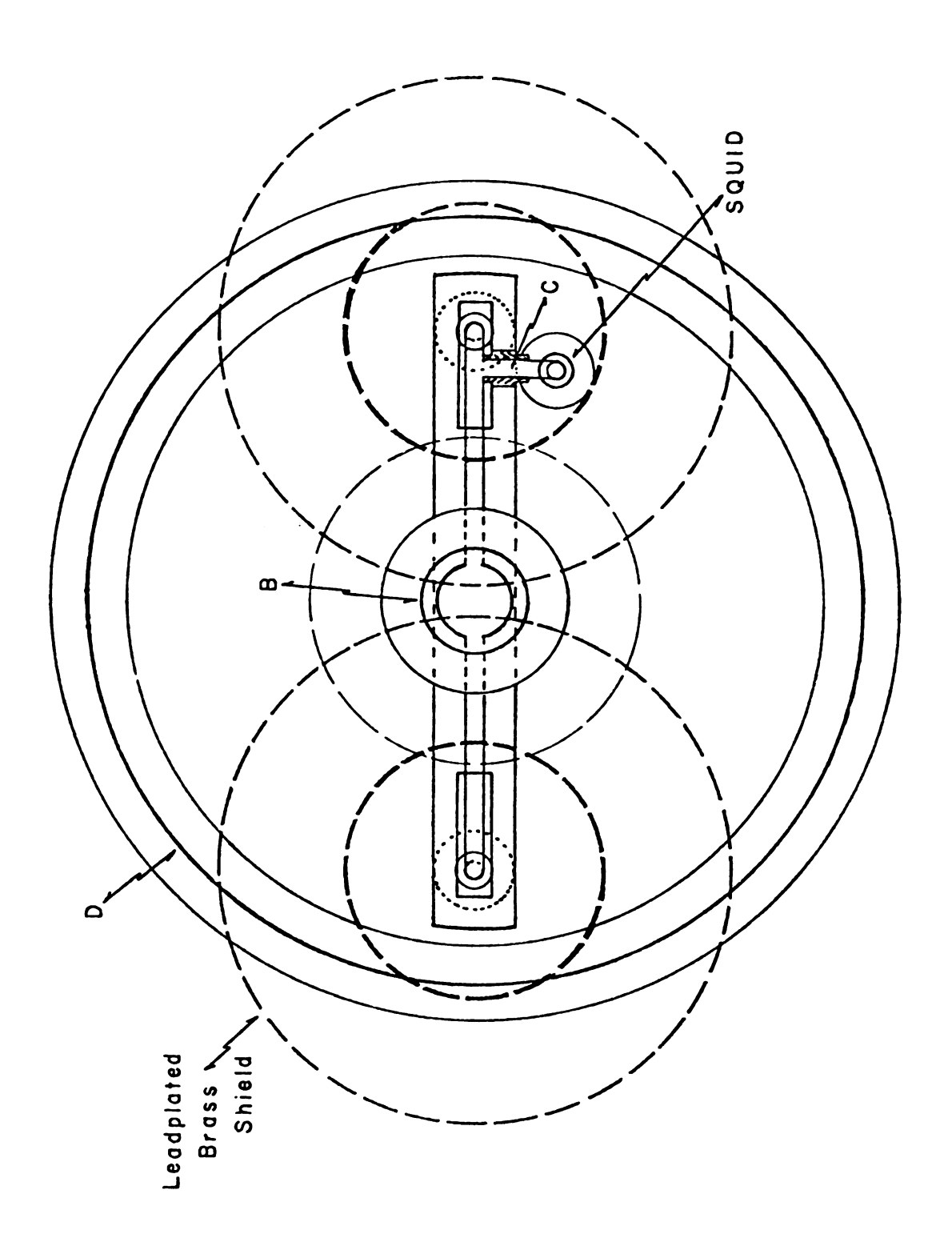


Figure 11. A top view of the dilution refrigerator and susceptibility coils. The letters refer to parts which are similarly labeled in Figure 10.



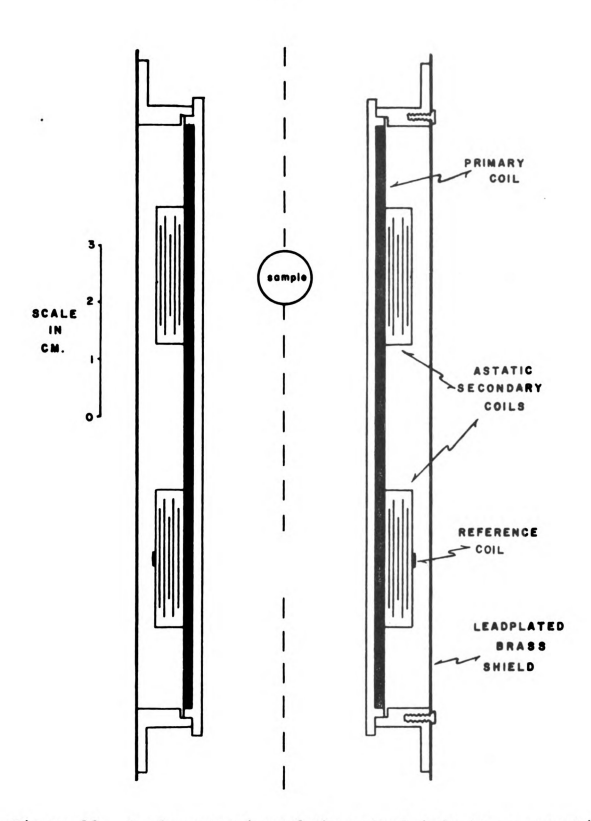


Figure 12. A close-up view of the mutual inductance magnetic susceptibility coils detailing their construction.

first and over the last layer. Mylar is used to prevent electrical shorts from forming between layers, which would occur if the copper insulation weakens under thermal stress and to allow for some flexibility as the coils contract during cooling. In order to ensure interwinding stability and to further protect against shorts, each layer is heavily covered with a "glue" composed of 50% GE 7031 varnish and 50% toluene. Wrapped around the outside of the primary is a Faraday shield constructed from a layer of copper coil foil situated so that its wires run parallel to the axis of the coil.

The two backwound sections of the secondary coil each contain 3800 turns of #36 copper wire. The primary-secondary mutual inductance with this design is approximately 82 mhenry for each section in the absence of the lead shield. Each section is 3.0 cm in length and positioned such that their center-to-center separation is 4.25 cm. The toluene and GE 7031 varnish glue was again liberally applied to ensure rigidity with respect to thermal stressing, but mylar was only used under the first and over the last layer of each section. The windings were supported by teflon split rings during their construction until the glue had set firmly. To minimize uncontrolled shifts in the balance point of the susceptibility bridges due to primary-secondary capacitive coupling, the outer layer of the primary and the inner layer of one secondary section are interconnected and grounded to the cryostat.

A reference mutual inductance was made by winding 100 turns of #36 copper wire on the secondary section which does not contain the sample. The reference mutual inductance is .55 mh with the superconducting shield around the coils.

The entire coil system is mounted inside a vacuum space and is thermally attached to the still. The superconducting shields which surround each coil consist of a thinwall .079 cm brass tube with an inner diameter of 4.76 cm. surface of the tube was electroplated with a .003 cm layer of The length of the tube, 14.29 cm, allows it to pure lead. extend beyond the ends of the coil and better shield against nearby magnetic objects and the magnetic field produced by the neighboring coil. In order to test the effectiveness of this supershield arrangement, a .794 cm steel ball bearing was lowered to the shield's edge while the coil was at liquid helium temperatures. The result was an introduction of only a .04 µhenry imbalance of the coil. Thereafter we were confident that any effect on the balance condition of the coil due to a nearby sample would be negligible.

The presence of the superconducting shield tends to reduce the magnetic field produced by the primary coil at the sample. The effective field inside the primary now becomes approximately:

$$B_{eff} \sim B_p (1 - A_p/A_s)$$

where  $B_p$  is the field produced without the superconductor being present and  $A_p/A_s$  is the ratio of the cross-sectional area of the primary coil and shield. For our coils this means that  $B_{\rm eff} = .513 \; B_p$ . Detailed computer calculations of the effect of superconductors on magnetic fields has recently been carried out by Todd I. Smith. 33 His results show that a further effect of the superconducting shield is to reduce the variation of the magnetic field over the volume of the sample.

These coils have behaved well despite the rigors of many cooling and warming cycles. Their balance point at 4.2 K changes very little from experiment to experiment, an indication of good interwinding stability. Sensitivity is also quite good. Using the coils in conjunction with a mutual inductance bridge operating at 17 Hz and an Ithaco Dynatrac 391 Lockin Voltmeter, we are able to achieve a sensitivity of  $10^{-4}$  µhenry, which corresponds to a susceptibility of about 10<sup>-8</sup> emu. Calibration of the coils was first done by averaging the data obtained on powered CMN samples during the investigations of thermal equilibrium within the mixing These calibrations determine constants for the chamber. coils which relate unitless dial changes on the susceptibility bridge ratio transformer to mutual inductance changes within the coil due to the presence of samples. These measurements gave coil constants for coil #1 and #2 respectively as .0919  $\pm$  .0013 emu/dial unit and .0883  $\pm$  .0010 emu/dial unit.

It was later found necessary to determine the coil constant more accurately for the coil which was being used to take measurements on various samples. This was accomplished by utilizing a .87724 gm CMN single crystal, shaped into a cylinder, mounted so that the known susceptibility (perpendicular to its c axis) was being measured. The calibration obtained for coil #1 with this crystal was .0833 ± .0002 emu/dial unit.

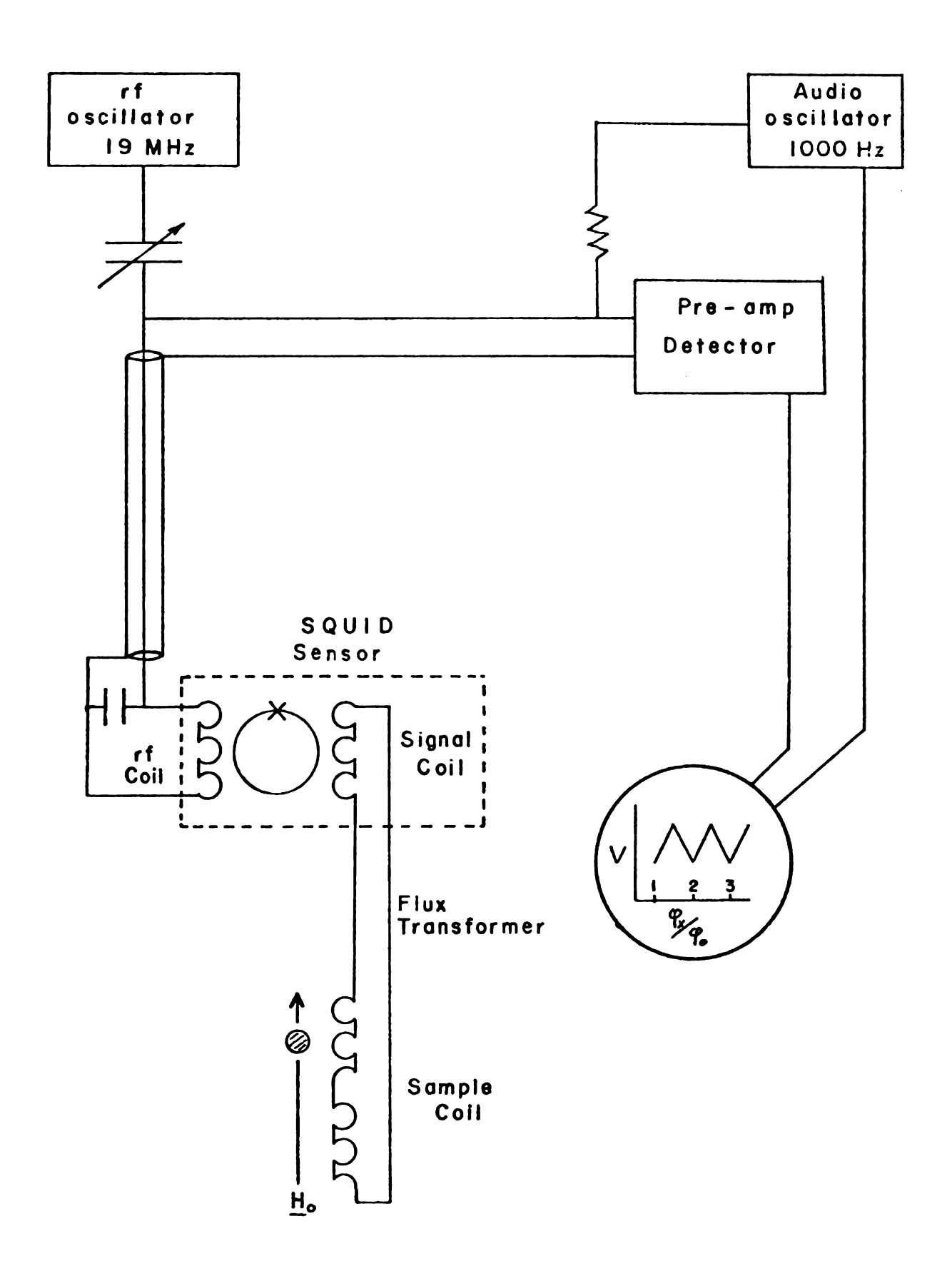
### The SQUID Magnetometer

The circumstances which eventually led to the development of the Superconducting Quantum Interference Device (SQUID) were initiated by B. D. Josephson 34 in his paper on the theory of tunneling currents between two superconducting materials separated by a thin insulating region. Josephson's theory predicted that even with zero voltage across the junction, a dc supercurrent could exist across the junction. This current could have any value from zero to a certain maximum value. If a nonzero voltage were applied to the junction, the dc supercurrent would still be present, but an ac supercurrent with an amplitude equal to the maximum possible dc supercurrent and a frequency 2 eV/M was superimposed on it. For practical purposes, a more convenient weak link connection, having properties similar to the thin insulation region, can be constructed by forming a point-contact between two superconductors.

A SQUID magnetometer is a device which utilizes the properties of a point-contact junction in a superconducting loop to measure very small changes in applied flux. A block diagram (Figure 13) shows schematically how this is achieved. A change in the magnetization of a sample will induce a current in the superconducting sample coil (comparable to the secondary windings of the conventional coil mentioned previously). Since the sample coil and signal coil comprise a superconducting circuit, this current will couple, via the signal coil, a flux into the SQUID sensor which contains the superconducting loop and point contact. Also coupled to the SQUID sensor is a rf tank circuit. voltage response of this tank circuit is periodic with changes in the total flux coupled into the SQUID sensor with the period being  $\phi_{O}$ , the unit of flux quanta ( $\phi_{O}$  =  $2 \times 10^{-7} \text{ gauss-cm}^2$ ).

The SQUID is normally operated in a "locked-on" mode. This is characterized by the use of a feedback circuit to stabilize the SQUID's operation at a particular dc flux level. The audio oscillator (1000 Hz) feeds a current into the rf coil and is adjusted so the external flux varies by  $\pm \frac{\Phi_0}{2}$  about the static dc flux. If the dc flux now changes due to a sample's magnetization being coupled to the SQUID sensor via the flux transformer, the feedback servo of the lock-in amplifier will put out a current proportional to this change. Stabilization of the dc flux level is accomplished by feeding

Figure 13. A block diagram of the SQUID magnetometer circuit. The SQUID sensor and sample coil are located inside the cryostat.



the current into the rf coil in order to counter the change in flux. The feedback current is monitored by a digital voltmeter. In this manner changes in the magnetization of a sample, and therefore its magnetic susceptibility, can be measured once the SQUID has been calibrated with a sample of known magnetization. A more rigorous treatment of the theory of point-contact SQUID magnetometers is presented in Appendix B. Most of the components of this SQUID system were manufactured by SHE Corporation. 35

The actual construction of the SOUID flux transformer and sample chamber was not done by the author; a more complete discussion of the SQUID system will be presented elsewhere. 36 However, it is essential to know the details of the SQUID sample chamber construction and its position relative to the CMN thermometer in the dilution refrigerator. This chamber was also designed for easy access to the samples with minimal disruption of the leak-tight seals necessary in the refrigerator. As such, it was built utilizing the glycerine-soapflakes glue described in a previous section. The SQUID magnetometer coil is wound on a form machined from Epibond 100-A epoxy, having a .254 cm inside diameter sample chamber region. The coil consists of two sections, each constructed of 21 turns of .0097 cm diameter niobium wire and wound in series opposition. The resulting sensitivity of the SQUID sensor is approximately  $10^{-2}$  flux quanta (~  $10^{-8}$  emu) for a 2.5 gauss field. The sample coil is coupled to a 117

turn signal coil located in the SQUID sensor by a pair of tightly-twisted niobium leads which are shielded by encasing them in high purity superconducting indium foil.

Figure 14 shows the sample chamber and its means of attachment to the refrigerator. The position of the SQUID chamber port in the refrigerator was shown in Figure 10. The samples are inserted into the SQUID coil on epoxy fingers with replacable tips designed specifically for a given sample or different orientations of the same sample. The coil and sample are entirely surrounded by a niobium superconducting shield used to trap the desired dc magnetic field at the sample site. This is accomplished when the cryostat is below 4.2 K by applying the appropriate field to the niobium cylinder with a magnetic-field solenoid wound on the inner vacuum can. The field is applied parallel to the cylinder's axis. The current producing the field is monitored by a digital voltmeter during the field application. When the field has reached the desired value, the niobium cylinder is heated to drive it into the normal state. The onset of the normal state can be seen by observing the resistance of a niobium sensor wire placed in close thermal contact with the niobium cylinder. After the niobium has become a normal conductor, the heat is removed allowing the niobium to again become superconducting, and in the process, trapping the applied field within the niobium cylinder. The external field is then turned off.

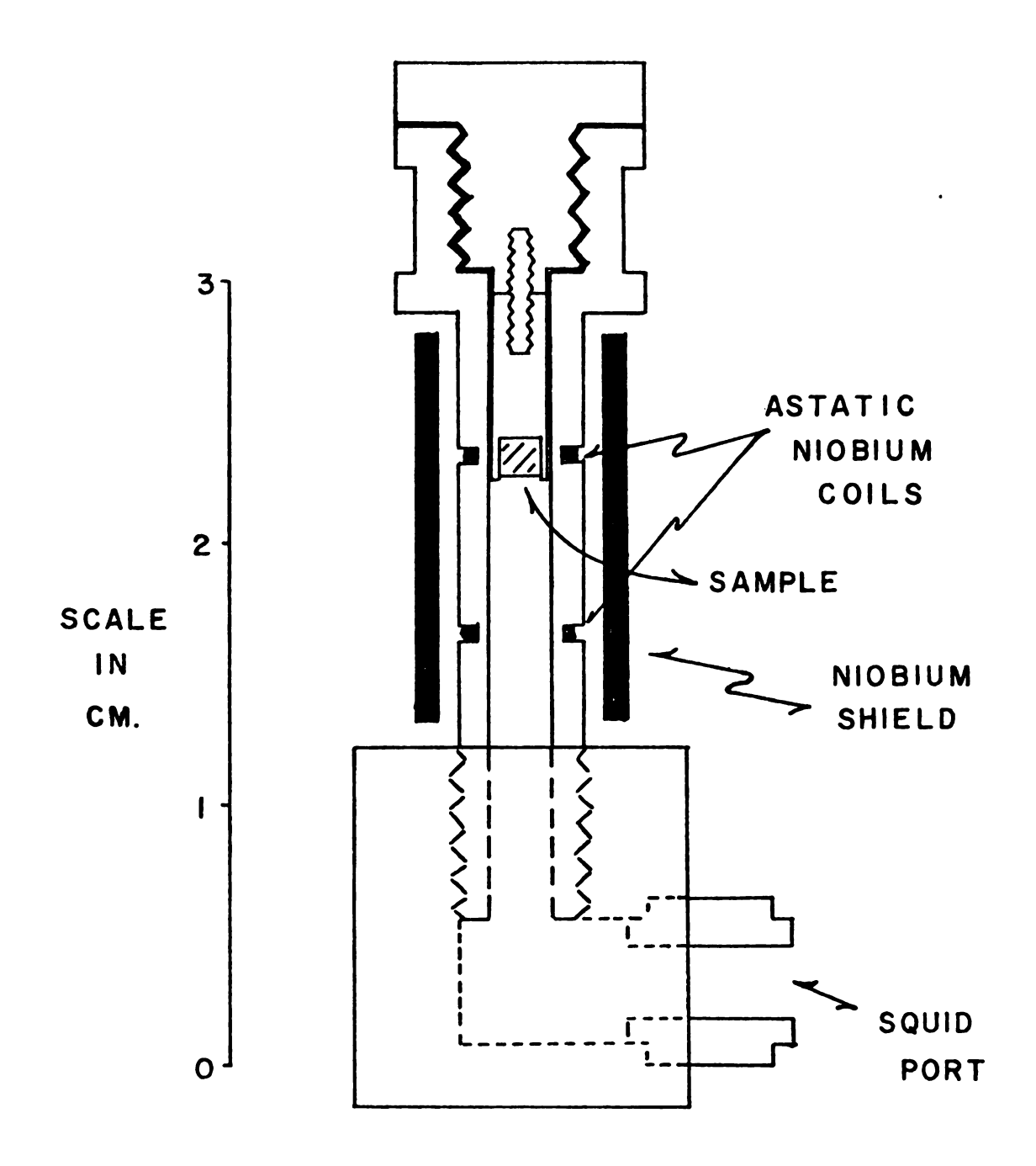


Figure 14. The SQUID sample chamber and its means of attachment to the mixing chamber's dilute solution return line.

There are several criteria which must be met when determining the magnitude of the magnetic field to be trapped in the cylinder. One must be certain that the field is not so large as to produce non-linear field effects in the susceptibility measurements. An estimation of these effects can be made by expanding the magnetization of a simple spin ½ system as given by the Brillouin function to the first non-linear term in the field (order H<sup>3</sup>). The applied field must be small enough so that at the lowest temperatures attainable this term will be insignificant. Such an expansion will result in a susceptibility of the following form:

$$\chi = \frac{Ng^2\mu^2}{4kT} (1 - \frac{1}{4} (\frac{g\mu H}{kT})^2)$$

From this expansion it can be seen that non-linear effects may occur due to the sample's having too large a susceptibility, or from the application of too large a field, or both. Therefore, care must be taken to be sure that the low temperature susceptibility being measured in the SQUID is indeed the zero-field susceptibility by an appropriate adjustment of the applied magnetic field. Of course the possibility of doing finite-field magnetization studies also exists for this system.

When the single crystals are being studied, further problems may arise, due to their size and shape. In general

the crystals should be as small as possible with respect to the diameter of the coils in order to minimize violations of the assumption that each sample can be considered to be a small dipole source. Also, the crystal shape may make demagnetization corrections necessary. These corrections are virtually impossible to calculate for most crystals shapes and are usually roughly estimated by assuming the crystal is an ellipsoid of revolution with axial ratios similar to those of the crystal. However, other methods can be used to estimate demagnetization effects, as will be shown later.

Even with these problems the SQUID proves to be an extremely valuable tool in the study of dilute magnetic systems, of samples which may be very expensive in quantity, and of small single crystals which may be difficult to grow to a size necessary for their use in more conventional magnetometers. In most instances it may not only be necessary, but desirable to use very small crystals for low temperature magnetic studies. Kapitza resistance between a crystal and the dilute solution, and poor internal heat transfer mechanisms may make it impossible to use a large crystal at low temperatures. Small crystals have a larger surface area per unit volume of material. Since Kapitza resistance varies inversely as the surface area, and the heat capacity is proportional to the volume, a small crystal will come into equilibrium with the surrounding dilute solution much sooner than a large crystal.

# E. Thermometry and Thermal Equilibrium within the Refrigerator

#### Thermometry

Low temperature thermometry in our system is by Curie law extrapolation of the susceptibility of powdered cerium magnesium nitrate (CMN). At high temperatures the measured CMN susceptibility is plotted as a function of the inverse absolute temperature. A least squares fit of this data yields a Curie constant for the thermometer. linear behavior with inverse temperature ( $\chi = C/T^*$ ) is then assumed to hold at low temperatures, allowing a magnetic temperature (T\*) to be measured. Recent investigations of the CMN temperature scale indicate this Curie law extrapolation, and therefore the condition  $T^* = T$ , to be valid to about 6 mK. Problems such as powder demagnetization effects on non-spherical thermometers are usually also present at these temperatures. Experimental studies have been made by A. C. Anderson<sup>37</sup> and by W. R. Abel and J. C. Wheatley<sup>38</sup> on the magnitude of the demagnetization corrections to cylindrical, powdered CMN thermometers. Estimations based on their measurements indicate that the magnetic temperature may be less than the absolute temperature by as much as .2 mK for a right circular cylinder thermometer with diameter equal to height. R. A. Webb et al. 39 have recently investigated these demagnetization effects further by comparing a similar

CMN thermometer with the temperature as measured by a Johnson device noise thermometer. They estimate the demagnetization correction to be 0 ± .12 mK in the range 8 mK to 20 mK. This means that at temperatures on the order of 10 mK the absolute temperature is most likely not known to better than 2% when powder thermometers are used. However, powder thermometers must be used in ultralow temperature experiments in order to minimize the effects of Kapitza resistance between the thermometer and dilute solution.

The means by which the CMN thermometer is tied to the absolute temperature scale at high temperatures, which must be done during each experiment, is to measure the CMN powder susceptibility against a <sup>3</sup>He gas-filled germanium resistor <sup>40</sup> calibrated in the temperature range .3 K to 3.0 K. important resistor was calibrated in the following manner. The germanium resistor, a 2 cm<sup>3</sup> He vapor pressure bulb, and a 2.9146 gm single crystal of CMN were placed in the refrigerator so as to be in good thermal contact with each other. The <sup>3</sup>He vapor pressure, measured with a mercury manometer and an MKS Baratron pressure meter 41 with a 0-30 mm Hg pressure head, was used to accurately determine the CMN's Curie constant over the temperature range .7 K to 3.0 K. This tied the absolute temperature as defined by the  $T_{62}$  He vapor pressure scale 42 to the magnetic temperature as measured by the CMN. The CMN was then used to calibrate the germanium resistor over the temperature range .3 K to 3.0 K.

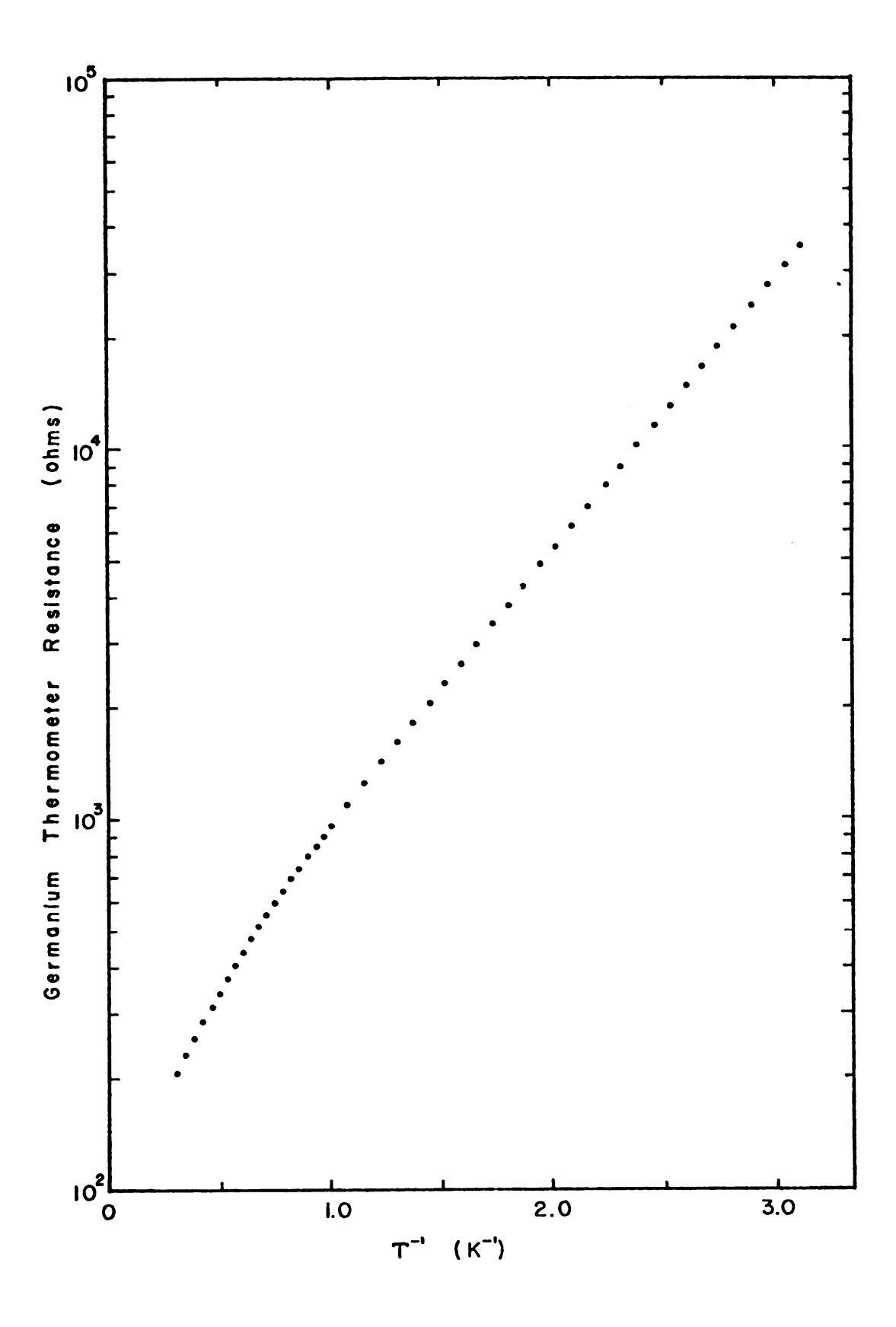
calibration is presented graphically in Figure 15, and is also tabulated in Appendix D. Once this resistor was calibrated it could be used in later experiments to calibrate CMN thermometers.

#### Thermal Equilibrium

A thermal analysis of the refrigerator was undertaken to investigate the possibility of a thermal gradient between the two sample positions in tail #1 and tail #2. Low temperature thermometers were constructed from CMN which had been put through a 45 micron sieve (sieve #325) to ensure a small grain size. In order to make the thermometers as nearly identical as possible, the two pills were simultaneously pressed into the shape of a .794 cm of a right circular cylinder with diameter equal to height. Their masses were determined to be .55555 gm and .55570 gm, resulting in filling factors of approximately 68%.

The temperature calibrations were carried out by cooling the refrigerator with a CMN pill in each tail and plotting the ratio of the temperatures determined by each thermometer against the temperature of one of them. As has been mentioned before, all these temperatures were determined from a least-squares fit of Curie's law in the temperature range .3 K to 3.0 K. Then the CMN thermometers were interchanged and the entire process repeated. Of course if the tails were in perfect thermal equilibrium and the thermometers identical,

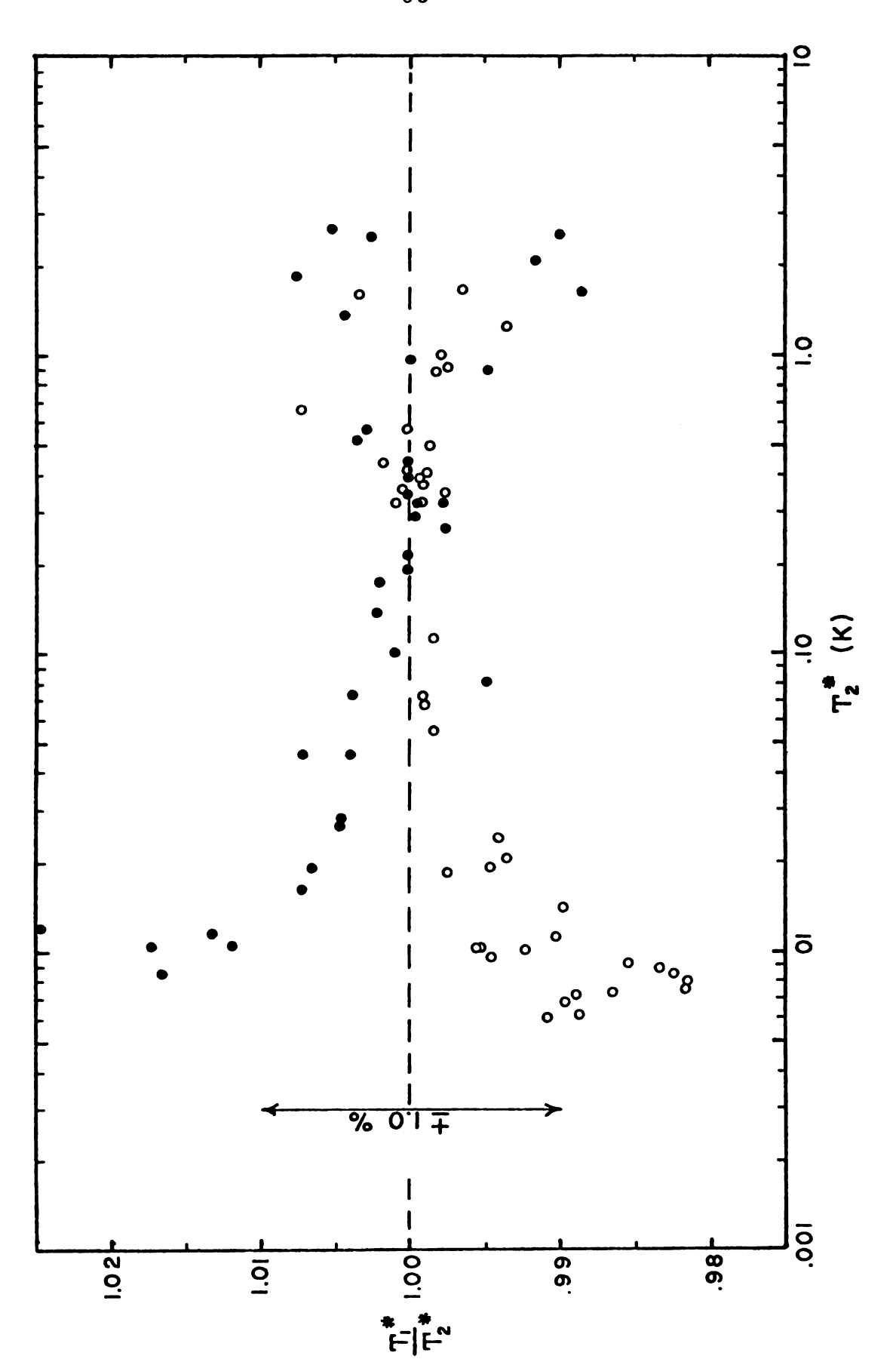
Figure 15. The results of the calibration of a germanium resistance thermometer against the absolute temperature in the range .3 K to 3.0 K.



one would expect  $T_1^*/T_2^*=1$  at all temperatures. Figure 16 shows the results of the calibration. This analysis indicated that some problem existed with CMN thermometers causing the temperature difference between the tails to reverse upon interchange of the thermometers. This implied that one or both CMN thermometers at low temperatures were giving incorrect temperatures for some unknown reason. However, the symmetry of these calibration experiments about the  $T_1^*/T_2^*=1$  line is evidence for thermal equilibrium between the tails.

The results of this temperature calibration and frustation over the long thermal relaxation times between the CMN thermometers and the dilute solution at low temperatures, which limited the lowest temperatures that we could reach usefully, led us later to change to a thermometer of powdered 90% lanthanum and 10% cerium magnesium nitrate. This powder was prepared by dissolving the pure lanthanum and cerium salts in water at a molar volume ratio of 9:1 respectively. The solution was allowed to slowly evaporate and deposit large crystals of nominal 90% LMN - 10% CMN. One well-formed crystal was then ground in a mortar and put through a 45 micron sieve in preparation for being pressed into pills. These 90% LMN - 10% CMN samples were made into .953 cm right circular cylinders with diameter equal to height and had masses of .90891 gm and .90837 gm. It is known that by lowering the density of cerium ions the Figure 16. Results of temperature calibrations of the refrigerator using 100% CMN thermometers. Open circles:  $M_1 = .55570$  gm CMN;  $M_2 = .555555$  gm CMN. Closed circles:  $M_1 = .555555$  gm CMN;  $M_2 = .55570$  gm CMN.

The subscripts refer to tail #1 or tail #2.



heat capacity of the powder can be reduced to the point where more rapid thermal equilibrium between the thermometer and dilute solution could be attained at low temperatures. 43

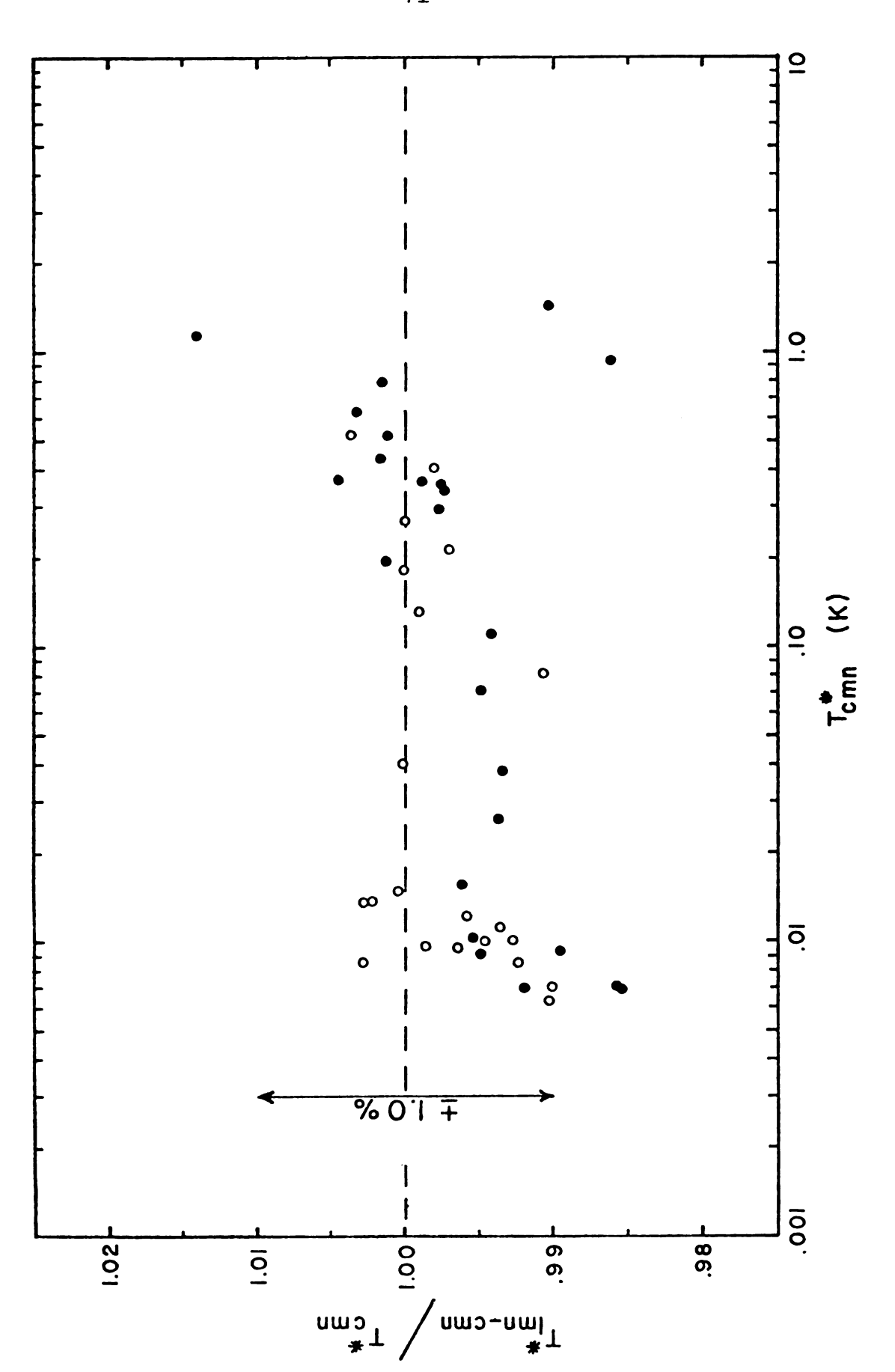
Initially a LMN-CMN pill was compared with the .55555 gm CMN thermometer. Careful measurements indicated that the CMN thermometer agreed with the LMN-CMN thermometer to within approximately .5% at a temperature of 10 mK and to within 1.5% at 7.0 mK (Figure 17). It was also very apparent that the relaxation time of the 100% CMN thermometer was considerably larger than the LMN-CMN thermometer. Later indirect measurements indicated to us that the .55570 gm CMN sample agreed with the LMN-CMN thermometer to 1.0% at 7.0 mK. This comparison was made by using two sets of susceptibility data obtained for a powder sample we were studying. For one set of data the .55555 gm CMN sample was used for the thermometer and the other data was obtained when the LMN-CMN was being used as a thermometer.

It is not known for certain why the temperature as determined by the two CMN thermometers were in disagreement with each other, but showed little disagreement when compared individually with LMN-CMN thermometers. However, the combined results of these experiments indicated to us that the temperature differences we had originally measured between the two tails were possibility due to the large thermal relaxation times of the 100% CMN powder pills. This explanation is consistent with the fact that

Figure 17. A comparison of the mixing chamber temperature as determined by 100% CMN and LMN-CMN thermometers. Closed circles: M<sub>1</sub> = .75444 gm

LMN-CMN; M<sub>2</sub> = .55555 gm CMN. Open circles represent an indirect comparison of .90891 gm

LMN-CMN and .55570 gm CMN.

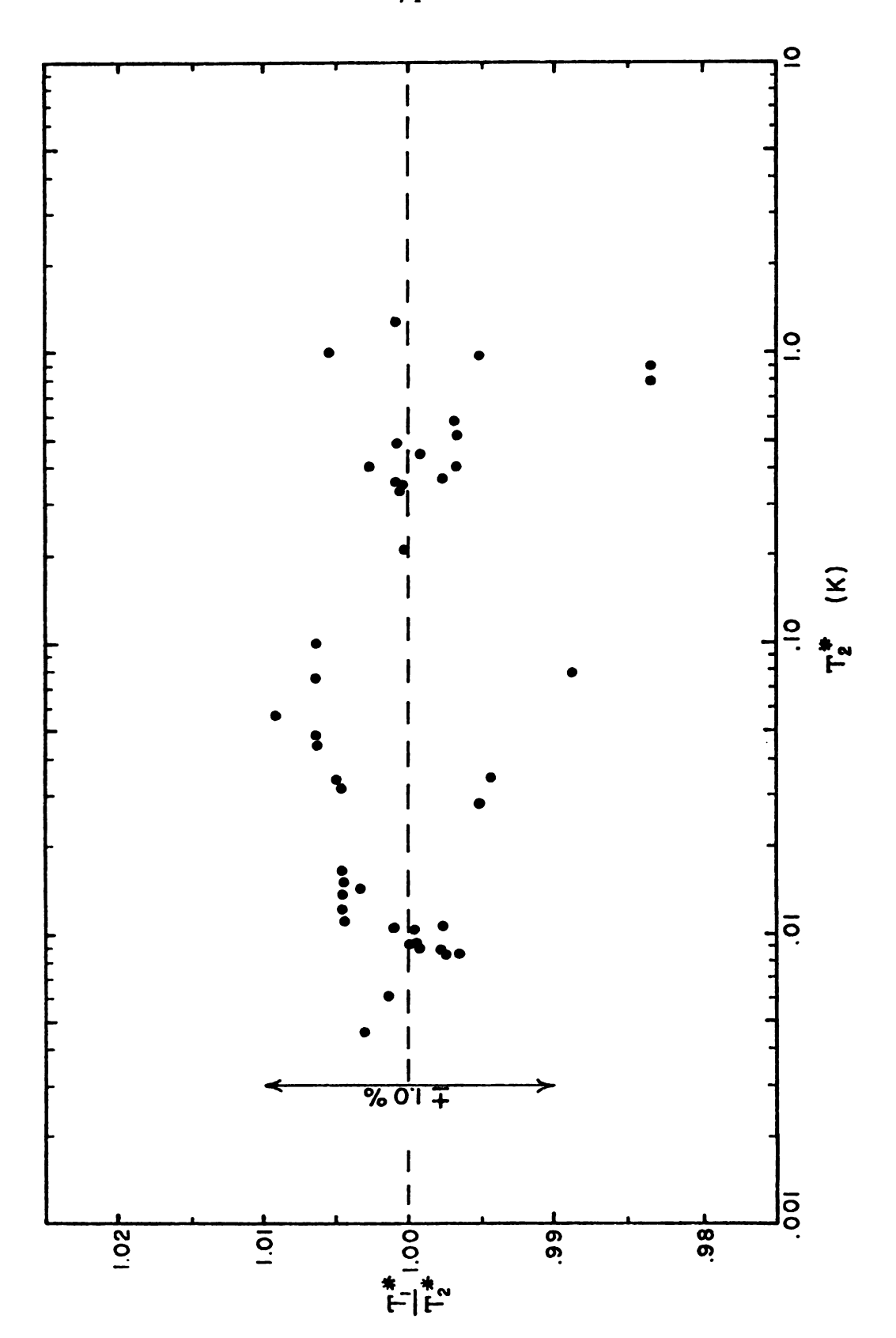


 $T_{LMN-CMN}^*/T_{CMN}^*$  < 1 over the low temperature region.

Since it was also apparent that the LMN-CMN pills had a relatively short relaxation time even at the lowest temperatures attainable by the refrigerator we were now confident that better thermometers could be made with this diluted CMN salt. The results of a subsequent recalibration of the refrigerator to check for possible thermal gradients between the tails using two LMN-CMN samples as thermometers is presented in Figure 18. These results, using much more reliable thermometers, conclusively show that no significant thermal problems exist due to the dual tail arrangement in spite of the presence of two phase separation levels in the refrigerator. It should be noted that most of the scatter in this high temperature data, as with the other calibrations, occurs above .8 K. This is very likely a result of temperature fluctuations in the <sup>3</sup>He-<sup>4</sup>He mixture which are apparent before and during the onset of phase separation. In each case the thermal calibrations indicate better thermal equilibrium immediately after phase separation occurred than existed before. The calibration shows that to a temperature below 5 mK we can still expect the temperatures in the two tails to agree within 1%.

In a typical experiment the conventional magnetic susceptibility coils will be operated at 1.6 gauss (20 mA amplitude current) in the region where calibration of the LMN-CMN thermometer is being done. This ensures the

Figure 18. Results of a temperature calibration of the refrigerator using LMN-CMN thermometers  $(M_1 = .90837 \text{ gm LMN-CMN}; \quad M_2 = .90891 \text{ gm LMN-CMN}. )$ 



necessary sensitivity to calibrate the dilute magnetic system against the germanium resistor. The field is then reduced to a .4 gauss field (5 mA amplitude current) before continuing to lower temperatures.

Thermometers made from dilute mixtures of CMN in LMN seem to be very promising as ultralow temperature thermometers. By increasing the nearest neighbor distance between cerium atoms in this manner one can lower the heat capacity of a thermometer so it can be more rapidly cooled at low temperatures. Also, this dilution process depresses the magnetic ordering temperature.<sup>2</sup> It is expected that the LMN-CMN thermometer's susceptibility will obey Curie's law to a lower temperature than 100% CMN although no direct experimental evidence is available to support this assump-This could possibly extend to lower temperatures the range over which such thermometers are useful (CMN is believed to begin deviating from Curie's law by about 6 mK). At the very least the comparison of the 100% CMN and 90% LMN - 10% CMN thermometers indicate that the LMN-CMN thermometers are no worse than 100% CMN in the temperature range over which we trust the 100% CMN thermometers. Further investigations of this material as an ultralow temperature thermometer will be carried out in the future.

Referring to the SQUID position in the refrigerator as shown in Figure 10, it should be noticed that the SQUID sample chamber is connected to the siphon tube return lines

at a distance of about 6.35 cm from the thermometer. As might be expected, this placement results in a temperature gradient from the thermometer to the SQUID sample at low temperatures due to viscous heating of the dilute solution as it flows from the thermometer to the SQUID port. Despite this fact, the SQUID must be placed at this point due to lack of space between the vacuum-can walls and the mixing chamber. Although this thermal gradient is undesirable, it can be dealt with easily. To further understand the nature of this thermal gradient, the temperature of the SQUID sample chamber was measured against the main LMN-CMN thermometer by using a small sample of powdered LMN-CMN (4.44 mg) in the SQUID. Originally a sample of 100% CMN was used in the squid for this calibration, but the thermal relaxation problems which became apparent with the pure CMN thermometer at ultralow temperatures in the mixing chamber convinced us to redo this calibration with the dilute CMN powder. The results of this calibration is shown graphically in Figure 19 where the inverse temperature as determined by the mixing chamber thermometer is plotted against the inverse temperature determined by the SQUID thermometer. Also, for comparison purposes, the theoretically derived estimation of the SQUID temperature based on siphon tube impedance measurements  $(Z \sim 6.4 \times 10^5/cm^3)$  is shown. The calculation has been carried out for two possible flow rates. At temperatures above 10 mK the <sup>3</sup>He flow rate through the SQUID siphon tube

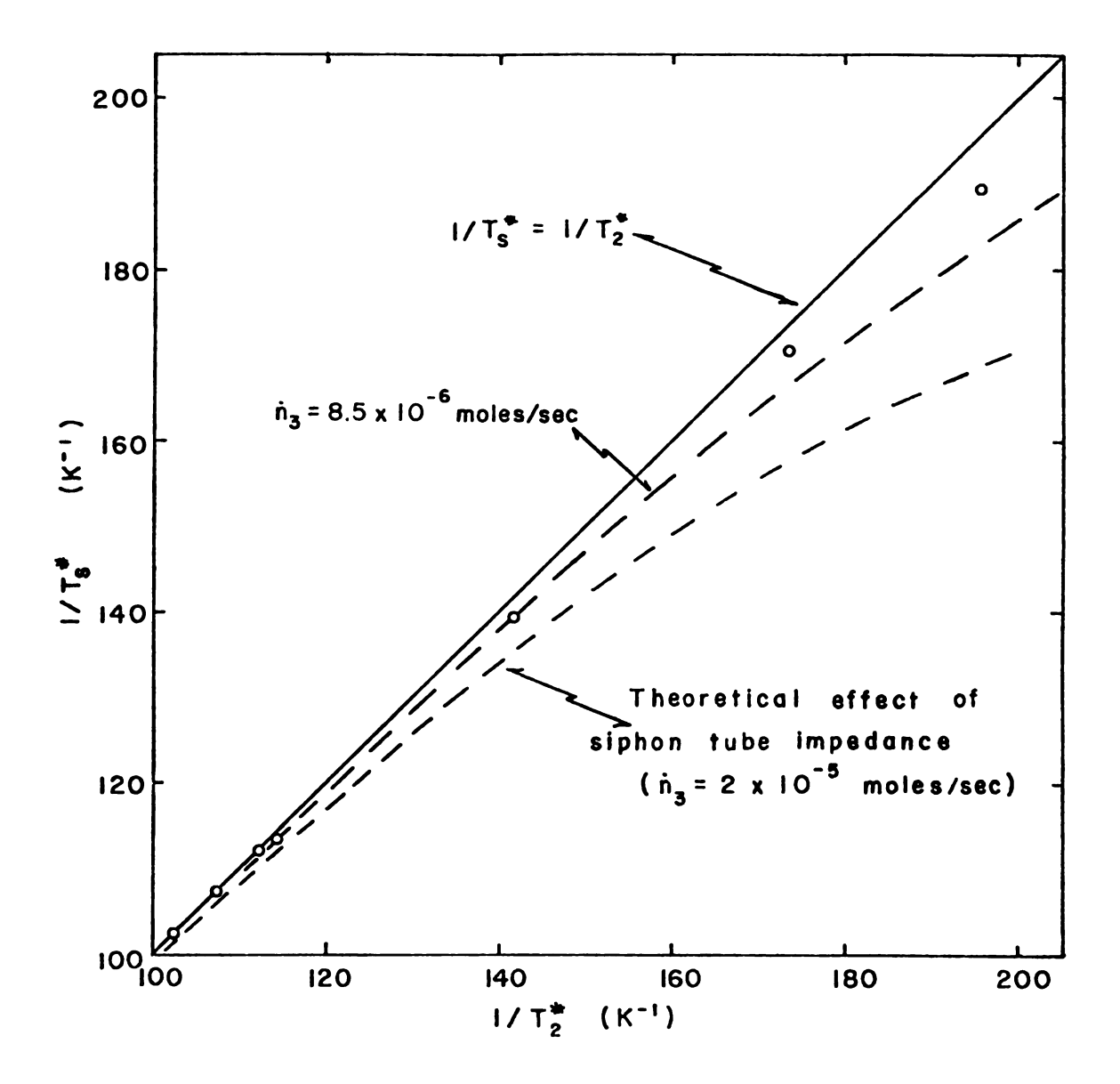


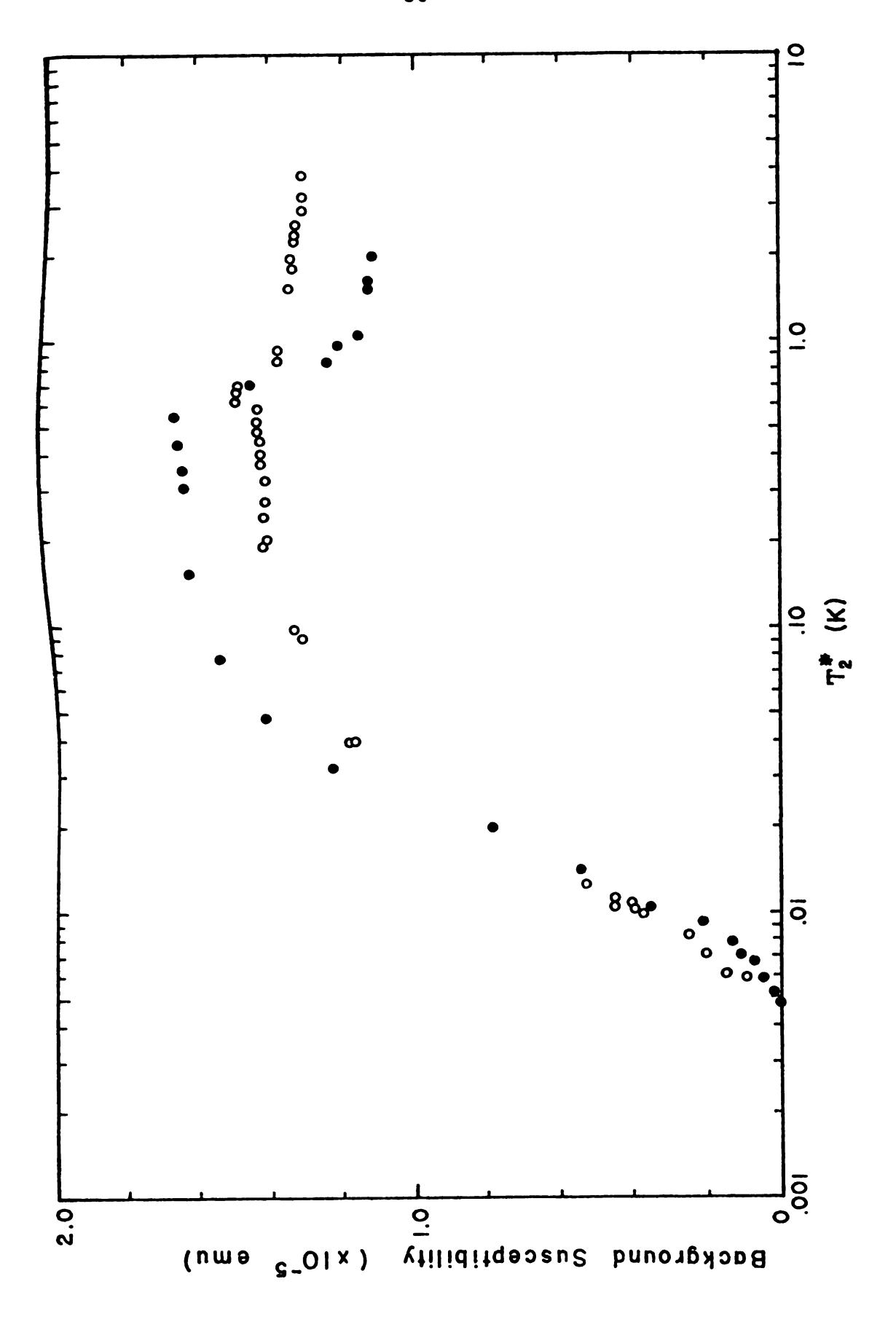
Figure 19. The inverse temperature at the SQUID magnetometer  $(1/T_s^*)$  as a function of the inverse temperature as defined by the LMN-CMN thermometer  $(1/T_2^*)$ . Dashed lines represent the theoretically estimated effects based on siphon tube impedance measurements.

is  $2 \times 10^{-5}$  moles/sec, but in the single-shot mode of operation below 10 mK the  $^3$ He flow rate while the refrigerator is cooling is reduced to about  $8.5 \times 10^{-6}$  moles/sec. However, even this flow rate will indicate a larger temperature gradient than is observed because at temperatures below 10 mK the refrigerator is brought into equilibrium to take a data point by further reducing the  $^3$ He circulation rate. Thus the theoretically calculated thermal gradient would overestimate this effect at the lowest temperatures. This calibration now allows one to define a SQUID temperature ( $T_S^*$ ) as a function of the magnetic temperature ( $T_Z^*$ ) in the thermometer tail of the mixing chamber. These temperature correction equations for the SQUID are shown in Table 5.

## Background Susceptibility Measurements

Further testing of the refrigerator in the form of background susceptibility measurements was required before any serious data analysis could be undertaken. The information obtained from the two background experiments is presented in Figure 20. These background experiments showed the presence of small paramagnetic impurities in each tail. The maximum correction due to these impurities is no larger than  $1.67 \times 10^{-5}$  emu. Also one of the tails, labeled tail \$1, exhibited a small diamagnetic shift at approximately T = 0.7 K. This is believed to be caused by the superconducting transition of a minute piece of aluminum foil which

Figure 20. The inherent background susceptibility of the mixing chamber. Open circles - tail #2; closed circles - tail #1. The coil constant used for coil #1 was .0833 emu/dial unit and for coil #2 was .0883 emu/dial unit.



was not machined away from the Epibond 100-A epoxy after it was molded. As with the thermal calibration graphs, the abscissa is plotted logarithmically to allow the entire temperature range to be easily scanned on a single graph. The background measurements have also been converted to correction equations which apply in specific temperature ranges. These equations, useful for computer analysis of raw data, are listed in Tables 2 and 3. The corrections for tail #1 are added to susceptibility measurements  $(\chi_1 \text{ corr.} = \chi_1 + \Delta \chi_1)$  while those for tail #2 are subtracted from the susceptibility measurements  $(\chi_2 \text{ corr.} = \chi_2 - \Delta \chi_2)$ . These corrections were applied to our previously presented temperature calibrations.

One further calibration experiment was made to determine the background susceptibility of the SQUID sample chamber. The results of this experiment for a 2.5 gauss trapped field are shown in Figure 21, and as with the mixing chamber background, indicates the presence of small number of paramagnetic impurities in the system. Table 4 lists the appropriate background equations and their range of validity. The corrected magnetic susceptibility is found from  $\chi_{\rm S}$  corr. =  $\chi_{\rm S} + \Delta\chi_{\rm S}$  \* H/2.5 where the background is assumed to be linear in the magnetic field, H. The background susceptibility was also measured at 25 gauss to ensure that this assumption was reasonable. The maximum correction term, assuming an arbitrary zero correction at  $1/T_{\rm S}^*=200$ , is 3.7

Figure 21. The background susceptibility of the SQUID sample chamber at an applied field of 2.5 gauss.

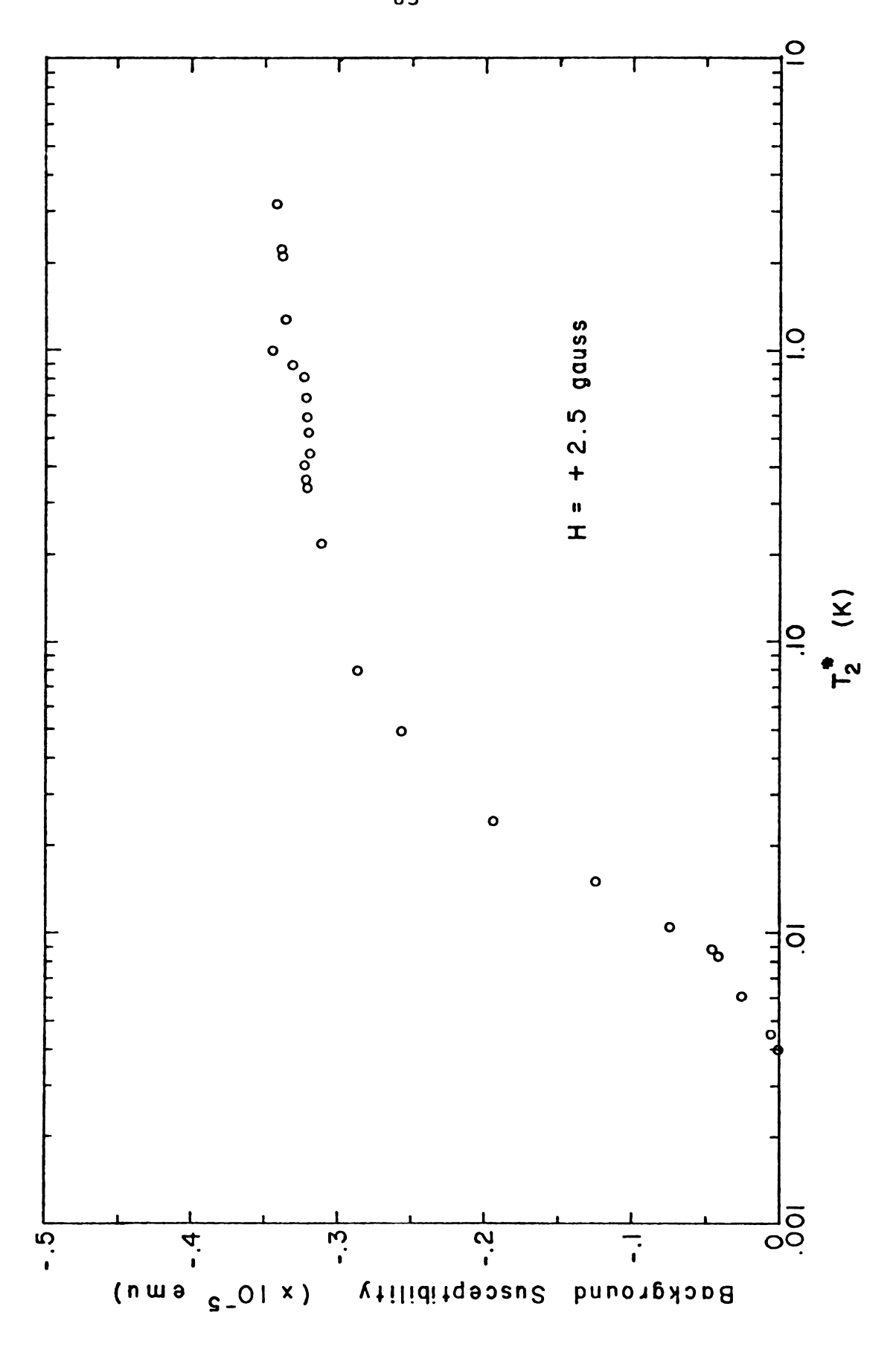


Table 2: Coil #1 Background Correction Equations

Background Correction (emu)	Temperature Range (K <sup>-1</sup> )
$\Delta_{\chi_{1}} = +1.08 \times 10^{-6} (1/T_{2}^{*}) +1.07 \times 10^{-5}$ $\Delta_{\chi_{1}} = +2.08 \times 10^{-6} (1/T_{2}^{*}) +1.00 \times 10^{-5}$ $\Delta_{\chi_{1}} = +1.21 \times 10^{-5} (1/T_{2}^{*}) -2.42 \times 10^{-6}$ $\Delta_{\chi_{1}} = -1.75 \times 10^{-7} (1/T_{2}^{*}) +1.70 \times 10^{-5}$ $\Delta_{\chi_{1}} = -1.98 \times 10^{-7} (1/T_{2}^{*}) +1.78 \times 10^{-5}$ $\Delta_{\chi_{1}} = -9.17 \times 10^{-8} (1/T_{2}^{*}) +1.23 \times 10^{-5}$ $\Delta_{\chi_{1}} = -2.67 \times 10^{-8} (1/T_{2}^{*}) +4.83 \times 10^{-5}$ $\Delta_{\chi_{1}} = 0.0$	0 < 1/T <sup>*</sup> <sub>2</sub> < 1.00 1.00 < 1/T <sup>*</sup> <sub>2</sub> < 1.23 1.23 < 1/T <sup>*</sup> <sub>2</sub> < 1.55 1.55 < 1/T <sup>*</sup> <sub>2</sub> < 6.40 6.40 < 1/T <sup>*</sup> <sub>2</sub> < 50.0 50.0 < 1/T <sup>*</sup> <sub>2</sub> < 108. 108. < 1/T <sup>*</sup> <sub>2</sub> < 195. 195. < 1/T <sup>*</sup> <sub>2</sub>

Table 3. Coil #2 Background Correction Equations

Background Correction (emu)	Temperature Range (K <sup>-1</sup> )
$\Delta\chi_{2}=+1.38\times10^{-6} (1/T_{2}^{*})+1.27\times10^{-5}$ $\Delta\chi_{2}=-6.62\times10^{-6} (1/T_{2}^{*})+2.56\times10^{-5}$ $\Delta\chi_{2}=-9.53\times10^{-8} (1/T_{2}^{*})+1.46\times10^{-5}$ $\Delta\chi_{2}=-1.43\times10^{-7} (1/T_{2}^{*})+1.49\times10^{-5}$ $\Delta\chi_{2}=-4.33\times10^{-8} (1/T_{2}^{*})+8.27\times10^{-5}$ $\Delta\chi_{2}=-0.0$	$0.0 \le 1/T_{2}^{*} \le 1.62$ $1.62 < 1/T_{2}^{*} < 1.70$ $1.70 \le 1/T_{2}^{*} \le 7.00$ $7.00 < 1/T_{2}^{*} \le 70.0$ $70.0 < 1/T_{2}^{*} \le 200.$ $200. < 1/T_{2}^{*}$

Table 4: SQUID Background Equations (H=.25 gauss)

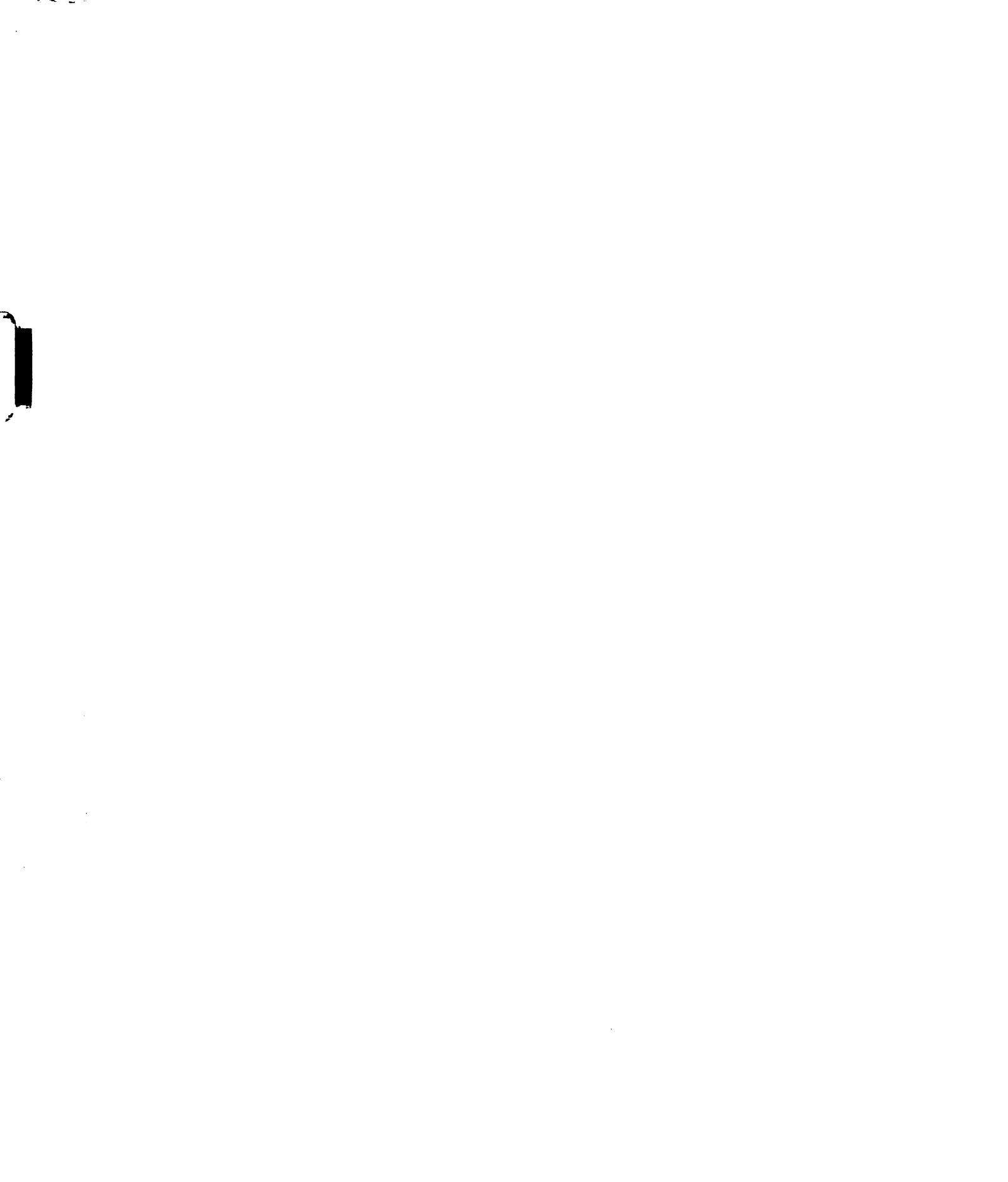
$\Delta \chi_{s} = -3.73 \times 10^{-6} (1/T_{2}^{*}) - 3.71 \times 10^{-6}$ $\Delta \chi_{s} = +1.07 \times 10^{-7} (1/T_{2}^{*}) - 3.44 \times 10^{-6}$ $\Delta \chi_{s} = -3.63 \times 10^{-7} (1/T_{2}^{*}) - 3.44 \times 10^{-6}$ $\Delta \chi_{s} = -3.63 \times 10^{-7} (1/T_{2}^{*}) - 3.44 \times 10^{-6}$ $\Delta \chi_{s} = -3.63 \times 10^{-7} (1/T_{2}^{*}) - 3.44 \times 10^{-6}$ $\Delta \chi_{s} = -3.63 \times 10^{-7} (1/T_{2}^{*}) - 3.44 \times 10^{-6}$ $\Delta \chi_{s} = -3.63 \times 10^{-7} (1/T_{2}^{*}) - 3.44 \times 10^{-6}$ $\Delta \chi_{s} = -3.63 \times 10^{-7} (1/T_{2}^{*}) - 3.44 \times 10^{-6}$ $\Delta \chi_{s} = -3.63 \times 10^{-7} (1/T_{2}^{*}) - 3.44 \times 10^{-6}$ $\Delta \chi_{s} = -3.63 \times 10^{-7} (1/T_{2}^{*}) - 3.44 \times 10^{-6}$	Background Correction (emu)	Temperature Range (K <sup>-1</sup> )
$\Delta \chi_{s} = +1.19 \times 10^{-6} (1/T_{2}^{*}) - 4.66 \times 10^{-6}$ $\Delta \chi_{s} = +5.07 \times 10^{-8} (1/T_{2}^{*}) - 3.31 \times 10^{-6}$ $\Delta \chi_{s} = +3.42 \times 10^{-8} (1/T_{2}^{*}) - 3.29 \times 10^{-6}$ $\Delta \chi_{s} = +2.61 \times 10^{-8} (1/T_{2}^{*}) - 2.98 \times 10^{-6}$ $\Delta \chi_{s} = +1.59 \times 10^{-8} (1/T_{2}^{*}) - 2.25 \times 10^{-6}$ $\Delta \chi_{s} = +3.48 \times 10^{-9} (1/T_{2}^{*}) - 8.28 \times 10^{-7}$ $1.02 < 1/T_{2}^{*} \le 1.02$ $1.02 < 1/T_{2}^{*} \le 1.19$ $1.19 < 1/T_{2}^{*} \le 2.48$ $2.48 < 1/T_{2}^{*} \le 38.0$ $38.0 < 1/T_{2}^{*} \le 62.5$ $62.5 < 1/T_{2}^{*} \le 115.$ $115. < 1/T_{2}^{*}$	$\Delta\chi_{s} = -3.73 \times 10^{-6} (1/T_{2}^{*}) - 3.71 \times 10^{-6}$ $\Delta\chi_{s} = +1.07 \times 10^{-7} (1/T_{2}^{*}) - 3.44 \times 10^{-6}$ $\Delta\chi_{s} = -3.62 \times 10^{-7} (1/T_{2}^{*}) - 3.08 \times 10^{-6}$ $\Delta\chi_{s} = +1.19 \times 10^{-6} (1/T_{2}^{*}) - 4.66 \times 10^{-6}$ $\Delta\chi_{s} = +5.07 \times 10^{-8} (1/T_{2}^{*}) - 3.31 \times 10^{-6}$ $\Delta\chi_{s} = +3.42 \times 10^{-8} (1/T_{2}^{*}) - 3.29 \times 10^{-6}$ $\Delta\chi_{s} = +2.61 \times 10^{-8} (1/T_{2}^{*}) - 2.98 \times 10^{-6}$ $\Delta\chi_{s} = +1.59 \times 10^{-8} (1/T_{2}^{*}) - 2.25 \times 10^{-6}$	$0.0 \le 1/T_{2}^{*} \le .285$ $.285 < 1/T_{2}^{*} \le .780$ $.780 < 1/T_{2}^{*} \le 1.02$ $1.02 < 1/T_{2}^{*} \le 1.19$ $1.19 < 1/T_{2}^{*} \le 2.48$ $2.48 < 1/T_{2}^{*} \le 38.0$ $38.0 < 1/T_{2}^{*} \le 62.5$ $62.5 < 1/T_{2}^{*} \le 115.$

Table 5: Inverse SQUID Temperature as a function of  $1/T_2^*$ 

Inverse SQUID Temperature (K <sup>-1</sup> )	Temperature Range (K <sup>-1</sup> )
$1/T_{S}^{*} = 1/T_{2}^{*}$ $1/T_{S}^{*} = +.94444(1/T_{2}^{*}) + 6.11116$ $1/T_{S}^{*} = +.73476(1/T_{2}^{*}) + 45.41778$	$0.0 < 1/T_{2}^{*} \le 110.$ $110. < 1/T_{2}^{*} \le 189$ $189 < 1/T_{2}^{*}$

flux quanta, which corresponds to  $3.4 \times 10^{-6}$  emu at 2.5 gauss.

The high temperature data obtained during the thermal gradient calibration experiment is useful in calibrating the SQUID coils. A calibration constant of 9.1289 x  $10^{-7}$  emu/flux quanta was found for these coils for a field of .25 gauss.



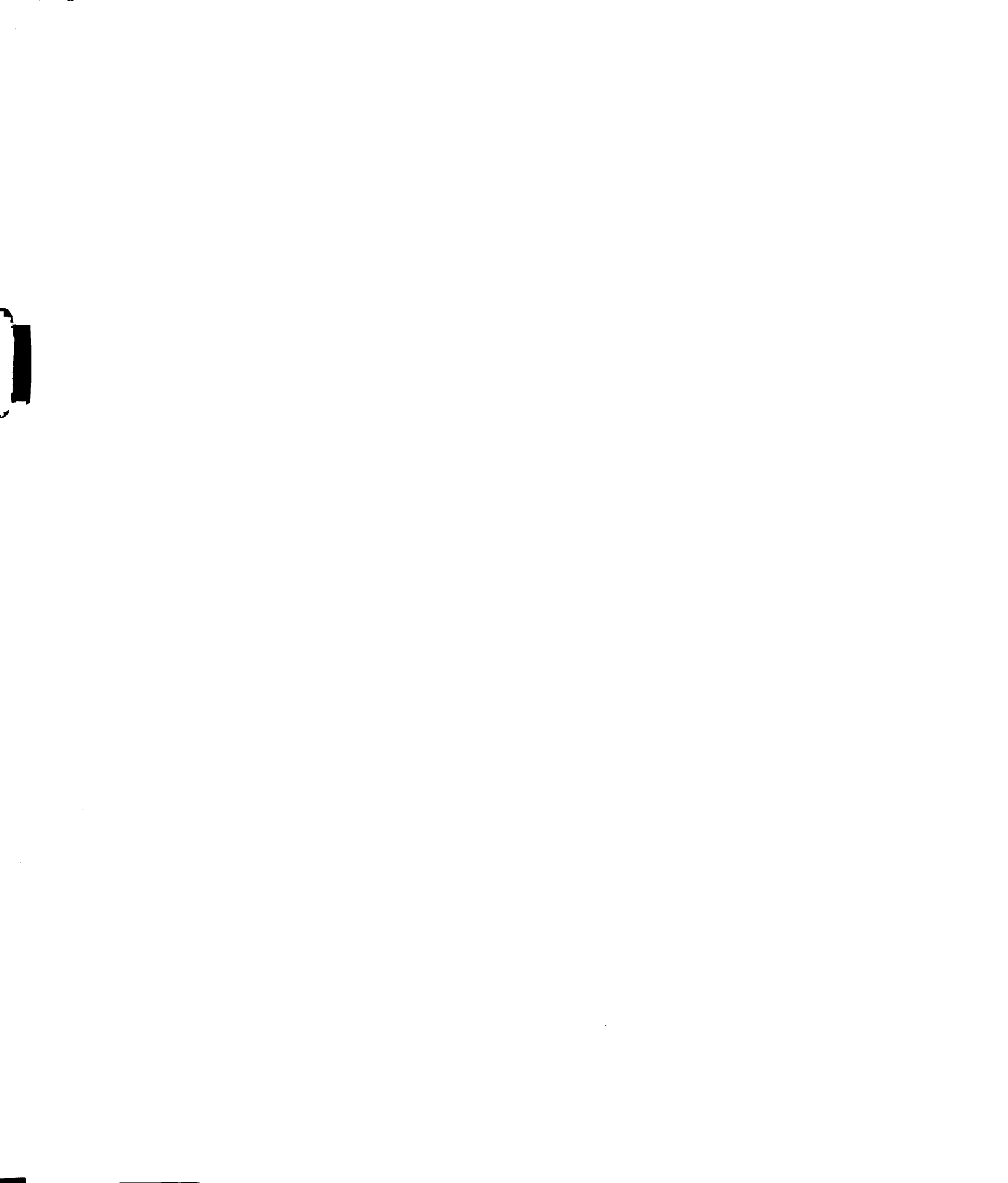
#### CHAPTER II

THE MAGNETIC SUSCEPTIBILITY OF COPPER TETRAPHENYLPORPHINE

## A. A General Survey of the Porphyrins

The structural base on which all porphyrins are built is the configuration called porphine. This basic molecular foundation consists of four nitrogen pyrrole rings interconnected by four methane-bridge carbon atoms, referred to as the  $\alpha$ ,  $\beta$ ,  $\gamma$ , and  $\delta$  meso-positions. The geometry of the molecule is planar, with hydrogen atoms attached to the four meso-positions and to the eight pyrrole sites as shown in Figure 22. The porphyrins are formed by substitution of various ligands at the hydrogen atom sites. Although no naturally occurring porphyrins are found with substitutions at the  $\alpha$  -  $\delta$  meso-positions, they invariably have substitutions at all eight pyrrole hydrogen atom sites. Only three of the many possible free porphyrins, that is, those which are not metal complexes, are found to occur in nature, these being present in leguminous plants and in urine under certain pathological conditions.

Metal complexed porphyrins 44, the metalloporphyrins (Fig. 23), are found to be more prevalent in nature and in fact are very important biologically especially as molecules involved in energy transfer processes. There are two means by which free porphyrins can take up a metal ion. One method involves the dissociation of the two central hydrogen



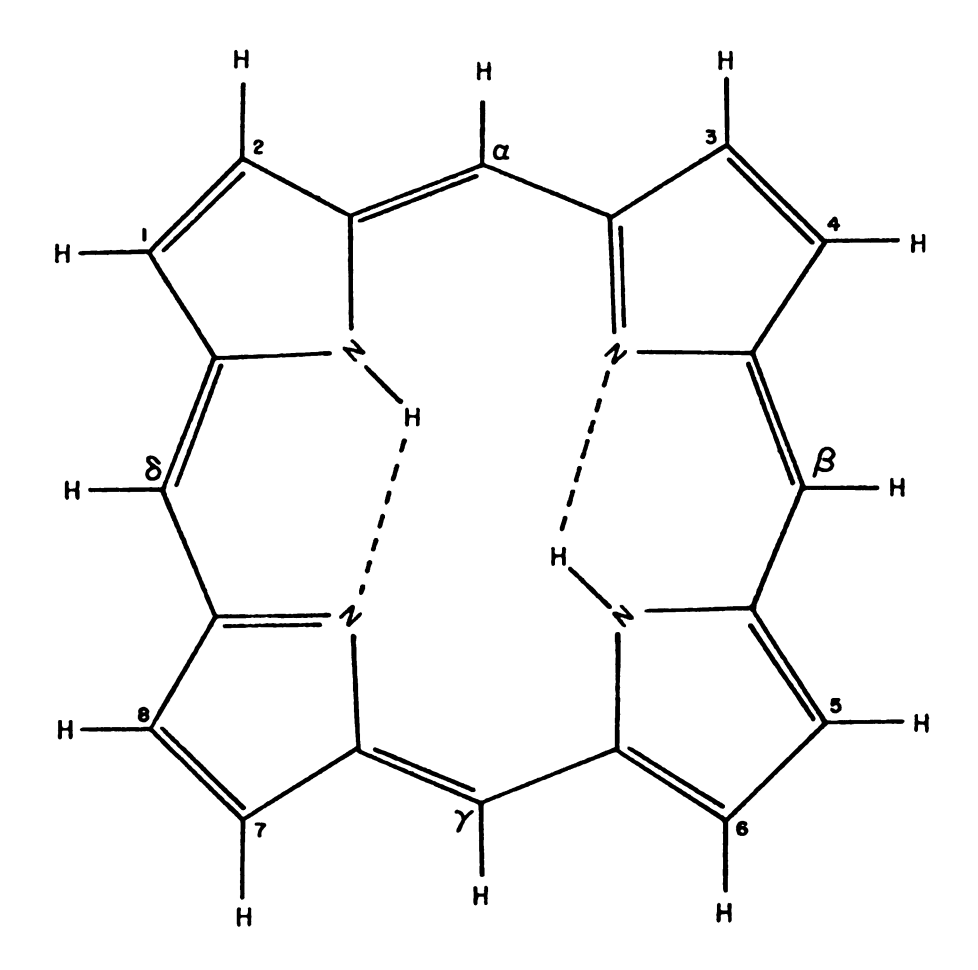
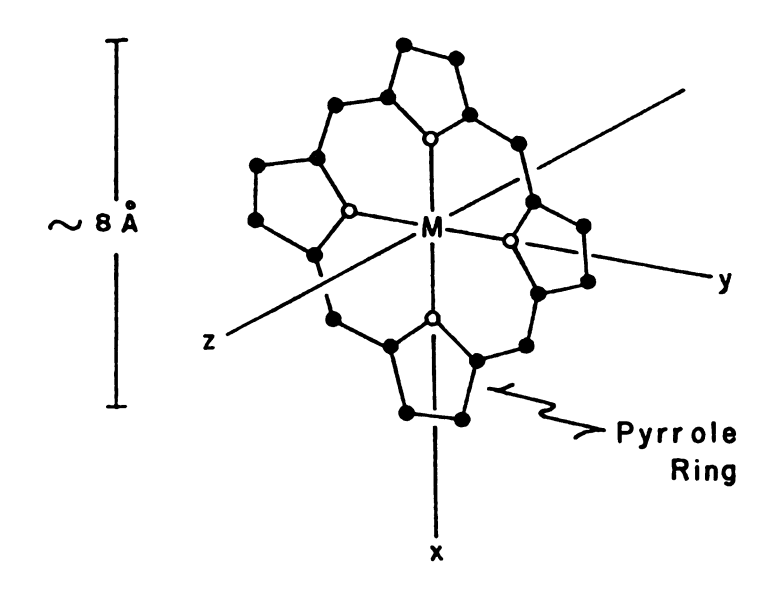
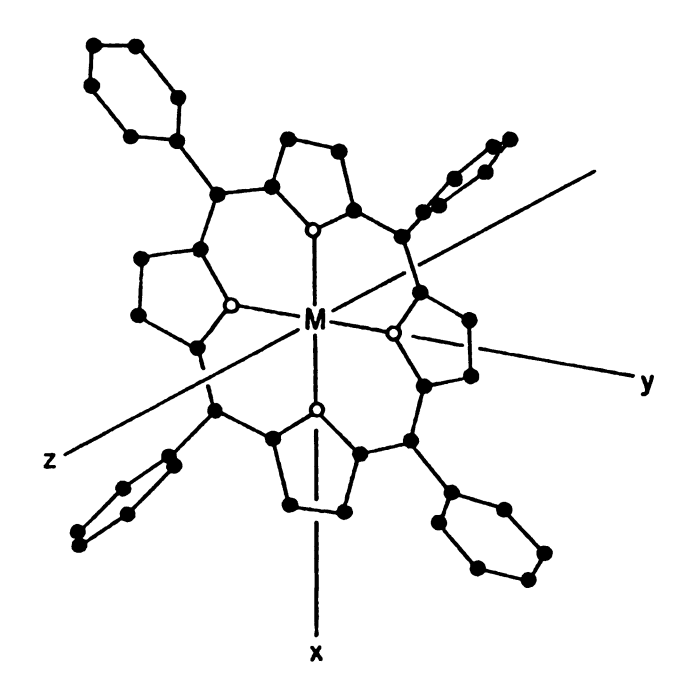


Figure 22. Structural representation of a porphine molecule. This structure forms the basis for all porphyrins.

Figure 23. A comparison between the structure of a metalloporphyrin and metallo-tetraphenylporphyrin
molecule. The site labeled M represents a
metal ion; open circles are nitrogen atoms
and closed circles are carbon atoms.



# **METALLOPORPHYRIN**



METALLO - TETRAPHENYLPORPHYRIN

nuclei from the porphyrin in solution followed by a metal ion - free porphyrin reaction. In the other method a complex is formed by the coordination of a metal ion with the two nitrogen atoms. This structure then stabilizes i tself by the total absorption of the metal ion and subseartent exclusion of the hydrogen nuclei. One of the most irreportant classes of porphyrins which can be produced is the iron complexes, which biologically are the haems. usefulness of the haem structure becomes apparent when the P roper protein side-chains are added to form haemoglobin, my oglobin, the cytochromes, etc. Another biologically s i quificant molecule results from replacing the hydrogen nuclei with a magnesium atom. This is not a true porphyrin, but a hydroporphyrin, since one of the pyrrole rings bonds is altered slightly. This molecule is either chlorophyll-a **∞** chlorophyll-b, depending on which substitution is made at the third coordination site. As is well known, chlorophyll is the pigment in leaves which converts sunlight into a useful form of energy for plants.

Another group of porphyrins can be formed which do not Occur in nature and are therefore synthetic porphyrins. This is done by introducing ligands at the  $\alpha$  -  $\delta$  meso-positions (Fig. 23). The first successful synthesis of  $\alpha$ ,  $\beta$ ,  $\gamma$ ,  $\delta$  - Tetraphenylporphine (TPP), the relevant ligands being phenyl rings, was reported by P. Rothemund and A. R. Menotti in connection with their studies of chlorophyll and

photosynthesis. Further work on the porphyrins led to a later paper 46 on the preparation of metal complexed salts. Three methods of preparing tetraphenylporphyrin metal complexes were presented, involving refluxing of the free base with the appropriate alkaline medium.

The spin density of a porphyrin crystal can be varied by attaching different ligands to the central porphine base, so that the volume occupied by an individual molecule is changed. This method of separating the paramagnetic ions is superior to the usual method of diluting paramagnets by replacing paramagnetic sites at random with an isostructural m lecule containing a diamagnetic ion. By increasing the 1 i gand size one can change the spin density in a uniform, controlled manner while retaining a regular crystalline Structure. Such a process could be very useful in the study magnetic interactions. For example a paramagnetic ion could be studied in a variety of crystalline structures. This would be possible, because the introduction of different Ligands at the  $\alpha$  -  $\delta$  meso-positions will generally not Seriously affect the intra-molecular environment of the ion. Alternatively, different electronic spin states of the same Paramagnetic ion could be studied in very similar crystal structures. This possibility arises because the net electronic moment of some paramagnetic ions in a porphyrin structure can be changed by the introduction of various ligands at the 5th and 6th coordination sites without

increasing the molecule's size to any appreciable degree.

Even in the more concentrated metalloporphyrins

(i.e. those with no attached ligands), the spin densities

are low enough that the intermolecular interactions will

be mainly due to weak, long range dipolar forces, with

cachange coupling usually being small in comparison to the

dipolar coupling. This means that most porphyrins will

likely have very low ordering temperatures and must be

tudied at ultralow temperatures if their magnetic behavior

to be determined completely.

Certain of these compounds may aid in future investigations into the nature of the anomalous thermal contact served between CMN and liquid <sup>3</sup>He at ultralow temperatures <sup>4</sup>.

The is phenomena is believed to be due to magnetic coupling tween the liquid <sup>3</sup>He and CMN at the liquid-solid interfece. Other surface studies would also seem feasible cause many porphyrins can be sublimated at about 300°C without destroying their molecular structure. The controlled sublimation of the surface layer of a crystalline porphyrin would result in a very clean surface for the investigations of interface phenomena. It should also be possible to construct thin films of porphyrin molecules for monolayer experiments by sublimation techniques.

## B. Copper $\alpha$ , $\beta$ , $\gamma$ , $\delta$ - Tetraphenylporphine

#### Introductory Remarks

Copper Tetraphenylporphine (CuTPP) is one of several metallo-tetraphenylporphyrin and metalloporphyrin compounds whose magnetic susceptibility has been measured with our apparatus. Magnetic susceptibility measurements a Long crystalline axes are invariably necessary if one is **t** ← obtain useful results. Since CuTPP was the first porphyrin which was successfully grown as a single crystal, i ts analysis was completed first and the results are reported here. The highly anisotropic hyperfine coupling hibited by the copper ion makes CuTPP a useful porphyrin with which to initiate a series of investigations into the tralow temperature magnetic properties of the porphyrins. The is anisotropic coupling dominates the magnetic susceptib i lity along the a and b crystalline axes at low temperares, while the intermolecular dipolar coupling dominates the susceptibility along the c axis. Thus these effects on the susceptibility can be observed approximately independently of each other. Since the influence of the hyperfine Coupling on the perpendicular susceptibility can be calculated, the low temperature behavior of CuTPP will yield useful information such as the thermal equilibrium of single crystals.

General instructions for the purification of CuTPP samples prior to the growth of single crystals will be given,

followed by the procedures used to grow the single crystals.

Similar procedures apply to the preparation of any of the

porphyrin samples for crystallization, the main difference

being the choice of solvents for a particular compound.

Although the preparation of CuTPP is not a difficult process in itself, the subsequent isolation of the pure complex from TPP may present problems that make the synthesis these compounds undesirable to many researchers. We are sateful to Dr. Richard Yalman and Mr. Gordon Comstock of tioch College for supplying us with our first porphyrin mples. Many of the porphyrins are now available from the chemicals Inc. 47. However, the method by which the popper complex of TPP is prepared is presented here.

The copper complex of TPP is easily prepared from TPP

first forming a solution of 500 mg of TPP in 50 ml of

loroform, then adding to this a hot solution of 200 mg of

pper acetate in 50 ml of glacial acetic acid. The

sulting mixture is heated in a Soxhlet refluxing apparatus

for two hours to insure complete metal ion replacement. The

solution is then concentrated to 50 ml and cooled to allow

microcrystals to precipitate.

# Purification and Crystal Growth

Before any attempts at growing crystals is made, it is advisable to purify the tetraphenylporphyrin complex in order to remove any impurities which may be present in

the form of tars. The presence of these tars is undesirable, not only because of their possible effects on magnetic susceptibility measurements, but also because they may present problems during crystal growth by providing too many nucleation sites. One of the major problems encountered while trying to grow large single crystals of CuTPP is that many microcrystals invariably grow instead of a few good single crystals. The removal of these impurities was found to be important, although their removal did not guarantee good crystal growth. The manner in which the CuTPP powder was

The sample was first put into solution with benzene. As

wi th most porphyrins, the solubility of CuTPP is rather low

in many solvents. This means that simply mixing a solvent

wi th CuTPP may not be sufficient to dissolve enough material

be of use. In order to increase the concentration of the

lution, it is refluxed for several hours in a Soxhlet

complexes is to use no more than 1 gram of the salt per liter

functions solvent. Generally, it is convenient to work with

Quantities on the order of 250 ml. After getting as much of

the salt into solution as possible, the solution is filtered

while still warm to remove the impurities. Filtering is

done through activated alumina contained in a sintered glass

disk filtration funnel. The alumina is 80-200 mesh, chrom
atographic grade and should be heated for several hours at

200°C to drive off any water which may be present. Filter paper should be used to prevent the alumina from lodging in the glass sintered disk.

After purification the solution must be further concentrated in preparation for crystal growing. There are two basic methods by which the crystals may be grown. In the first method, the solution is returned to the Soxhlet flask, but now the refluxing system is replaced by a condensing tube arrangement to trap the evolved benzene vapors.

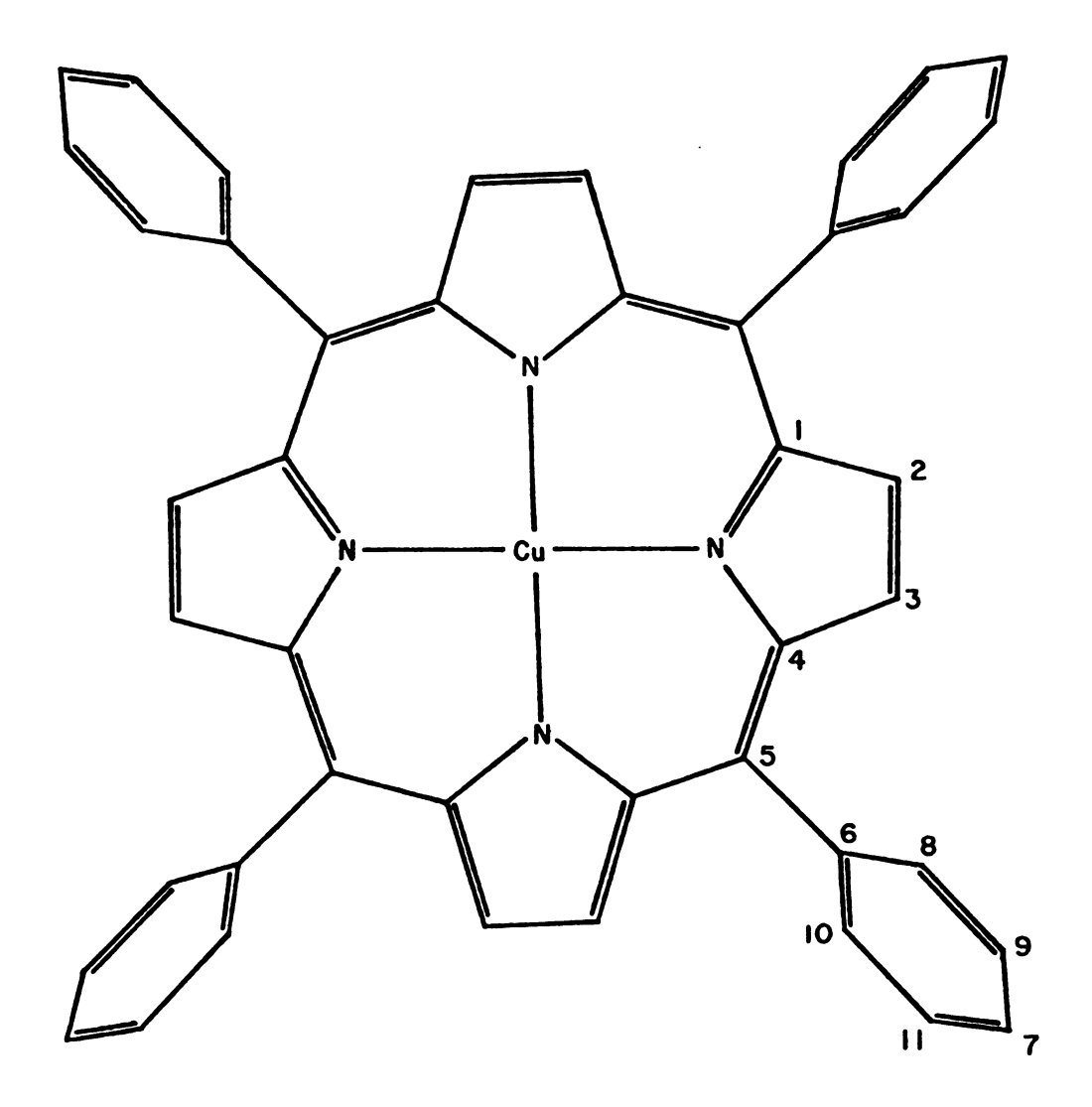
Assuming 250 ml is the original volume of the solution, it Should now be concentrated to about 60-80 ml. One way to d∈termine if the solution is concentrated enough is to look For the presence of small crystals just above the surface of the liquid on the walls of the flask. When this crystallization occurs, the solution should be removed, a small amount Of benzene added, and allowed to cool. The solution can then be transferred to small beakers for recrystallization. These beakers should be covered with a layer of parafilm with holes punched into it to adjust the evaporation rate. A close watch should be kept on beakers containing benzene as the solvent, since benzene vapors tend to decompose the parafilm cover within a few days. The beakers usually need to be cleaned of microcrystals every few days, and the best seed crystals transferred to a new beaker into which the solution has been filtered. It is often necessary to use a microscope to identify the good seed crystals.

The second method involves the partial replacement of the first solvent by a second solvent, in which the porphyrin has a much lower solubility. The effect is to put more material into solution in the second solvent than would normally be possible. Generally this solvent also has a much slower evaporation rate than the original solvent, which allows the crystal growth to be more easily controlled. As before, the original solution is returned to the Soxhlet flask for the concentration process. However, as the benzene is removed, it is slowly replaced by xylene until roughly an 8:1 ratio of xylene to benzene is obtained. amount of replacement does not seem to be critical. resulting mixture is then cooled and placed in parafilm covered beakers for crystal growth. It is much easier to regulate the rate of evaporation with this method and in some cases the evaporation rate is so slow as to not require a cover, although one is usually present to prevent dust from entering the beakers.

Cutppe crystals were found to grow relatively easily from a concentrated solution containing only benzene, with the major difficulty occurring while the technique of manipulating micro-seed crystals was being mastered. The crystals were large enough for our purposes after about two to three weeks. Microcrystals had to be removed from the beakers every two days to prevent them from twinning with the good crystals.

### The Structure of CuTPP

Molecules of CuTPP do not appear to have the exact planar structure exhibited by the basic porphine skeleton. The non-planarity exhibited by the porphyrin ring system containing a copper atom at the central position can best be seen by considering the deviations of various atoms with respect to a plane passing through the four nitrogen sites. This plane is found to be parallel to the (001) crystal plane. The copper atom is located at -.05 A below the plane, while the pyrrole carbon atoms labeled 2 and 3 in Figure 24 are located at +.20 A and -.13 A respectively. Therefore the pyrrole rings are slightly twisted out of the porphyrin plane. Fleisher et al. 48 have concluded from their work that the presence of the copper metal atom in the porphyrin structure is not the main reason for its non-planarity. Instead, they believe it is mostly a result of the desirability of a closely packed crystal structure, which is interfered with by the presence of the phenyl ligands. The close proximity of these ligands to the porphyrin plane apparently causes it to distort considerably. Further information about the relative positions of the porphyrin and phenyl rings can be obtained by referring to Figure 24. The phenyl rings, attached at the  $\alpha - \delta$  meso-positions, are tilted such that their plane is almost perpendicular to the (001) plane. The angle



The structure of copper tetraphenylporphine.

The relative positions of the numbered atoms

are indicated in the text and in Table 6.

between the  $C_5$ - $C_6$  carbon-carbon bond and its projection onto the (001) plane is  $13^\circ$ . Similarly, the projection of a line through the  $C_8$  and  $C_{10}$  carbon atoms makes an angle of  $72^\circ$  with this plane. Table 6 presents a more complete listing of the deviations of the atoms from a planar structure and some relevant bond lengths. Fleischer has also stated that the  $C_5$ - $C_6$  bond length of 1.51 Å is evidence for electronic isolation of the porphyrin ring and phenyl groups. However, this is apparently disputed by the ESR studies of CuTPP and its p-chloro derivative  $^{50}$ ,  $^{51}$ . These measurements tend to indicate that the phenyl rings are electronically coupled with the porphyrin ring resonance structure.

The Cu<sup>2+</sup> ion is a 3d<sup>9</sup> transition metal system (effective electronic spin S=1/2, nuclear spin I=3/2) and is contained in a square-planer tetracoorinate environment within the porphyrin ring. The nature of the bonds between the Cu<sup>2+</sup> ion and the pyrrole ring ligands can be quantitatively determined from molecular orbital theory using linear combinations of atomic orbitals<sup>52</sup>.

If two atomic orbitals overlap, two molecular orbitals are formed, one having a lower energy than the lowest energy atomic orbital and the other having a higher energy than both atomic orbitals. These molecular orbitals correspond to new electronic wave functions constructed from the addition and subtraction of the atomic wave functions. The

Table 6. The nonplanarity of a CuTPP molecule. The deviations of various atoms from the (001) plane passing through the copper ion are listed. Some relevant bond lengths are also tabulated 48.

Atom	Deviation from the Cu ion (Å)	Bond	Bond length (Å)
Cu	0.00	Cu-N	1.957 ± .013
N	04	N - C <sub>1</sub>	1.396 ± .013
C,	.26	N-C <sub>4</sub>	1.396 ± .013
C <sub>2</sub>	.23	C1- C5	1.427 ± .016
C <sub>3</sub>	09	C <sub>2</sub> - C <sub>3</sub>	1.335 ± .023
C <sub>4</sub>	24	C <sub>3</sub> - C <sub>4</sub>	1.427 ± .016
c <sub>5</sub>	42	C <sub>4</sub> - C <sub>5</sub>	1.398 ± .013
Ce	75		
C <sub>7</sub>	-1.42		

molecular orbitals derived from the addition of the atomic orbitals, called bonding orbitals, are mostly localized between the ion and ligand and are therefore mostly covalent in character. The molecular orbitals obtained from the subtraction of the atomic orbitals are antibonding orbitals because they are localized on the copper ion, and in fact resemble the free ion orbitals.

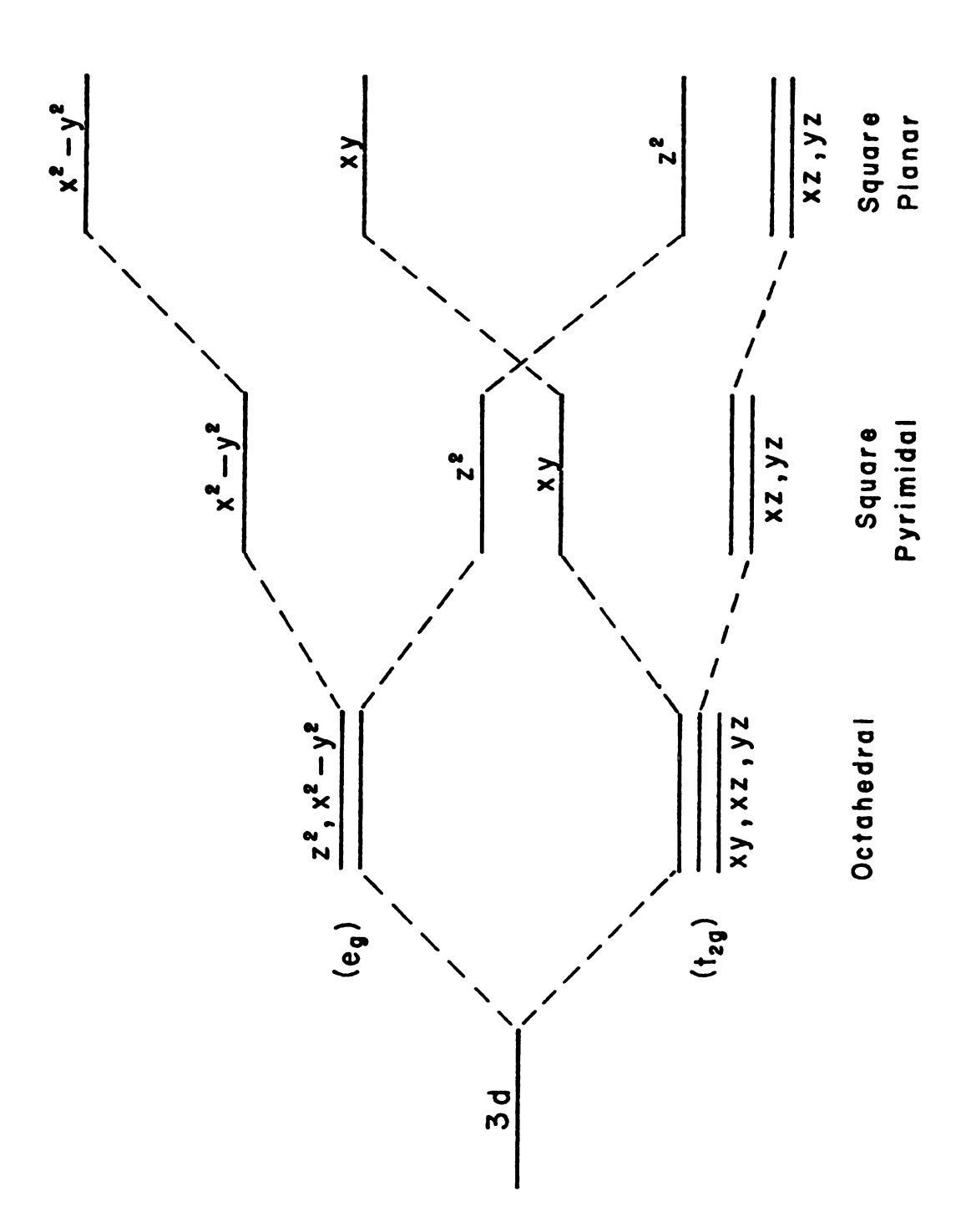
The five 3d orbitals that one would associate with the free copper ion, the  $d_{xy}$ ,  $d_{xz}$ ,  $d_{yz}$ ,  $d_{x^2-y^2}$ , and  $d_z^2$  orbitals are situated so the four lobes of the  $d_{x}^{2}$  orbital are pointing towards the four nitrogen atoms along the x and y This allows the  $d_x^2$ -v<sup>2</sup> orbital to form a very strong covalent bonding orbital with the sp 2 hybrid orbitals of the nitrogen pyrolle ligand. The unpaired electron of the CuTPP resides in the high energy antibonding  $\sigma$  orbital associated with this same combination. There seems to be no in-plane  $\pi$  bonding to the nitrogen atoms with the  $d_{xy}, d_{xz}$ , or  $d_{yz}$  orbitals. The effect of the filled  $d_z^2$ orbital, which points perpendicular to the plane of the nitrogen atoms, is to have a repulsive influence toward any ligands which may try to bond at the fifth or sixth coordination sites.

This is consistent with the crystal field theory approach to the energy of the 3d copper ion orbitals in the porphyrin structure. In this picture the 3d free ion orbitals are assumed to be located in a crystalline electric

field due to negative point charges whose symmetry is determined by the symmetry of the ligands surrounding the ion. The manner in which the energy of the five-fold degenerate 3d orbitals splits in crystalline fields of different symmetries is shown in Figure 25. The  $d_{\chi^2-y^2}$  orbital has the highest energy in the square-planar environment because its four lobes point directly toward the point charges. Therefore, the unpaired electron would again be expected to reside in this orbital. These energy levels of the crystal field theory approach correspond to the antibonding molecular orbitals found from molecular field theory.

The copper  $\alpha$ ,  $\beta$ ,  $\gamma$ ,  $\delta$  - tetraphenylporphine crystals grown from benzene were found to be tetragonal. The blue-violet crystals had highly degenerate faces at  $(0,\pm 1,\pm 1)$  and  $(\pm 1,0,\pm 1)$  giving the crystals the shape of a tetragonal bipyramid. A perspective drawing of the crystals illustrating the direction of the crystalline axes is shown in Figure 26. The crystals we grew were on the order of 1 mm<sup>3</sup> in size with the base of the pyramids being .1-.2 mm thick. The space group is  $I\bar{4}2d$  (No. 122 International Tables) and unit cell dimensions are  $a=15.03\pm.01\mathring{A}$ ;  $c=13.99\pm.01\mathring{A}$ . There are four molecules per unit cell (Z=4) for this structure, resulting in an 8.4 $\mathring{A}$  nearest neighbor distance within a crystal. Figure 27 indicates the positions of the copper sites in a unit cell and also

Figure 25. The manner in which the 3d orbital energy splits in crystalline field environments of different symmetry.



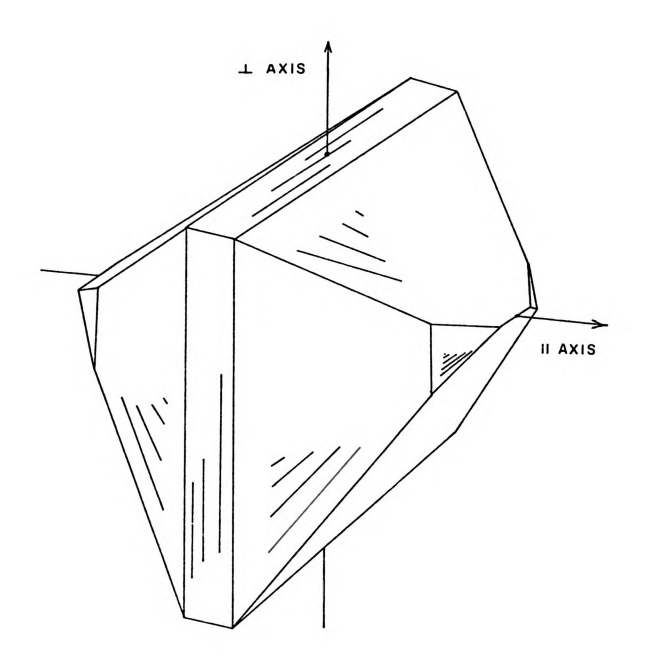


Figure 26. A perspective view of a CuTPP single crystal showing its relation to the crystalline axes.

Figure 27. A unit cell of CuTPP. The small squares around each copper site represents the porphyrin ring plane.

represents the planes of the porphyrin rings by small squares drawn around the copper atoms. The planes of all these porphyrin rings are situated perpendicular to the c axis, which is the four-fold axis of the crystal. This configuration determines a spin density in the magnetically concentrated single crystal of only 1.27 x  $10^{21}$  spins/cm<sup>3</sup>. The four-fold axis of a crystal is relatively easy to identify because it is perpendicular to the base of the bipyramid structure. The positioning of the porphyrin rings within a unit cell and the manner in which the nearest neighbor distance is increased due to the presence of the attached phenyl rings is shown by Figure 28, which is a projection of one unit cell on the (001) plane. Molecules which lie at different positions along the c axis are represented by different line structures in this drawing. The phenyl rings of any one molecule are tilted by 72° to the (001) plane and situated so as to lie over or under a neighboring molecule. Thus the effect of the phenyl ligands is to limit the distance of closest approach of the paramagnetic ions within the porphyrin rings and therefore reduce the intermolecular dipole-dipole and exchange coupling. The phenyl rings are believed by J. Assour<sup>51</sup> to diamagnetically shield one molecule from another, resulting in much less dipolar interaction broadening in ESR spectra than would ordinarily be expected for crystals of this magnetic concentration.

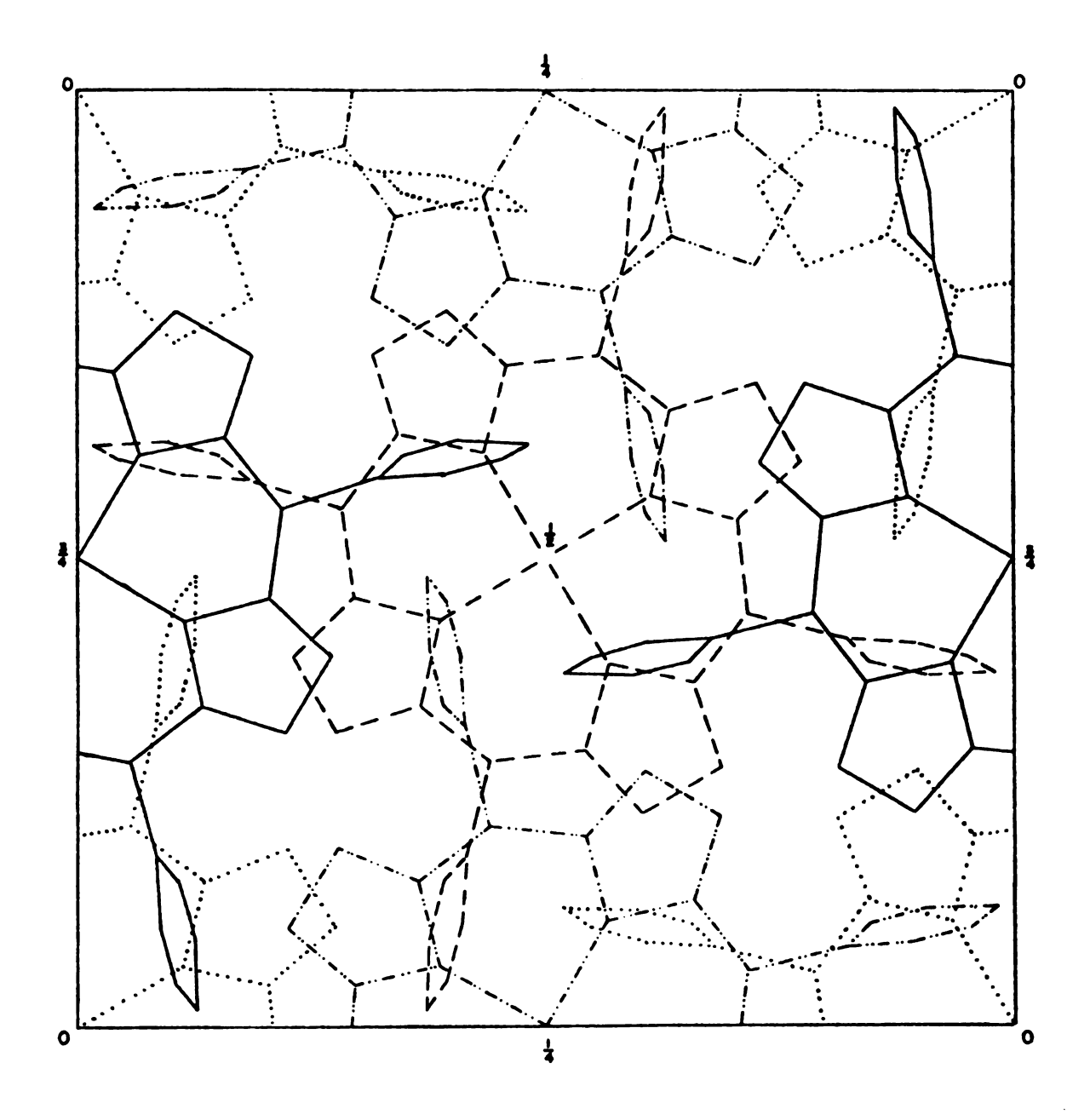


Figure 28. The projection of one unit cell of CuTPP on the (001) plane. Each line structure represents a different plane perpendicular to the c axis.

# C. Theory of the Magnetic Susceptibility of Copper Tetraphenylporphine

The application of a magnetic field to a material can result in a magnetization being induced in the material. The magnetic susceptibility is in general a tensor quantity which relates the induced moment per unit volume, or the magnetization, to the applied field:

$$\chi(\mathbf{T}) = \frac{\partial \mathbf{H}}{\partial \mathbf{H}}$$

In many materials, as in CuTPP, the induced moment is parallel to the applied field along at least one set of axes so that the magnetic susceptibility for that material becomes a scaler:

$$\chi_{\alpha}(\mathbf{T}) = \frac{\partial M_{\alpha}}{\partial H_{\alpha}}$$

where  $\alpha$  represents a component of the field. The magnetization of a quantum mechanical system can be expressed as:

$$\langle M_{\alpha} \rangle = \frac{1}{\beta V} \frac{\partial}{\partial H_{\alpha}} (ln z)$$

where  $\beta$  = 1/kT, V is the volume of the material, and Z is the partition function, which is proportional to the probability that a given energy state is populated. The partition function may be determined once the energy levels are known and is given by:

$$Z(T) = tr e^{-\beta H}$$

where H is the total spin-hamiltonian for the system.

We will first consider the general effective spin hamiltonian which can be used to describe the energy of the Cu<sup>2+</sup> ion in its molecular and crystalline environment and then decide which terms will make important contributions to the susceptibility. This hamiltonian has the form:

$$H_{i} = \underbrace{S \cdot g \cdot H}_{z} + \underbrace{S \cdot A \cdot I}_{z} + \underbrace{\sum_{n=1}^{4} S \cdot A_{n} \cdot I_{n}}_{n=1} + D\{S_{z}^{2} - 1/3S(S+1)\}$$

$$+ Q\{I_{z}^{2} - 1/3I(I+1)\} + \underbrace{I \cdot g_{N} \cdot H}_{j} + \underbrace{\sum_{j}^{j} H_{ij}}_{j}$$

from which the total spin hamiltonian for the crystal can be obtained by a sum over all copper ion sites  $(H = \sum_{i} H_{i})$ . Although this general expression is quite complicated, it can be simplfied to some extent for CuTPP. It should be mentioned that the spin hamiltonian is inherently an approximation to the actual hamiltonian of an ion in a crystalline electric field potential. The manner in which this approximation is made will be briefly outlined below. The individual terms will then be explained and discussed in the following paragraphs as they relate to CuTPP. A more detailed discussion of the effective spin hamiltonian can be found by referring to G. E. Pake  $^{53}$  and W. Low  $^{54}$ .

In the absence of spin-orbit interactions the crystal field interaction will quench the orbital angular momentum

(i.e.  $\langle n|L|n\rangle = 0$ ) and therefore quench the magnetic moment of the copper ion. The effect of the spin orbit interaction, which is much weaker than the crystal field interaction in this case, is to reintroduce a small amount of orbital angular momentum into the system. The energy of the electron in a magnetic field is not changed to first order by the spin-orbit coupling, but a second order calculation does yield an energy shift due to the perturbative admixing of excited orbital sites. It is found that this effect can be included in a spin hamiltonian formalism by assuming the electron to have its free value electronic spin (S=3) and to couple with an external magnetic field via an anisotropic tensor  $(\tilde{S} \cdot \tilde{g} \cdot \tilde{H})$ . This is the electronic Zeeman interaction term of the spin hamiltonian. Because of the axial symmetry associated with a square-planar environment, the g tensor is also axially symmetric allowing the Zeeman interaction to be expressed in terms of  $g_{||}$ , the principal value of the q tensor perpendicular to the porphyrin ring (parallel to the c axis) and  $g_{\parallel}$ , the isotropic value of the g tensor in the plane of the porphyrin ring (perpendicular to the c axis). The Zeeman term now becomes:

$$H_{Zee} = g_{\parallel \parallel}^{\mu} S_z^{H}_z + g_{\perp}^{\mu} (S_x^{H}_x + S_y^{H}_y)$$

where  $\mu$  is the Bohr magneton.

Another term which arises from this perturbation analysis of spin-orbit coupling is the crystal field term  $(D\{S_z^2 - 1/3S(S+1)\})$ . This term represents the effect of a splitting of the electrons orbital ground state due to the spin orbit coupling in the crystalline field environment.

The form in which it appears here is valid only if the crystalline field environment possesses axial symmetry, which is the case for the square-planar coordinated copper ion in CuTPP. Since the crystal field interaction does not split the energy levels for a spin \( \frac{1}{2} \) system, it does not have to be considered in a discussion of CuTPP.

Two of the terms in the general equation can be eliminated because their interaction energies are always small compared to the temperature at which we are experimentally able to investigate the magnetic susceptibility of this material. The nuclear Zeeman interaction  $(S \cdot g_N \cdot I)$  expresses the coupling of the copper nuclear moment to the applied external field. However, the nuclear magnetic moment, being on the order of 2000 times smaller than the electronic moment guarantees this term will always be small. The quadrupole interaction  $(Q\{I_Z^2 - 1/3I(I+1)\})$  is a result of the coupling between the nuclear electronic quadrupole moment and the gradient of the crystalline electric field at the nucleus. An upper bound on the strength of this interaction, obtained experimentally by

3

Đ

þ:

:.

Th th

at

S.

Bài àct P. T. Manoharan and M. T. Rogers  $^{55}$ , is  $Q \le 4 \times 10^{-4}$  cm  $^{-1}$ . This corresponds to a temperature  $T \le .58$  mK. At the very lowest temperatures which we can obtain, the magnitude of the interaction which this term represents could be sufficient to make it observable. An estimation of its effect, assuming the to-be-mentioned hyperfine coefficient, B, equal to zero, has shown it to produce no contribution to the parallel susceptibility. It is also found that in the same approximation the quadrupole interaction increases the perpendicular susceptibility by .4% at 20 mK and 1.5% at 10 mK. It should be emphasized that this is the maximum effect possible because Q was assumed to equal the upper bound value  $4 \times 10^{-4}$  cm  $^{-1}$  for this calculation.

The result to this point is that for CuTPP the hamiltonian is of the form:

$$H_{i} = \underbrace{s \cdot g \cdot H}_{z} + \underbrace{s \cdot A \cdot I}_{z} + \underbrace{\sum}_{n} \underbrace{s \cdot A}_{n} \cdot I_{n} + \underbrace{\sum}_{j} H_{ij}$$

The magnitude of these interactions is sufficient to allow the possibility that any or all of them may be significant at 10 mK.

Of the remaining terms that have not yet been mentioned,  $S \cdot A \cdot I$  represents the copper electronic spin-nuclear spin interaction, 56,57 i.e. the hyperfine coupling. In the same manner as was seen for the Zeeman term, the hyperfine interaction tensor may be expressed in terms of the principal

values of a hyperfine interaction tensor perpendicular and parallel to the porphyrin ring allowing the hyperfine term to become:

$$H_{\text{hyp}} = AS_zI_z + B(S_xI_x + S_yI_y)$$

where A and B are the hyperfine coefficients parallel to and perpendicular to the c axis respectively. The magnitude of the coefficients in this term and the other interactions relevant to CuTPP are listed in Table 7.

Of the remaining two terms, one represents the superhyperfine coupling between the copper electron and the nuclear spin of the attached pyrrole rings' nitrogen atoms  $(\sum_{n=1}^{7} S \cdot A_n \cdot I_n)$ . The magnitude of the interaction energy, on the order of 2.5 mK, is significant at low temperatures. An exact calculation of the effect of this term is extremely difficult, but an estimation was made by utilizing the Laplace transform computational method presented by P.H.E. Meijer<sup>58</sup> (assuming the hyperfine coefficient, B, was zero). The results of this calculation 59 show that it reduces the zero-field parallel susceptibility with the reduction being of order  $\chi_{\mid \mid}$   $A_n^2/T^2$ . The magnitude of this contribution at 15 mK, the approximate limit of the validity of our theoretical results, is about .5% and at 10 mK is about .8%. The contribution to the perpendicular susceptibility assuming B=0 has also been estimated. It is found that this

The values in Principle values of the interaction tensors relevant parenthesis were obtained during our investigations to CuTPP along the crystalline axes $^{55}$ . of CuTPP. Table 7.

Nuclear Quadrapole coefficient (x10 <sup>-4</sup> cm <sup>-1</sup> )	ø	64.0	l	
Superhyperfine coefficients (x 10 <sup>-4</sup> cm <sup>-1</sup> )	8	<u>.</u> 9	I	
	An	9. 9.	1	
Hyperfine coefficients (x 10 <sup>-4</sup> cm <sup>-1</sup> )	<b>1</b>	30	(0%~)	
	<b>∀</b>	212.2	(205.I ± 14.2)	
Electronic g-values	5√	2.033	(2.052 ± .017)	
	 	2.179	2.175 ±.017)	

susceptibility will be reduced by approximately .7% at 20 mK and 2.0% at 10 mK.

It should be mentioned that if this term were large, one would not expect the crystal field approximation, and therefore this spin hamiltonian, to be valid for this system. This would be true because a basic assumption of the crystal field theory is that the ion under consideration is entirely separate from the source of the crystalline electric field, and can be treated as a free ion in the crystalline electric potential.

The only term which has not been discussed is \$\sigma\_i'H\_{ij}\$. In general this term expresses the intermolecular coupling of the copper ions. It is composed of both the classical dipole-dipole coupling and exchange coupling. Even the large nearest neighbor distance (8.4Å) in crystalline CuTPP does not prevent the effects of the dipolar coupling from becoming significant at low temperatures. However, it does mean that the effects of exchange coupling between copper atoms, which approximately drops off exponentially, will probably be very small in this material barring any unusual super-exchange effects. Such effects could possibly occur if two copper electrons could interact through the phenyl rings. However, there is no experimental evidence that such an interaction occurs in CuTPP. Assuming the molecules only interact by classical dipole-dipole coupling we can write

the interaction at the ith ion due to all the other copper ions as:

$$H_{d_{i}} = \sum_{j} \frac{(\underline{u}_{i} \cdot \underline{u}_{j}) - 3(\underline{u}_{i} \cdot \hat{r}_{ij})(\underline{u}_{j} \cdot \hat{r}_{ij})}{r_{ij}}$$

where j is summed over the crystal lattice and  $\mu_i$  is a vector whose components are  $\mathbf{g}_k$   $\mathbf{S}_{k_i}$  ( $\mathbf{k}=\mathbf{x},\mathbf{y}$ , and  $\mathbf{z}$ ). The manner in which this summation is carried out in actual calculations is presented in Appendix C.

The presence of the dipolar coupling term disallows a solution of the magnetic susceptibility for this system in closed form. Since the Zeeman and hyperfine terms are by far the larger of the interactions we treat dipole-dipole interactions as a perturbation in order to estimate its effects. The hamiltonian that we must work with in the absence of such perturbations is:

$$H_{o} = g_{||\mu} S_{z}^{H}_{z} + g_{|\mu} (S_{x}^{H}_{x} + S_{y}^{H}_{y}) + AS_{z}^{I}_{z} + B(S_{x}^{I}_{x} + S_{y}^{I}_{y})$$

The zero field magnetic susceptibility can be easily calculated by working in the basis in which the hyperfine interaction is diagonal. The result of this calculation for the susceptibility parallel to the c axis is:

$$(\chi_0)_{\parallel} = \frac{g_{\parallel}^2 \mu^2}{4kT} \frac{\left[e^{-\beta A} + \frac{A^2}{2\alpha^2} \left\{\frac{3B^2}{A^2} \frac{\sinh \beta \alpha}{\beta \alpha} + \cosh \beta \alpha\right\} + \frac{\sinh B}{\beta B}\right]}{\left[e^{-\beta A} + 2 \cosh \beta \alpha + \cosh \beta B\right]}$$

This susceptibility exhibits a Curie law behavior in both the high and low temperature limit, with the effective Curie constant decreasing by about 7% from  $\frac{g_{\parallel}^2 \mid^{\mu^2}}{4k}$  in the high temperature limit to  $\frac{g_{\parallel}^2 \mid^{\mu^2}}{4k}$  ( $\frac{1}{1+3B^2/A^2}$ ) in the low temperature limit.

The zero field susceptibility perpendicular to the c axis was determined to be:

$$\chi_{O_{\perp}} = \frac{g_{\perp}^{2} \mu^{2}}{4\alpha (B^{2} - \alpha^{2}) (e^{-\beta A} + 2 \cosh \beta \alpha + \cosh \beta B)} \left[\frac{A\alpha}{3} (e^{-\beta A} + 2 \cosh \beta \alpha)\right]$$

$$- \frac{(A^2 + 4\alpha^2)}{3} \sinh \beta \alpha - A\alpha \cosh \beta B + 2B\alpha \sinh \beta B$$

which has a Curie law behavior in the high temperature region, but becomes essentially temperature independent at about 10 mK. The details of the manner in which these calculations were carried out is presented in Appendix C.

The modification of these results due to the effects of the classical dipole-dipole interaction in a crystalline solid can be estimated by utilizing Van Vleck's moment expansion technique<sup>60</sup>. This method involves treating the dipole-dipole coupling as a perturbation on the Zeeman and hyperfine interactions, and expanding the partition function in powers of 1/T. In this manner the effect of dipolar coupling can be determined for temperatures such that the

coupling energy is small compared with kT. Van Vleck's result showed that if a system had a Curie law behavior  $(\chi = c/T)$  at high temperatures then the effect of a dipolar term would be to modify the magnetic susceptibility according to

$$\chi = c/T \left(1 + \frac{c\Delta}{T} + \ldots\right)$$

where  $\Delta$  is an appropriate summation of the dipole interactions over the crystal lattice  $^{61}$ . If this expansion is carried to first order, the result looks like a low temperature expansion of the Curie-Weiss law  $(\chi = \frac{C}{T-\theta})$  to first order. In practice the dipole lattice summation is often used to define an effective Curie-Weiss theta  $(\theta = c\Delta)$ . The results of applying this expansion technique to evaluate the dipolar contribution to the parallel and perpendicular magnetic susceptibilities of CuTPP to first order are:

$$\chi_{\mid \mid} = (\chi_{o})_{\mid \mid} \{1 + (\chi_{o})_{\mid \mid} \Delta_{\mid \mid} + \ldots \}$$

$$\chi_{\perp} = (\chi_{0})_{\perp} \{1 + (\chi_{0})_{\perp} \Delta_{\perp} + \ldots \}$$

where 
$$\Delta_{\mid \mid} = \sum_{j}' \left( \frac{z_{ij}^2 - r_{ij}^2}{r_{ij}^5} \right)$$
 and  $\Delta_{\perp} = \sum_{j}' \left( \frac{x_{ij}^2 - r_{ij}^2}{r_{ij}^5} \right)$  are the

appropriate lattice summations for a crystal of CuTPP. In these summations  $r_{ij}$  is the distance between the ith and

jth atoms and has components  $x_{ij}$ ,  $y_{ij}$  and  $z_{ij}$ . These summations define effective Curie-Weiss thetas of -1.54 mK and +0.62 mK respectively. The method by which this lattice summation and the susceptibility calculations was carried out is presented in Appendix C.

#### CHAPTER III

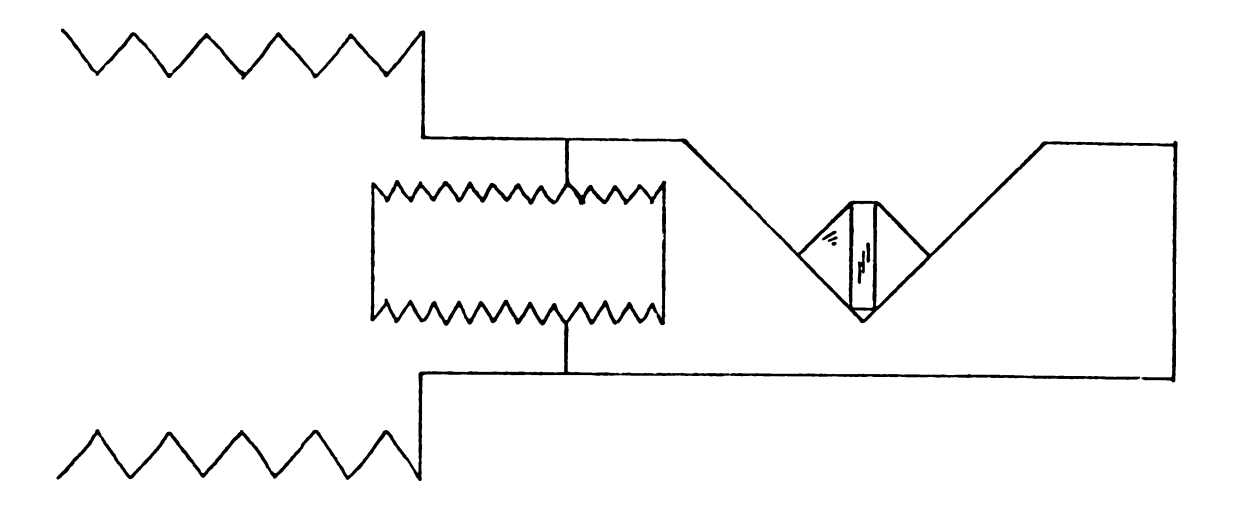
#### THE EXPERIMENTAL DATA

### A. Presentation of the Experimental Results for CuTPP

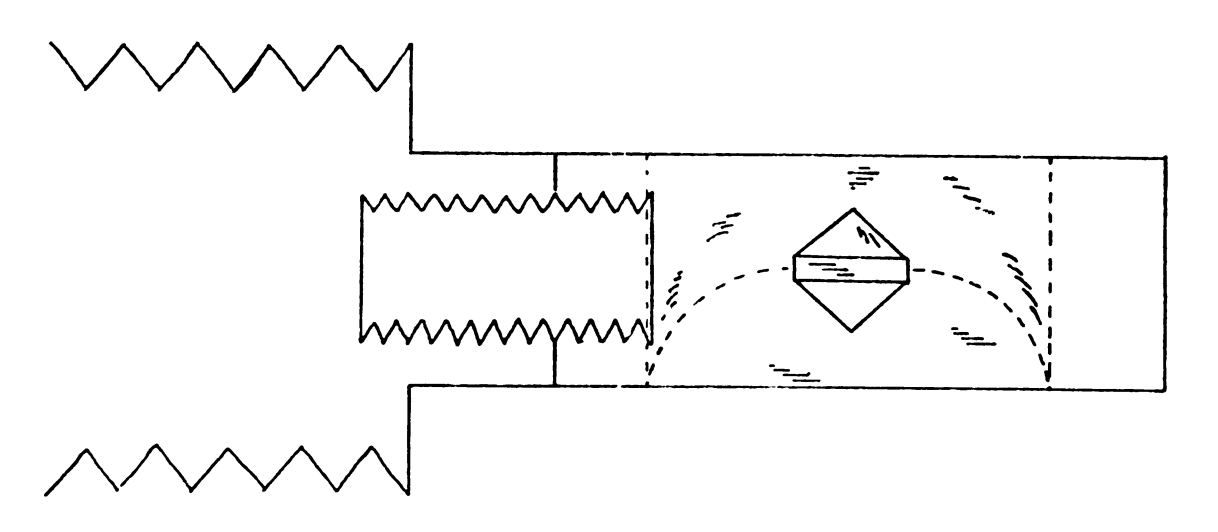
Once the direction along which magnetic susceptibility measurements are to be made is decided and related to the external morphology of the crystal, it must be properly mounted within the SQUID. The crystal shape and relative orientation of the porphyrin rings with respect to the crystalline axes determine the difficulty encountered with the alignment of the crystal. There is also the additional problem of the crystals' small size. Due to the symmetry of the CuTPP crystals and the fact that the porphyrin rings are perpendicular to the c axis, this task was not too difficult for this compound.

Drawings of the SQUID sample holders and mounted crystals for measurements of magnetic susceptibility parallel and perpendicular to the planes of the porphyrin rings are shown in Figure 29. The sample holders were designed to make the alignment process as simple as possible. Crystal alignment within the holders was accomplished by adjusting the crystal relative to the sample holder axis with a small probe while observing the results through a microscope. The accuracy of the alignment was then checked by placing the sample and holder in an optical goniometer

Figure 29. The manner in which the single crystals were mounted in the SQUID magnetometer for measurements of the parallel and perpendicular susceptibilities.



Parallel Axis →



Perpendicular Axis -->

and determining the position of the crystal with respect to the axis of the sample holder. It was found to be relatively easy to attain an accuracy of ±4°. Calculations of the maximum effect of a misalignment of this magnitude results in an uncertainty in the magnetic susceptibility of about .2% at 10 mK. The crystal was secured to the holder by applying a small drop of glycerine and soap flakes glue.

Before magnetic susceptibility measurements were made on the CuTPP crystals, they were checked by ESR techniques to determine for certain that the c axis was indeed obvious from the external crystal morphology. The hyperfine splitting was found to be maximum along the direction we had chosen as the four-fold axis, thereby indicating this direction was perpendicular to the plane of the porphyrin rings and was the c axis of the crystal. These ESR measurements yielded electronic g-values of  $g_{||}$  = 2.175 ± .017 and  $g_{\parallel}$  = 2.052 ± .017. The uncertainty in these numbers does not include the effects of crystal misalignment within the ESR apparatus, which could not be determined. hyperfine constants were also determined to be  $A = (205.1 \pm 1.00)$ 14.2)  $\times 10^{-4}$  cm<sup>-1</sup> and B ~ 30  $\times 10^{-4}$  cm<sup>-1</sup>. Since the hyperfine splitting parallel to the porphyrin planes could not be resolved in the magnetically concentrated crystal, the hyperfine coefficient in this plane, B, was found by extrapolation of the out-of-plane data. These numbers are

comparable with the values obtained by P. T. Manoharan and Max T. Rogers<sup>55</sup>. They measured  $g_{\parallel} = 2.179$  and  $g_{\perp} = 2.033$  for the electronic g-values and A = 212.2 x  $10^{-4}$  cm<sup>-1</sup> and B = 30 x  $10^{-4}$  cm<sup>-1</sup> for the hyperfine constants. Having confidence in our crystals we then aligned then in the dilution refrigerator.

Two crystals were used for parallel susceptibility measurements, one having a mass of approximately .6 mg and the other having a mass of 1.25 mg. The .6 mg crystal was originally a larger crystal which had fractured so that it no longer had the tetragonal bipyramid shape, but instead was very roughly pyramidal. The 1.25 mg crystal had the normal tetragonal bipyramid shape and was also used for susceptibility measurements perpendicular to the c axis. This crystal was estimated to be about 1mm 3 in volume and to have a surface area of 5.2  $\times$  10<sup>-2</sup> cm<sup>2</sup>. Both the parallel and perpendicular susceptibilities were measured with a .25 gauss dc magnetic field trapped in the niobium cylinder. The systematic errors in the zero-field magnetic susceptibility due to the presence of this small finite field is negligible even at the lowest temperatures attained during the experiment.

A sample of powdered CuTPP was placed in the conventional magnetic susceptibility coils of the refrigerator.

The sample was formed by pressing .25009 gm of CuTPP into a .793 cm right circular cylinder with diameter equal to

height. The resulting filling factor for this sample was 44.5%. The CuTPP was not actually powdered by us but was used exactly as it had been formed by the preparation process. The grain size obtained during a rapid precipitation of the CuTPP is very important if the precipitate is to be used directly at ultralow temperatures. If the individual grains are small enough and internal relaxation processes are not too long, powdered samples are the only means of properly thermally tying a material to the cold dilute solution at extremely low temperatures. A comparison of single crystal and powder data then becomes useful as an indication of where the single crystals might be going out of thermal equilibrium with the refrigerator and therefore of the range of validity for these single crystal measurements. The average grain size for CuTPP was estimated using a high power, oil drop microscope to be on the order of 1 micron.

During these experiments we found no indication of a thermal equilibrium problem with regard to the powdered CuTPP sample. The powder susceptibility measurements were made in a 1.6 gauss ac magnetic field in the temperature range from 4.2°K to .3°K, where careful calibration of the 90% LMN - 10% CMN thermometer is necessary, and in a .4 gauss field at lower temperatures.

The experimental zero field magnetic susceptibility data obtained for CuTPP is shown graphically in Figure 30, which

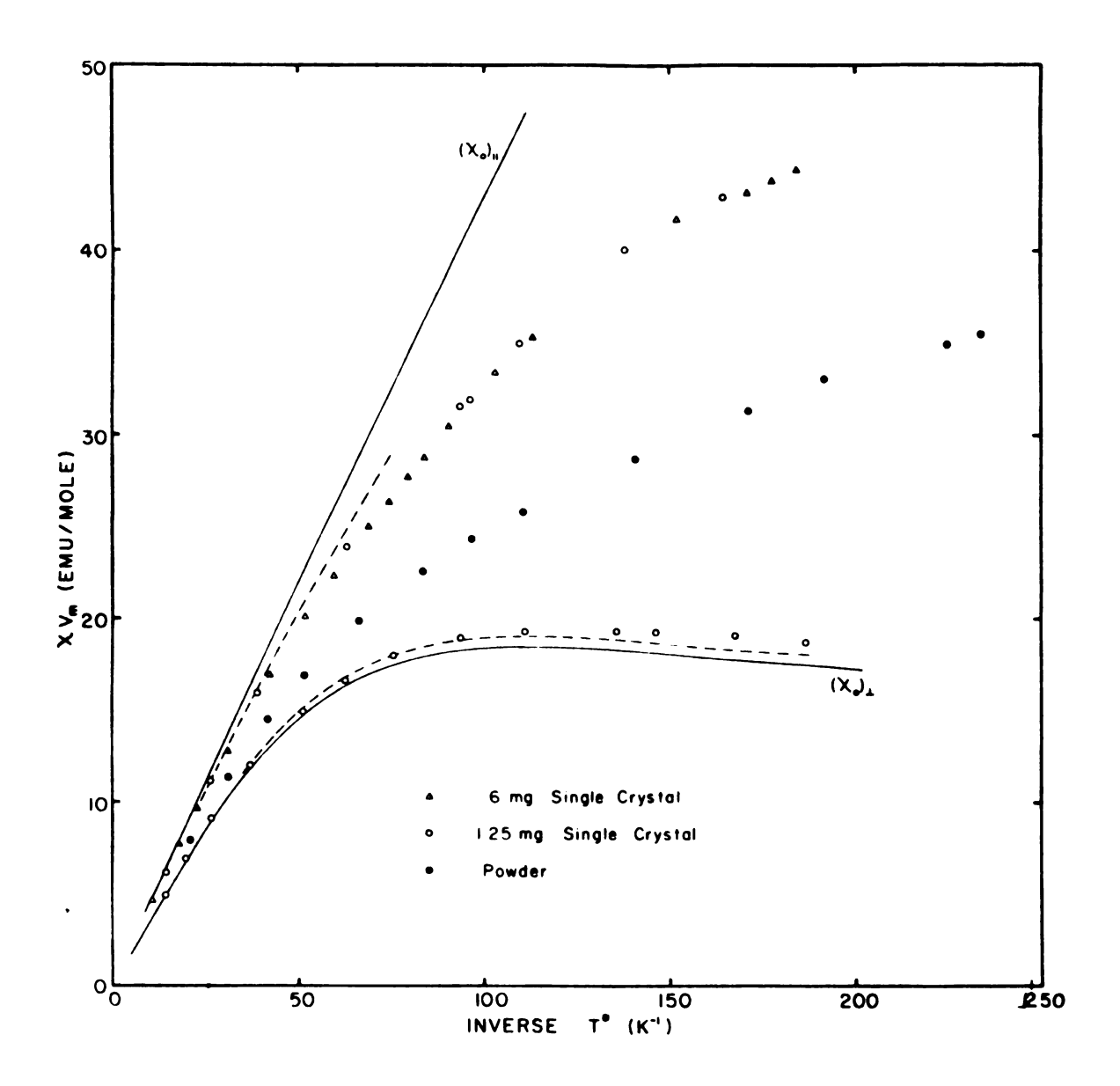


Figure 30. The magnetic susceptibility data for CuTPP.

The solid lines represent the theoretical susceptibilities without inclusion of the dipolar interaction and the dashed lines represent the theoretical susceptibilities including the effect of dipole coupling.

is a plot of susceptibility in emu/mole against the inverse magnetic temperature. The data are also presented in tabulated form in Appendix D.

The magnetic susceptibility perpendicular to the c axis (i.e. in the plane of the porphyrin rings) became approximately temperature independent at about 10 mK after attaining a maximum susceptibility of 19.3 emu/mole. In the temperature range from .7°K to .25°K, where deviations from Curie-law behavior are not yet apparent, this data yields  $g_{\parallel}$  = 1.963  $\pm$ .008. The most likely reason for this g-value being different from the ESR results is that the .25 gauss magnetic field was not trapped properly in the SQUID magnetometer. An error in the trapped field of only .02 gauss could easily account for this discrepancy. This effect is possible because the µ-metal shield, which must be moved after each experiment, may be positioned slightly differently from one experiment to another. However, this presents no serious difficulty with the data since the g-factor can be renormalized if necessary.

The susceptibility parallel to the c axis (i.e. perpendicular to the porphyrin planes) was found to continue rising, at least initially, in a Curie-like manner down to the lowest temperatures. The value obtained for  $g_{\parallel}$  by using the high temperature data measured on the 1.25 gm crystal was 2.177  $\pm$  .012. This compares favorably with the previously mentioned values obtained by ESR methods. Since

the .6 mg crystal could not be massed properly, the parallel susceptibility data acquired from this crystal was normalized such that it agreed with the other crystal data at high temperatures. The two sets of data deviated slightly from each other at the lowest temperature; however, one might expect this as demagnetization corrections for each sample (see page 133) are different.

The powder susceptibility continues rising down to at least 4.2 mK with no indication of the onset of a transition to the ordered state being apparent. We believe the powder data to be very reliable even at temperatures below 10 mK, when the refrigerator is operating in the "single shot" mode, due to the expected good thermal contact between the powder grains and dilute solution. This seems to be verified by the fact that during the experiment the relaxation time of the CuTPP powder sample was observed to be at least as rapid as the relaxation time associated with the LMN-CMN thermometer.

# B. Factors Affecting the Measurement of Magnetic Susceptibility at Ultralow Temperatures

## Demagnetization Corrections

An important consideration that must be taken into account when studying single crystals at very low temperatures is the presence of demagnetizing fields within the crystals 62. The magnetic susceptibility one measures experimentally is determined with respect to the external magnetic field (H<sub>o</sub>) that is applied to the sample as a whole  $(\chi_{ext} = M/H_0)$ . However, a paramagnetic ion within the crystal does not respond to the influence of the external field, but instead to some resultant field interior to the crystal which depends on the crystal shape (i.e. boundary conditions at the crystal surface) and the relative positions of the paramagnetic ions (i.e. the crystal lattice structure). Therefore the experimentally measured magnetic susceptibility must be corrected so that it reflects the influence of the local field (H<sub>loc</sub>) at the paramagnetic ion. These corrections can be estimated in the following manner.

Consider an ion at the center of the crystal. The magnetic field at the site occupied by this ion is less than the applied external field due to the effect of induced "magnetic poles" at the crystal surface. This opposing field is proportional to the intensity of magnetization so

that one can express the internal magnetic field in the crystal as:

$$H_i = H_O - NM$$

where N is the demagnetization factor. Now we must consider the effect of all the other paramagnetic ions on this This can be determined by dividing the influence of these ions into several contributions. First we imagine removing all the ions in a spherical region, which is microscopically large but macroscopically small centered about this site. The contributions to the local field are now due to the ions outside the sphere, on the surface of the spherical region, and interior to the spherical volume. The ions outside the sphere are assumed far enough from the site at which we are determining the local field so that they can be considered as a continuum of magnetic dipoles. An integration over this volume shows it produces no net field at the center of the sphere. The surface of the sphere on the other hand contributes a field of  $\frac{4\pi}{3}$  M at its The effect of ions interior to the sphere is interior. determined by adding the contributions from each ion. is related to the classical dipolar lattice summation of page 122. The local field at the ion can now be expressed as: 60

$$H_{10C} = H_0 + (4\pi/3 - N + \Delta')M$$

where MA' is the field determined from the lattice summation. Since the effective field derived from this lattice summation has been accounted for previously by the expansion of dipole-dipole interaction term of the spin hamiltonian, we do not need to consider this term here. The actual susceptibility can now be calculated:

$$\chi_{\text{loc}} = \frac{\chi_{\text{ext}}}{1 + (4\pi/3 - N)\chi_{\text{ext}}}$$

where we define  $\chi_{loc} = M/H_{loc}$ .

Our problem now is to determine the demagnetizing factor for the particular crystals we study. Demagnetizing factors can only be calculated for samples which are ellipsoids of revolution or limiting cases of this shape (i.e. a flat disk or long needle). The complications arising from such a complex surface as that exhibited by CuTPP crystals make a calculation of N essentially impossible. In order to evaluate the effect of this correction an alternate method must be found other than a direct calculation. Since N is only a function of the shape of the sample we can estimate it by a room temperature experiment as follows. A mockup (scaled to 1 mm = 1 inch) of the CuTPP crystals was made from mild steel. The magnetic induction internal to the steel "crystal" upon the application of an external magnetic field is:

$$B_{i} = H_{i} + 4\pi M$$

$$= (1 + 4\pi \chi_{i}) H_{i}$$

where the internal field  $H_i$  is related to the external applied field  $H_O$  through the demagnetizing coefficient  $(H_i = H_O - NM)$ . We can also write the magnetic induction in terms of the external field:

$$B_i = H_O + (4\pi - N)M$$
  
=  $(1 + (4\pi - N)\chi_{ext})H_O$ 

Now for steel the internal permeability ( $\mu_i = 1 + 4\pi\chi_i$ ) is much greater than 1 so combining the two expressions for the internal magnetic induction and applying the condition  $1/\mu_i \stackrel{\sim}{\sim} 0$  will yield the result:

$$N \approx \frac{1}{\chi_{oxt}} = \frac{H_o}{M}$$

Therefore the shape dependent factor N can be determined for a steel mockup of the crystal and this demagnetization factor applied to the CuTPP crystal data. Of course there are some approximations inherent in this calculation. For the mild steel we used the permeability was determined to be approximately 250 so that the approximation  $1/\mu_1 = 0$  is good to about .5%. It is also assumed that the steel is an isotropic medium.

The demagnetizing factor was determined experimentally by the following method. The steel mockup of the CuTPP samples and a similar size steel sphere were alternately inserted into a pickup coil in the presence of an applied magnetic field. Their magnetization was determined by the flux changes they induced in the pickup coil as they were placed into and removed from it according to the following relation:

$$M = \frac{\Delta \phi}{4\pi V n f}$$

where  $\Delta \phi$  is the flux change, V is the volume of the sample, n is the number of turns per unit length in the pickup coil and f is a factor which depends on the coil geometry:

$$f = \frac{L/2}{(R^2 + (L/2)^2)^{\frac{1}{2}}}$$

where L is the length of the coil and R is its radius.

Two pickup coils were used during the measurements. One coil was a mockup of a section of the SQUID sample coil to the same scale as the crystals. The other was a much larger coil (R = 19.9 cm) in which the diameter of the sample was much smaller than the coil diameter. This condition is assumed to hold for the above equation which relates magnetization to the flux change produced by a sample of volume V. For a spherical sample, if these conditions are valid, one would expect N =  $4\pi/3$ . Therefore a measurement of the demagnetizing factor for the steel

sphere provides a means of calibrating the pickup coils. In order that our susceptibility correction equation be valid for the susceptibility of CuTPP as measured in emu/mole we may define the following relationship:

$$\varepsilon = (4\pi/3 - N)\rho/m$$

where m/ $\rho$  is the molar volume of CuTPP ( $\rho$  = 1.43 gm/cm<sup>3</sup>; m = 676.8 cm<sup>3</sup>/mole). The susceptibility of CuTPP corrected for crystal shape effects is then:

$$\chi_{\text{loc}} = \frac{\chi_{\text{exp}}}{1 + \varepsilon \chi_{\text{exp}}}$$
 (emu/mole)

For the large pickup coil it was found that for the sphere  $\varepsilon_{\rm S}=-.0003$  while for the small coil, for which the assumed conditions are not valid, but more closely approximate the experimental arrangement for measurements on CuTPP, we found  $\varepsilon_{\rm S}=-.0013$ . These values could now be used to correct all other measurements to satisfy the condition  $\varepsilon_{\rm S}=0$ . The corrected values of  $\varepsilon$  measured for the parallel axis direction of the 1.25 mg crystal was  $\varepsilon_{\parallel}=-.0013$  ± .0003 for both coil measurements and the perpendicular axis measurements gave  $\varepsilon_{\perp}=+.0027$  for the large coil and + .0023 for the small coil, for an average value of  $\varepsilon_{\perp}=+.0025$  ± .0005. All measurements were first with the external field in one direction, then again with the field reversed. This was necessary to ensure there would be no problems due

to residual fields in the steel samples. The differences in these measurements were not significant.

The magnetic susceptibility of CuTPP corrected for crystal demagnetization effects can now be expressed as:

$$\chi_{\parallel} = \frac{\chi_{\parallel}^{\exp}}{1 - .0013 \chi_{\parallel}^{\exp}}$$

and

$$\chi_{\perp} = \frac{\chi_{\perp}^{\text{exp}}}{1 + .0024 \chi_{\perp}^{\text{exp}}}$$

where the susceptibilities are in emu/mole.

The correction was also estimated for the fractured .6 mg CuTPP crystal by machining a steel mockup crystal which approximated the shape of this CuTPP crystal as closely as possible. For this shape  $\varepsilon_{||}$  was found to be  $-.0022 \pm .0003$ . The uncertainty in this result is small because it does not reflect the difficulty of correctly reproducing the irregular shape of the fractured CuTPP crystal. However, upon application of this correction to the experimental data one finds that the .6 mg data even more closely follows the 1.25 mg data to low temperatures. This is evidence that the deviations of the original data obtained from each crystal differed because of the effects of demagnetization of the different crystal

shapes. A plot of the magnetic susceptibility of CuTPP corrected for demagnetization effects is shown in Figure 31 page 144, and is tabulated in Appendix D. Also shown on this graph is the theoretically calculated susceptibility including the contribution from the dipolar coupling term. The powder susceptibility measurements have not been corrected for demagnetization effects. These corrections are very difficult to estimate for powder samples. Attempts have been made to measure demagnetization effects in powdered right circular cylinders of CMN with diameter equal to height 37-39. These measurements were mentioned with respect to thermometry. One might expect the corrections for a similar shaped CuTPP powder sample to be even smaller because of the more isotropic nature of a CuTPP powder grain as compared to CMN. It will definitely be a much smaller correction than is necessary for the single crystal measurements.

# Thermal Equilibrium of Single Crystals

Another serious problem which arises when one attempts to study single crystals at ultralow temperatures is the difficulty of maintaining thermal equilibrium with the dilute solution. The very small crystals employed in the single crystal SQUID measurements allow thermal equilibrium to be maintained to much lower temperatures than is possible for the large crystals which would be required in

the conventional magnetometers. However, due to the rapid increase in Kapitza resistance for heat flow across the crystal surface to the dilute solution, even these crystals eventually reach a temperature below which thermal equilibrium is no longer possible.

One can estimate the relaxation time necessary for thermal equilibrium to be achieved between the crystal and dilute solution. Assuming the Kapitza resistance to be on the order of  $10^{-5}/\mathrm{AT}^3$ , approximately valid for many dilute solution-solid interfaces, the relaxation time will be:

$$t = R_k C = \frac{10^{-5} C}{AT^3}$$

where C is the heat capacity of the crystal. The heat capacity of the 1.25 mg crystal was estimated assuming the entire contribution is due to the hyperfine coupling (i.e. ignoring the dipolar interaction). In the temperature range around 10 mK it was found to be about 5 x  $10^7$  ergs/mole-K. An estimation of the 1.25 mg crystal's surface area based on the crystal's dimensions as measured by a travelling microscope indicates that A  $\sim 5.2 \times 10^{-2} \text{ cm}^2$ . Thus at 14 mK one would expect a relaxation time for this crystal on the order of two hours, but at 10 mK it would increase to 6 hours. This is consistent with our experimental results. At 14 mK the crystal's thermal relaxation time is on the order of the relaxation time of the refrigerator (see Figure 7 and Appendix A), but at 10 mK it has become much larger. Our

experimental data indicates the powder data do begin to deviate from the effective powder susceptibility as determined by the single crystal data  $(\chi_{pow} = \frac{\chi_{||}}{\chi_{pow}} + \frac{\chi_{||}}{\chi_{pow}})$  at about 14 mK (Figure 31). The data obtained with the .6 mg crystal, which has a smaller heat capacity than the 1.25 mg crystal, indicates thermal equilibrium with this sample was maintained to approximately 11 mK. This is verified by observations of a chart recorder which continuously monitors the SQUID sample response and LMN-CMN thermometer response to changes in temperature. No indication of unusually long relaxation times were noticed at temperatures above 14 mK. It should be mentioned that measurements on other crystals 63 have shown it is possible to carry some single crystal measurements to below 10 mK. The value of the SQUID magnetometer as a tool for studying crystals at ultralow temperatures is very apparent from these results.

#### CHAPTER IV

#### AN ANALYSIS OF THE EXPERIMENTAL RESULTS

## A. Comparison of Theory and Experiment

The experimental magnetic susceptibility data corrected for demagnetization effects is presented in Figure 31 which is a plot of  $\chi$  in emu/mole vs. the inverse magnetic temperature (1/T\*). The uncertainty in the parallel and perpendicular susceptibility data is represented by error bars. Some of this uncertainty arises from the possibility of crystal misalignment within the SQUID sample holder (±4°). Other sources of error from which these error bars are derived include uncertainties in the measurements which are necessary for the determination of the demagnetizing factors, and in the approximation  $1/\mu_i = 0$ . A probable major contribution to the uncertainty in this data, not included in the error bars, concerns the reliability of these demagnetization corrections in their application to the CuTPP crystal. It was assumed that measurements on a nearly isotropic medium, steel, can be directly applied to an anisotropic medium such as CuTPP. Error bars on the parallel susceptibility data below 14 mK on the 1.25 mg crystal data and below 11 mK for the .6 mg crystal data are no longer useful indicators of the accuracy of this data due to the onset of systematic errors arising from the lack of thermal equilibrium at these temperatures.

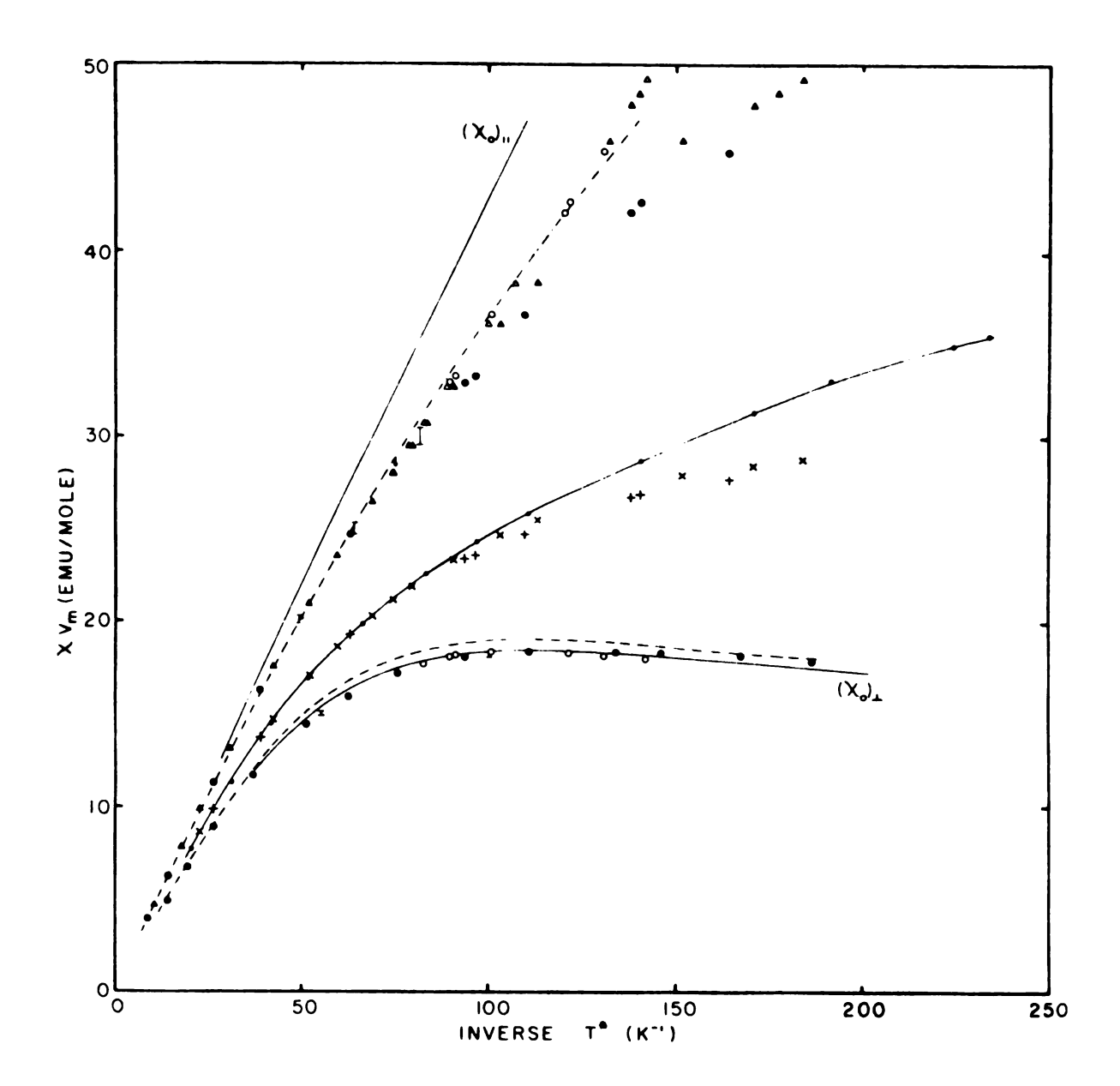


Figure 31. The magnetic susceptibility data for CuTPP corrected for demagnetization effects. Open symbols represent data further corrected for thermal equilibrium effects. The +'s and x's represent an "effective powder susceptibility" derived from the single crystal data.

The susceptibility perpendicular to the crystalline c axis becomes approximately temperature independent at The uncertainty in this data due to the previously mentioned sources is .3% at about 20 mK and increases to .6% at 10 mK. The basic behavior of this susceptibility can be understood from the hyperfine interaction between the copper electronic and nuclear spin. The theoretical perpendicular susceptibility including the contribution from the dipolar-interaction lattice summation has been plotted in Figure 31 for comparison with the experimental The theory rises above this data below about 30 mK, following the data but remaining above it to the lowest temperature. Estimations of the effect of the nuclear quadrupole interaction in the approximation B = 0indicate it will increase the  $\chi_{\,|\,}$  theory by approximately .4% at 20 mK and as much as 1.5% at 10 mK. The contribution from the superhyperfine interaction in the same approximation will reduce this theory by about .7% at 20 mK and 2% at 10 mK. Remembering that the estimation of the quadrupole interaction effect was carried out assuming the maximum value possible for Q, one can say that at the least the overall effect of these terms will be to decrease the  $\chi_{\parallel}$  theory by about .3% at 20 mK and .5% at 10 mK.

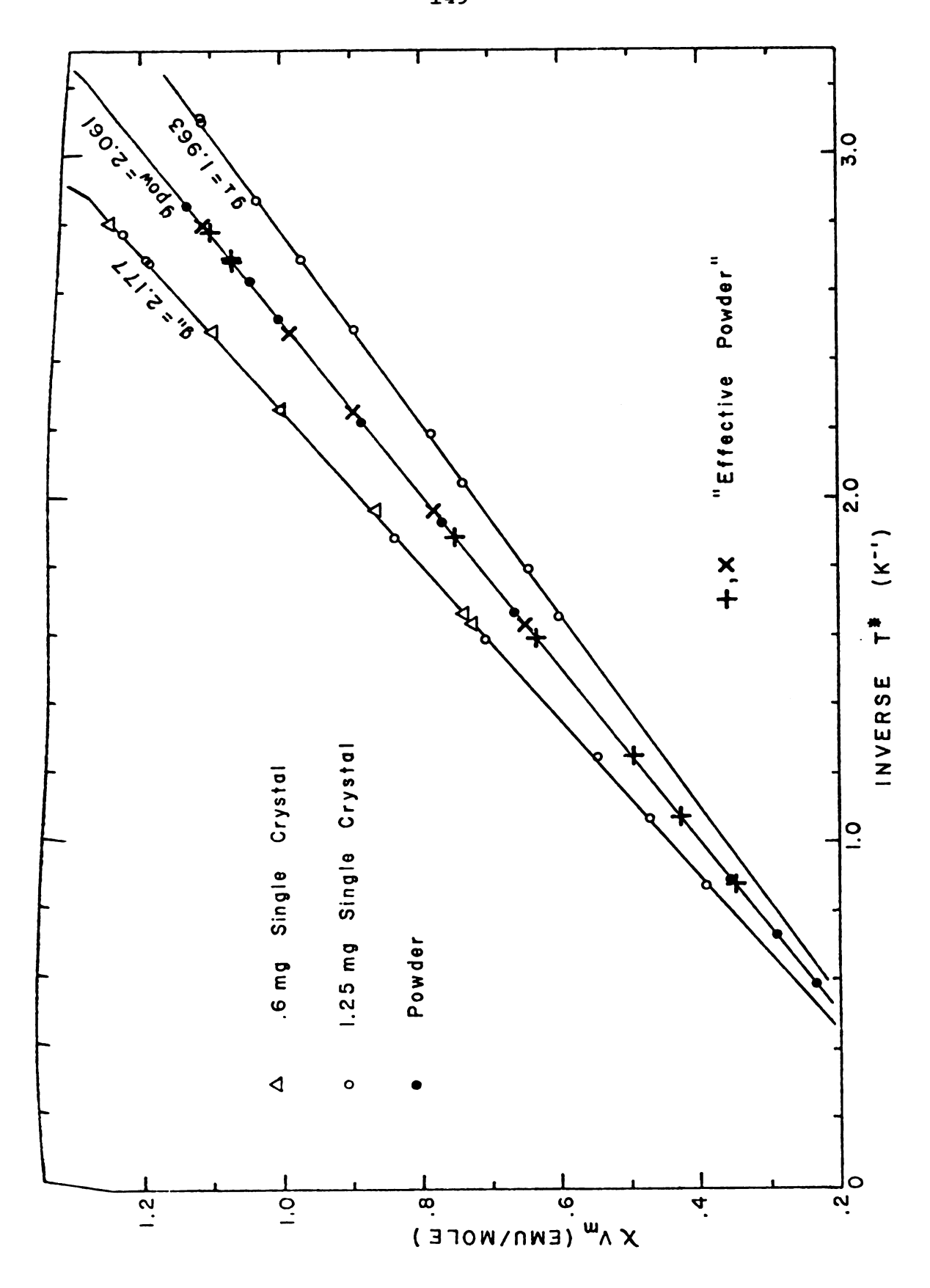
The susceptibility parallel to the crystalline c axis continues to increase in a Curie-like manner to the lowest temperatures we were able to attain. Estimations of the

expected uncertainty in this data indicate they are uncertain to within 1% at 20 mK, increasing to approximately 1.5% at 12 mK. The theoretical parallel axis magnetic susceptibility is probably valid to approximately Below these temperatures it is possible that contributions from higher order terms in 1/T will become important and should be considered before this theory can be extended to lower temperatures. Calculations of the effects of the superhyperfine and nuclear quadrupole interactions indicate that this theoretical  $\chi_{\parallel \parallel}$  should be reduced by about .4% at 20 mK and as much as .6% at about 14 mK in the approximation B = 0. The entire contribution is a result of the superhyperfine coupling, the quadrupole interaction giving zero contribution in this approximation. The possible correction of this theory due to the presence of the superhyperfine interaction is indicated by arrows in Figure 31. Of course in the actual case, where  $B \neq 0$ , one would expect this effect to be somewhat modified from our calculation. However, we do not believe this modification would be large. The manner in which B affects  $\chi_{\left.\right|\right.}$  was shown in Figure 30. The effective Curie constant was changed by -7% from the high to the low temperature regimes. The superhyperfine coupling is an even higher order effect at these temperatures. The maximum deviation of the theory and experimental data for the parallel susceptibility, not including the estimated effect of the superhyperfine

coupling, is about 1.3% down to 16 mK, the theory lying slightly below the experimental data. This maximum deviation occurs at about 30 mK.

The importance of the temperature independent behavior of the perpendicular susceptibility at low temperatures in estimating the behavior of the parallel susceptibility to even lower temperatures will now be made apparent. As has been mentioned previously, the powder sample is expected to be in good thermal equilibrium down to 4 mK. If we form an appropriate summation of the parallel and perpendicular axis crystal susceptibility ( $\chi_{pow} = \chi_{||}/3 + 2 \chi_{||}/3$ ), we can compare the experimental powder data with an "effective powder susceptibility" as determined by the single crystals. For this comparison it was necessary to normalize the  $\chi_{\parallel}$ data so that the experimental and effective powder data were equal over the temperature range of 3 K to .3 K. This is tantamount to requiring the condition  $g_{pow}^2 = g_{\parallel}^2/3 + 2g_{\parallel}^2/3$ to hold at high temperatures. The perpendicular g value was adjusted to 2.001. Figure 32 shows the susceptibility data over this temperature range. The results of this summation is shown in both Figure 31 and Figure 32 where +'s indicate the 1.25 mg parallel axis crystal data were used and x's indicate the .6 mg parallel axis crystal data were used. In both instances the perpendicular axis data were obtained from the 1.25 mg crystal. The effective powder data begins to deviate from the measured powder susceptibility at about

Figure 32. The high temperature single crystal and powder magnetic susceptibility data. The g values determined from this data are also shown. The "effective powder susceptibility" was obtained from the crystal data after normalizing the perpendicular susceptibility to g = 2.001.



13-14 mK for the 1.25 mg crystal and at about 11 mK for the .6 mg crystal. This indicates the .6 mg crystal was probably in better thermal equilibrium than the 1.25 mg crystal which is, of course, reasonable since the .6 mg crystal has the smaller heat capacity and a larger surface-to-volume ratio. Below these temperatures it is apparent that thermal equilibrium can no longer be maintained between the respective crystals and the surrounding liquid helium.

Now at the temperatures at which the lack of thermal equilibrium becomes noticeable, the perpendicular susceptibility has become approximately temperature independent. Therefore, one would expect the experimentally determined perpendicular susceptibility to deviate very little from the actual value to even lower temperatures than is possible for measurements of  $\chi_{|\cdot|}$ . This allows us to manipulate the data in the following manner in order to estimate the parallel susceptibility to lower temperatures. can shift the effective powder data to higher temperatures (at a constant susceptibility value) until it coincides with the experimental powder susceptibility. Assuming the shift to be due solely to a lack of thermal equilibrium during the measurements (i.e. that the crystals were actually at the temperature defined by the shifted value), we can apply this temperature correction to  $\chi_{|\,|}$  and  $\chi_{|\,|}$ . Since the different crystals came out of thermal equilibrium at

different temperatures, these corrections will be different for each crystal. The effect of applying the thermal equilibrium corrections is shown in Figure 31. The open symbols on this graph represent thermally corrected data. Notice that now the .6 mg and 1.25 mg data coincide to temperatures on the order of 8.5 mK. Although it may not be valid in this temperature range, the theoretically determined parallel susceptibility has been extended into this region for comparison with the corrected experimental This extension of the theoretical  $\chi_{\parallel \parallel}$  continues to follow the data down to about 8.7 mK. The obvious next step in the analysis of these results is to attempt a calculation of the effect of the superhyperfine term when  $B \neq 0$ . However, such a calculation is extremely difficult and has not been carried out as yet. Also, it will most likely be very important to consider the 1/T dipolar interaction term.

Up to this point we have largely been concerned with uncertainties in the experimental data. However, there are also uncertainties associated with the coefficients used to determine the theoretical results. The theories therefore may be somewhat modified by the possible variations in these coefficients.

The theoretical perpendicular susceptibility was found to rise above the experimental data below 30 mK. Since this theoretical  $\chi_{\perp}$  is mainly controlled by the magnitude of the hyperfine coefficient A, one might ask how it would be

affected by a change in the value of A. Adjustments of A, within its uncertainty, were made and its effect on the  $\chi_{\parallel}$  theory was observed. In order to preserve the low temperature behavior of  $\boldsymbol{\chi}_{\parallel}$  as indicated by the experimental data, and also not change  $\chi_{\left| \ \right|}$  significantly, it is necessary to constrain the ratio B/A. If A is increased by 4% over the value used to obtain the theory plotted in Figure 31, then B must also be increased by 4%. This 4% increase is the limit allowed by the uncertainty in our EPR determination of A. Since P.T. Manoharan and M.T. Rogers<sup>55</sup> do not indicate the uncertainties in their measurements of A and B for magnetically concentrated single crystals, it is not known if these increased values would lie within the range of their uncertainties. The effect of such an increase is to reduce the  $\chi_{\parallel}$  theory so that it roughly follows the previous calculation of  $(\chi_0)_{\parallel}$ . However, it still would not fit the experimental data to within the error bars, but it is an improvement. One can therefore not say that an adjustment of these coefficients within the range of their uncertainties would be sufficient to explain the experimental data, but only that it is a possible factor in the  $\chi_{\parallel}$  theory not agreeing with the experimental data at the lowest temperatures.

It was estimated that the theoretical parallel susceptibility was on the average about 1.3% lower than several experimental  $\chi_{\parallel \parallel}$  data points in the temperature range around

If the experimental data is not corrected for demagnetization effects the theory and experiment would agree much better in this intermediate temperature region. (The same statement applies to  $\chi_{|}$ .) However, one finds that the effective powder susceptibility as determined by the crystal data in the absence of demagnetization corrections does not agree with the experimental powder data nearly as well over this temperature range as does the demagnetization corrected data. It therefore seems reasonable that the application of the demagnetization corrections is essentially correct. If the uncertainty in the experimental data is taken into account, the discrepancy between the experiment and theory is as small as .9%. One should also recognize that the maximum uncertainties in our temperature measurements (±1%) occur over the approximate temperature range 30-100 mK (see Figure 18). The temperature uncertainties will be reflected in the measurements of χ.

In light of the foregoing discussion of this data it seems that further analysis requires a calculation of the effect of the superhyperfine coupling and nuclear quadrupole interaction with  $B \neq 0$ . Only after this calculation is complete can one make more definite statements about the behavior of the parallel and perpendicular crystalline susceptibilities from the intermediate to the low temperature regions. We believe this data in general to be fit rather

well by the theoretical calculations. The basic behavior of the parallel susceptibility appears to be explained by the dipolar interaction, while the perpendicular susceptibility is primarily a result of the highly anisotropic hyperfine coupling.

# B. Summary and Conclusions

The magnetic susceptibility of CuTPP parallel to the crystalline c axis has been observed to follow the first order expansion of a Curie-Weiss law behavior down to a temperature of approximately 15 mK. The susceptibility perpendicular to the crystalline c axis became approximately temperature independent at about 10 mK. Theoretical calculations show this behavior for  $\chi_{\parallel}$  is primarily a result of the hyperfine interaction. An extension of the theoretical description of the parallel and perpendicular susceptibilities to lower temperatures will require a calculation of the superhyperfine interaction effect when  $B \neq 0$ , and a calculation of the  $1/T^3$  term in the expansion of the dipolar interaction. The powder data shows no signs of the onset of a transition to the ordered state to 4.0 mK. powder data is expected to be valid to this temperature because of the good thermal contact between the powder grains and the dilute solution. A comparison of the experimental powder data with an effective powder susceptibility determined from the single crystal data indicates the single

crystals were in thermal equilibrium to approximately 12 mK. The results of these single crystal experiments have proven the SQUID to be a very valuable tool for investigating the magnetic behavior of single crystal samples at ultralow temperatures.

This thesis has presented the initial results of a comprehensive study of metalloporphyrin and metallotetraphenylporphyrin compounds which is presently under way. The information obtained and techniques developed during the investigation of CuTPP is proving useful for the further study of these compounds. However, the study of CuTPP itself is undoubtedly not completed with the publishing of these results. The magnetic susceptibility along the crystalline c axis of CuTPP has been observed to continue rising at least down to 7 mK. It would certainly be very interesting to carry these measurements to even lower temperatures. A possible method by which this could be accomplished is the adiabatic demagnetization of a single crystal using the SQUID magnetometer. Such experiments as this may be forthcoming in the future. should be noted that adiabatic demagnetization of a powdered sample of CuTPP would not be useful as a means of producing lower temperatures, because the magnetic entropy vs. temperature relationship perpendicular to the c axis is such that adiabatic demagnetization would produce warming in all microcrystals for which the external magnetic field is oriented in this direction.

The relatively good thermal equilibrium observed between the single crystals and dilute solution at low temperatures indicates good internal heat transfer mechanisms within the crystals. Therefore it seems reasonable that this material could be of use in investigating the anomalously good thermal contact shown to exist between some salts and pure <sup>3</sup>He <sup>4</sup>. One may find that CuTPP single crystals could be studied at lower temperatures by utilizing <sup>3</sup>He to provide better thermal contact at ultralow temperatures.

It should be emphasized that the feasibility of a complete study of the metal complexed porphyrins at ultralow temperatures was critically dependent on the outcome of the single crystal measurements attempted on CuTPP. Since large single crystals of these compounds cannot be grown, they cannot be studied in conventional magnetometers. Even if this were possible, the lack of thermal equilibrium at relatively high temperatures would make an attempt at studying large crystals useless. The success of the single crystal studies of CuTPP using the SQUID magnetometer has shown it is possible to study very small single crystals at ultralow temperatures.



### LIST OF REFERENCES

- R. A. Fisher, E. W. Hornung, G. E. Brodale and
   W. F. Giauque, J. Chem. Phys. 58, 5584 (1973).
- 2. M. Kolac et al., J. Low Temp. Phys. 11, 297 (1973).
- 3. B. M. Abraham et al., J. Low Temp. Phys. <u>14</u>, 387 (1974).
- 4. J. H. Bishop et al., J. Low Temp. Phys. 10, 379 (1973).
- 5. H. Kojima, D. N. Paulson, and J. C. Wheatley, Phys. Rev. Letters 32, 141 (1974).
- J. C. Wheatley, Physica 69, 218 (1973).
- 7. E. Lagendijk et al., Physica 61, 220 (1972).
- 8. J. C. Doran, U. Erich and W. P. Wolf, Phys. Rev. Letters 28, 103 (1972).
- 9. R. A. Webb and J. C. Wheatley, Phys. Rev. Letters <u>29</u>, 1150 (1972).
- 10. L. D. Landau and I. Pomeranchuk, Dokl. Akad. Nauk. SSSR 59, 669 (1948).
- 11. H. London, <u>Proceedings of the International Conference</u>
  on Low Temp. Physics, Oxford (Clarendon Laboratory,
  1951) p. 157
- 12. G. K. Walters and W. M. Fairbank, Phys. Rev. <u>103</u>, 269 (1956).
- D. O. Edwards, D. F. Brewer, P. Seligman, M. Skertic,M. Yaqub, Phys. Rev. Letters 15, 773 (1965).
- 14. K. W. Taconis and R. de. Broyn Ouboter, <u>Progress in Low Temp. Physics</u> Vol. IV, C. J. Gorter, editor (North-Holland Publishing Co., Amsterdam, 1964), p. 38.

- 15. H. London, G. R. Clark, E. Mendoza, Phys. Rev. <u>128</u>, 1992 (1962).
- 16. R. Radebaugh, NBS Technical Note 362.
- 17. J. C. Wheatley, <u>Progress in Low Temp. Physics</u> Vol. VI,
  C. J. Gorter, Editor (North-Holland Publishing Co.,
  Amsterdam, 1970) p. 77.
- 18. W. E. Keller, Helium 3 and Helium 4 (Plenum Press, New York, 1969).
- H. E. Hall, P. J. Ford, K. Thompson, Cryogenics 6,
   80 (1966).
- 20. O. E. Vilches and J. C. Wheatley, Phys. Letters <u>24A</u>, 440 (1967); 25A, 344 (1967).
- 21. J. C. Wheatley, Am. J. Phys. 36, 181 (1968).
- 22. J. C. Wheatley et al., J. Low Temp. Phys. 4, 1 (1971).
- 23. Lansing Research Corporation, 705 Willow Avenue, Ithaca, New York, 14850.
- 24. L. E. DeLong et al., Rev. Sci. Instr. 42, 147 (1970).
- 25. J. C. Wheatley, O. E. Vilches, and W. R. Abel, Physics 4, 1 (1968).
- 26. H. Sheinberg and W. A. Steyert, Los Alamos Scientific Laboratory Report LA-4259-MS.
- 27. G. L. Pollack, Rev. of Mod. Phys. 41, 48 (1969).
- 28. Norton Vacuum Equipment Division, Newton, Mass.
- 29. Furane Plastics, Inc., Los Angeles, Calif., 90039.
- 30. A. C. Mota, Rev. of Sci. Instr. 42, 1541 (1971).
- 31. R. J. Commander and C. B. P. Finn, J. Physics E: Sci. Instr. <u>3</u>, 78 (1970).

- 32. A. C. Anderson, R. E. Peterson and J. E. Robichaux, Rev. of Sci. Instr. 41, 4 (1970).
- 33. T. I. Smith, J. Appl. Phys. 44, 852 (1973).
- 34. B. D. Josephson, Physics Letters 1, 251 (1962).
- 35. SHE Corporation, 3422 Tripp Court, Suite B, San Diego, California, 92121.
- 36. A complete description of the SQUID system will be presented in the Ph.D. thesis of Gary L. Neiheisel. The basic design and operational characteristics of a SQUID system is explained in a paper by R. P. Giffard, R. A. Webb, and J. C. Wheatley, J. Low Temp. Phys. 6, 533 (1972) and in references therein.
- 37. A. C. Anderson, J. Appl. Phys. 39, 5878 (1968).
- 38. W. R. Abel and J. C. Wheatley, Phys. Rev. Letters 21, 597 (1968).
- 39. R. A. Webb et al., Phys. Letters, 41A, 1 (1972).
- 40. CR-100 <sup>3</sup>He gas-filled germanium resistor. CryoCal Inc., P.O. Box 10176, 1371 Avenue "E", Riviera Beach, Florida, 33404.
- 41. MKS Baratron pressure meter-type 77, MKS Instruments
  Inc., Burlington, Mass.
- 42. R. H. Sherman <u>et al.</u>, J. Res. Natl. Bur. Std., <u>68A</u>, 579 (1964).
- 43. Abraham et al., Phys. Rev. 187, 273 (1969).
- 44. J. E. Falk, <u>Porphyrins and Metalloporphyrins</u> (Elsevier Publishing Company, 1964)

- 45. P. Rothemund and Amel R. Menotti, JACS 63, 267 (1941).
- 46. P. Rothemund et al., JACS 70, 1808 (1948).
- 47. Strem Chemicals Inc., 150 Andover Street, Danvers, Mass., 01923.
- 48. E. B. Fleischer et al., JACS 86, 2342 (1964).
- 49. E. B. Fleischer, JACS 85, 1353 (1963).
- 50. D. J. E. Ingram et al., JACS 78, 3545 (1956).
- 51. J. M. Assour, J. Chem. Phys. 43, 2477 (1965).
- Quantum Mechanics (Academic Press, 1969); also

  F. Basolo and R. Johnson, Coordination Chemistry

  (W. A. Benjamin, Ind., 1964).
- 53. G. E. Pake, <u>Paramagnetic Resonance</u> (W. A. Benjamin, Inc., New York, 1962).
- 54. W. Low, <u>Paramagnetic Resonance in Solids</u>, Seitz and Turnbull, Editors (Academic Press, 1960).
- 55. P. T. Manoharan and M. T. Rogers, in <u>Electron Spin</u>
  Resonances of Metal Complexes (Plenum Press, 1969).
- 56. A. Abragam and M. H. L. Pryce, Proc. Roy. Soc. (London)
  A205, 135 (1951).
- 57. B. Bleaney, Phil. Mag. 42, 441 (1951).
- 58. P. H. E. Meijer, Phys. Rev. B, 6, 214 (1971).
- 59. W. P. Pratt, Jr., Michigan State University, private communication.
- 60. J. H. Van Vleck, J. Chem. Phys. 5, 320 (1937).
- 61. J. M. Daniels, Proc. Phys. Soc. (London) A64, 673 (1953).

- 62. D. De Klerk, Handbuch der Physik, Vol. 15 (1956), p. 117.
- 63. To be published: A 4.47 mg single crystal of the compound CaCu(OAc)<sub>4</sub>·6H<sub>2</sub>O has been studied in crystalline form and found to remain in thermal equilibrium below 10 mK.
- 64. R. De Bruyn Ouboter and A. Th. A. M. De Waele, <u>Progress</u>
  <u>in Low Temperature Physics</u> Vol. VI (North-Holland
  Publishing Co., Amsterdam, 1970), p. 243.
- 65. A. H. Silver and J. E. Zimmerman, Phys. Rev. <u>157</u>, 317 (1967).
- 66. J. E. Zimmerman, P. Theine, and J. T. Harding, J. Appl. Phys. 41, 1572 (1970).
- 67. R. M. White, Quantum Theory of Magnetism, (Mc Graw-Hill 1970), p. 44.
- 68. J. R. Peverley, J. Computational Physics 7, 83 (1971).



#### APPENDIX A

#### THERMAL RELAXATION WITHIN THE MIXING CHAMBER

A calculation of the thermal relaxation times for heat flow between the CMN thermometer and sample positions in each tail was carried out while designing the refrigerator's mixing chamber. The feasibility of using the dual tail arrangement, which allows for a compact system, depends critically on the rate at which the refrigerator can come into thermal equilibrium at low temperatures. It was assumed for purposes of this calculation that heat was applied to one tail and then allowed to flow so as to establish thermal equilibrium with the other tail. The conduction of heat between the two tails can be approximately assumed to occur in two parallel paths, one through the dilute solution and concentrated <sup>3</sup>He, and the other through the copper coil foil which surrounds each sample chamber and forms a continuous path between them via the resistance thermometer mounting parts (see Figure 6). A "circuit" diagram is presented in Figure A.1 which represents each impedance to heat flow as a thermal resistance. The thermal relaxation time for heat flow through a material can be expressed as  $\tau$  = RC where R is the thermal resistance of the path and C is the heat capacity of the material.

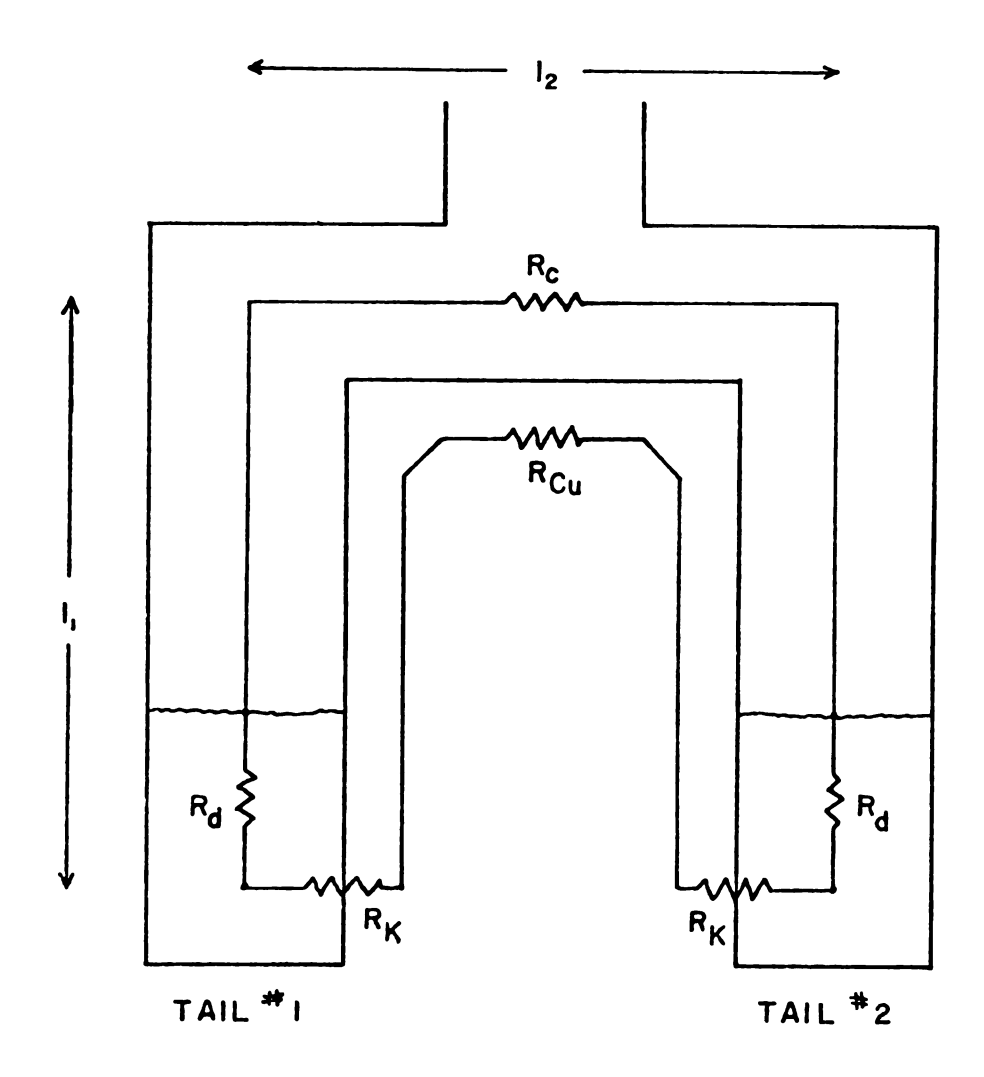


Figure A.1. A "circuit diagram" representing thermal resistance to heat flow between the two tails of the mixing chamber. Path A refers to heat flow through the liquid  $(R_d-R_c-R_d)$  and path B to heat flow through the coil foil  $(R_K-R_{cu}-R_K)$ .

The calculation is by no means exact but is a rough overestimation of the thermal equilibrium problems one might expect from this mixing chamber design. The flow of <sup>3</sup>He through the mixing chamber has been ignored in this calculation. The time necessary for the <sup>3</sup>He atom within the mixing chamber to be replenished by the incoming flow of liquid <sup>3</sup>He during cooling is also a measure of the thermal equilibrium times of this refrigerator. The thermal relaxation process acting to bring the two tails into equilibrium occurs simultaneously with the cooling at the phase boundaries as <sup>3</sup>He is circulated. Thus in reality the total thermal equilibrium time is a function of both these processes.

We will first consider the flow of heat through the liquid helium. From the heat flow diagram we see that there are effectively three paths in series,  $R_d^-R_c^-R_d^-$ , where the subscripts represent dilute solution and concentrated  $^3$ He, respectively. The worst possible case in the low temperature region, where the major heat flow is through the liquid, is obtained by assuming the entire region is filled with dilute solution. This is true because the dilute solution's thermal conductivity is smaller than the thermal conductivity of the concentrated  $^3$ He at very low temperatures. It is also assumed that the heat capacity of the entire volume of dilute solution within the mixing chamber will contribute

to the thermal relaxation time. Therefore all the dilute solution is treated as if it were located at the sample positions. This is obviously an overestimate of the true situation. The relaxation time for path A can then be expressed as:

$$\tau_{A} = R_{d}C_{d}$$

$$= \left(\frac{2\ell_{1}n_{1}}{A_{1}} + \frac{\ell_{2}n_{2}}{A_{2}}\right) \left(\frac{C_{d}}{K_{d}}\right)$$

where  $K_d$  is the thermal conductivity of the dilute solution and  $C_d$  is its heat capacity per mole of solution. The ratios  $\ell_1/A_1$  and  $\ell_2/A_2$  are the length to cross-sectional area ratios of the different regions connecting the two tails. The number of moles of dilute solution present in each region  $(n_1,n_2)$  must be estimated. At low temperatures the  $^3$ He concentration  $(\chi_3 = \frac{n_3}{n_3 + n_4})$  in the dilute solution is small  $(\sim .064)$  so we can approximate the number of moles of dilute solution by its maximum value  $^{25}$ :

$$n_1 \approx \frac{v_1}{v_{4,0}}$$

and identically

$$n_2 \approx \frac{v_2}{v_{4,0}}$$

where  $v_{4,0} = 27.6 \text{ cm}^3/\text{mole}$  is the limit of the molar volume of  $^4\text{He}$  at T = 0.0K and  $V_1$  and  $V_2$  are the volumes of regions

1 and 2, respectively. Combining these results gives us an expression for the relaxation time for heat flow through the liquid:

$$\tau_{A} = \frac{2\ell_{1}^{2} + \ell_{2}^{2}}{v_{4,0}} \quad (\text{cgs units})$$

The values of the molar specific heat and thermal conductivity have been experimentally measured in the range 3 mK to 250 mK, and were obtained from graphical presentations of this data 17.

The second path of heat flow must include the effects of Kapitza resistance between the dilute solution and copper coil foil ( $R_{K}$ ) and thermal resistance along the coil foil path between the tails. The total series resistance is:

$$R = 2R_{K} + R_{Cu}$$

An estimation of the thermal time constant associated with heat flow along this path B can be expressed as:

$$\tau_{B} = (2R_{K} + R_{Cu})C_{d}$$

where  $\mathbf{C}_{\mathbf{d}}$  is the heat capacity of the dilute solution in the mixing chamber region. This heat capacity, being much larger than the coil foil's heat capapity, effectively determines the rate of heat flow along this path.

The Kapitza resistance between copper and dilute solution has been measured and can be formulated as: 25

$$R_{K} = 1.5 \times 10^{-5}/AT^{3}$$

where A is the contact area.

The resistance to heat flow within the copper is:

$$R_{Cu} = \ell/A'K_{Cu}$$

where  $\ell/A'$  is the length to area ratio of the coil foil and  $K_{Cu}$  is its thermal conductivity. For temperature less than 1 K we can assume  $K_{Cu} \stackrel{\sim}{\sim} 1.4 \times 10^7 T$  (erg/sec-cm-K).

Using the same procedure as before to evaluate the number of moles of dilute solution within the sample chamber leads to an expression for the thermal relaxation time associated with this path in terms of the dilute solution's heat capacity:

$$\tau_{\rm B} = (\frac{3 \times 10^{-5}}{{\rm AT}^3} + \frac{\ell}{{\rm A'K_{Cu}}}) \frac{{\rm V_1}}{{\rm V_{4,0}}} {\rm C_d}$$

The results of these calculations can now be combined into a single expression for the total relaxation time for heat flow between the tails. By using the appropriate dimensions for our mixing chamber we find:

$$\tau_A = 3.8 \, C_d / K_d$$

and

$$\tau_{\rm B} = (\frac{2.1 \times 10^{-5}}{{
m T}^3} + \frac{5.6 \times 10^{-5}}{{
m T}}) \quad c_{\rm d}$$

Since the two paths are in parallel, the total relaxation time for heat flow between the two tails can be found from

$$\frac{1}{\tau} = \frac{1}{\tau_{A}} + \frac{1}{\tau_{B}}$$

The result was presented in Figure 7. As has been mentioned, the presence of two phase lines, one in each tail, means that each tail is cooling simultaneously and we therefore have overestimated the problem of thermal resistance. In practice one must distinguish between thermal relaxation and the rate at which cold <sup>3</sup>He passes through the mixing chamber as it is cooled. Typically we find that at temperatures near 10 mK it may take roughly two hours for the mixing chamber to cool from one temperature to another. However, the maximum relaxation time for this mixing chamber seems to be only on the order of one hour. This calculation indicates, and indeed it has been observed, that this design presents no thermal equilibrium problems.

APPENDIX B

## APPENDIX B

# THEORY OF POINT CONTACT SQUIDS

The phenomena of superconductivity can be explained as a condensation of electron pairs (Cooper pairs) into a single quantum state  $^{64}$ . A superconducting region can then be described by a complex order parameter,  $\psi(\mathbf{r},t) = \psi_{0}(\mathbf{r},t)$   $\mathrm{e}^{\mathrm{i}\theta}$ , where  $|\psi_{0}(\mathbf{r},t)|^{2}$  is the supercurrent charge density and  $\theta$  is the quantum mechanical phase. If one is dealing with a superconducting loop, the condition of single-valuedness of the order parameter requires that the integral of its phase around the loop must be  $2\pi n$ , where n is an integer. This implies a quantization of the total flux ( $\phi$ ) trapped within the loop, and indeed this flux is found to be quantized in units of  $\phi_{0} = h/2e$ .

The usefulness of a circuit element consisting of a superconducting loop closed by a point contact junction (weak link) in magnetometry lies in its ability to pass a supercurrent  $(i_s)$  which is a function of the phase difference  $(\Delta\theta)$  across the junction. Since any such junction will also have an associated resistance and capacitance, there is in general also a normal current  $(i_n)$  and a displacement current  $(i_d)$  through the junction. The SQUID built for this refrigerator is an rf-biased single-junction device which uses a pointed niobium screw contact to provide the weak link in a superconducting loop. The low inductance junction produced

by this contact is useful in low frequency applications. The low frequency mode of operation is characterized by the supercurrent being the dominant current in the junction. For this condition the total current becomes  $i = i_C \sin \theta$  where  $i_C$  is the critical supercurrent for the junction. It can be shown that the total flux change through the loop is related to the external flux applied perpendicular to the loop by the expression  $^{65}$ :

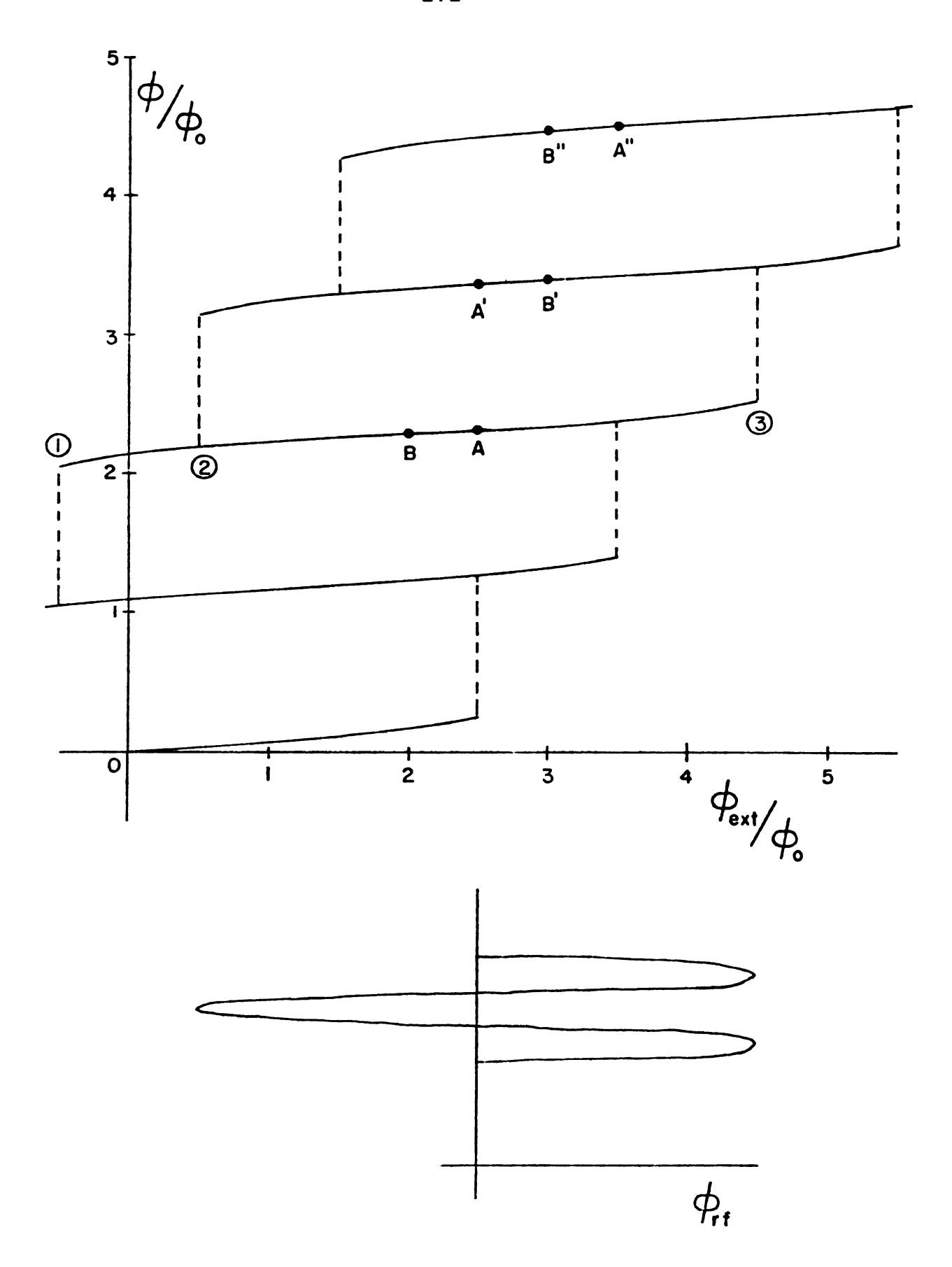
Lic 
$$\sin \frac{2\pi}{\phi_O} (\phi + k\phi_O) = \phi - \phi_{ext}$$

where  $k\phi_0 = 0$ ,  $\pm \phi_0$ ,  $\pm 2\phi_0$  ... This response function follows from the quantization of the integral of the canonical momentum of a Cooper pair around the loop (again the condition for single-valuedness of the wave function).

Under the normal operating conditions of an rf-biased circuit, which is characterized by the requirement that  $2\pi \text{Li}_{\text{C}}/\phi_{\text{O}}$  be greater than one, the response is as shown in Figure B.1. This type of response is obtained by adjusting the niobium screw contact tension until the critical current meets the above criteria. The dotted lines indicate transitions corresponding to single flux quantum shifts ( $\Delta k = \pm 1$ ) which occur when the critical flux, or critical current, is reached in the loop.

In order for this device to be useful, one must be able to measure the flux changes introduced into the superconducting loop from the magnetized sample via the signal coil. Figure B.1. The response function of a SQUID magnetometer.

The total flux (\$\phi\$) through the superconducting loop is plotted as a function of the external applied field.



This is accomplished by inductively coupling the loop to a tank circuit which is resonant at the rf signal frequency 66,36. As the rf current amplitude in the inductor is increased, the superconducting loop will set up an opposing field by the creation of a supercurrent within the loop.

Suppose the dc flux level in the loop is at point A in Figure B.1. As the rf flux amplitude about point A is increased the rf voltage across the tank circuit increases linearly until the rf amplitude reaches A-3 at which the rf voltage will be  $V_{A}$ . At this point an irreversible transition occurs. The energy required for this transition is drawn from the tank circuit with a resulting decrease in the rf oscillation level. This process repeats itself as long as the rf drive is insufficient to overcome the loss in energy per rf cycle due to the traversing of one hysteresis loop. In this region of operation the rf voltage is no longer a linear function of rf current amplitude, but is approximately constant at  $\mathbf{V}_{\mathbf{A}}$ . Now assume the dc flux level is at B. The same process as before occurs except that now the maximum critical flux level will be reached when the rf flux amplitude equals B-3 and an irreversible transition about two hysterises loops occurs. The maximum voltage across the tank circuit at this point will be  $V_{R} > V_{A}$ . The distance B-A represents one-half of a flux quantum  $(\phi_0/2)$ . Since the points A and A', B' and B", etc. are equivalent points in the response function, it is apparent that the maximum voltage across the rf tank circuit is periodic in the dc flux level with period  $\phi_{0}$ . One can therefore utilize this property to measure the dc flux change through the loop.



### APPENDIX C

# THEORETICAL CALCULATION OF THE MAGNETIC SUSCEPTIBILITY OF CUTPP

We have seen that the spin hamiltonian which describes the energy of the paramagnetic copper ion at the ith site in a crystal of CuTPP is:

$$H_{i} = g_{||}^{\mu S} z_{i}^{H} z + g_{\perp}^{\mu} (S_{x_{i}}^{H} x + S_{y_{i}}^{H} y) + AS_{z_{i}}^{I} z_{i}$$

$$+ B(S_{x_{i}}^{I} x_{i} + S_{y_{i}}^{I} y_{i}) + \sum_{j}^{\prime} H_{ij}$$

$$\text{where } H_{ij} = \frac{(\underbrace{\mu_{i} \cdot \mu_{j}}) - 3(\underbrace{\mu_{i} \cdot \hat{r}_{ij}})(\underbrace{\mu_{j} \cdot \hat{r}_{ij}})}{r_{ij}}$$

The total spin hamiltonian for the crystal is simply  $H = \sum_{i} H_{i}$ . It will be useful to write the single ion spin hamiltonian in the form:

$$H_{i} = H_{z_{i}} + H_{o_{i}} + H_{d_{i}}$$

where  $H_{z_i}$  refers to the Zeeman term,  $H_{o_i}$  is the hyperfine interaction and  $H_{d_i}$  represents the intermolecular classical dipole-dipole coupling. The zero-field magnetic susceptibility along the  $\alpha$ th axis can be obtained from the partition

function for this system. The exact partition function is:

$$Z = \operatorname{tr} e^{-\beta H}$$

$$= \operatorname{tr} e^{-\beta i} (H_{o_i} + H_{z_i} + H_{d_i})$$

and the zero-field susceptibility is obtained from the well-known expression:

$$\chi_{\alpha} = \lim_{\mathbf{H}_{\alpha} \to \mathbf{O}} \frac{1}{\beta \mathbf{V}} \frac{\partial^{2} (\ln \mathbf{Z})}{\partial \mathbf{H}_{\alpha}^{2}}$$

where  $\alpha = x$ , y, or z axis.

In practice, one finds that it is impossible to find a basis which is composed of eigenstates of the total hamiltonian. Therefore the evaluation of the trace involves more than a simple sum of diagonal elements. In fact the dipolar coupling term guarantees that no such basis can be found. Since the susceptibility cannot be calculated in closed form with this hamiltonian, one must assume the dipole coupling is a perturbation and expand the partition function. A particularly good method for many applications is to expand the partition function in powers of the applied magnetic field and retain only terms to first order in the dipolar interaction. Of course only the terms to order  $H_Z^2$  should contribute to the zero-field susceptibility because of the second derivative which is involved in its derivation.

Another method which is closely related to the previous one involves expanding the expectation value of the magnetization in an identical manner. The advantage of this method lies in the fact that it is only necessary to expand the magnetization to first order in the applied field to obtain the susceptibility. The magnetization of the crystal can be expressed as:

$$M_{\alpha} = -g_{\alpha} \mu < \sum_{i} S_{i\alpha} >$$

where  $\mu$  is the Bohr magneton and  $g_{\alpha}$  is the appropriate component of the g-tensor. The zero-field magnetic susceptibility is then obtained from the first derivative of this quantity:

$$\chi_{\alpha} = \lim_{H_{\alpha} \to 0} \frac{\partial M_{\alpha}}{\partial H_{\alpha}}$$

In order to see how this expansion may be carried out, consider a general operator of the form  $e^{-\beta(A+B)}$  where A and B are two operators which may not commute. Also assume that B is small compared to A. We can expand this exponential operator in powers of B by the following procedure. We can express this operator as:

$$e^{-\beta(A+B)} = e^{-\beta A}\phi(\beta)$$

where  $\phi(\beta)$  is a function of B, which can be written in a manner that initially seems to complicate the issue, but will prove useful:

$$\phi(\beta) = e^{\beta A} e^{-\beta (A+B)}$$

The derivative of  $\phi(\beta)$  with respect to  $\beta$  can be used to derive a recursion relation for the expansion of  $\phi(\beta)$  in powers of B:

$$\frac{d\phi(\beta)}{d\beta} = -e^{\beta A} B e^{-\beta(A+B)}$$

= 
$$-B(\beta) \phi(\beta)$$

where  $B(\beta) = e^{\beta A} B e^{-\beta A}$ . Integrating this equation and recognizing that  $\phi(0) = 1$  will give the result:

$$\phi(\beta) = 1 - \int_{0}^{\beta} B(s) \phi(s) ds$$

which is the recursion relation for an expansion of  $\phi(\beta)$  in powers of B.

This expansion can now be applied to the expectation value of the spin operator where the terms  $H_{z_i}$  and  $H_{d_i}$  are considered to be small. The expansion and evaluation of the appropriate matrix elements will be carried out in the basis defined by the eigenstates of  $H_{o_i}$ . The small term approximation is valid for the zero field limit because  $H_{z_i}$  is a

linear function of the applied magnetic field and  $H_{d_1}$  involves the dipolar coupling interaction energy which is much smaller than the hyperfine interaction energy. Assuming the applied field to be along the  $\alpha$  axis (i.e.  $H_{z_1} = g_{\alpha} \mu H_{\alpha} s_{\alpha}$ ) the expansion can be shown to yield:

Only terms to first order in the field and to first order in the dipole interaction which contribute to the susceptibility have been kept. Due to the requirement that there be no net spontaneous moment, all terms which are odd in spin operators will be zero. The first term in this expansion represents the susceptibility with only the hyperfine and Zeeman interactions present, and the other terms represent the first order perturbative effect of the dipolar coupling.

The simplification that can be made by utilizing this expansion over an expansion involving the partition function is apparent from the fact that lower order terms are sufficient for the calculation of the susceptibility (i.e.  $O(H_{\alpha})$  instead of  $O(H_{\alpha}^2)$ ). Once this expansion has been obtained, the remainder of the calculation involves evaluating the trace over the eigenstates of  $H_{\alpha}$ . The eigenstates of  $H_{\alpha}$  can be constructed from linear combinations of the well-known eigenstates of  $S_{\alpha}$  ( $\frac{1}{2} \pm m_{\alpha}$ ,  $\frac{1}{2} \pm m_{\alpha}$ ), where  $m_{\alpha} = \frac{1}{2}$ ,  $m_{\alpha} = \frac{1}{2}$ ,  $m_{\alpha} = \frac{1}{2}$ . First the hyperfine interaction is written in terms of raising and lowering operations and its matrix elements in this basis are determined:

$$H_{o_i} = A S_{z_i} I_{z_i} + \frac{B}{2} (S_{+_i} I_{-_i} + S_{-_i} I_{+_i})$$

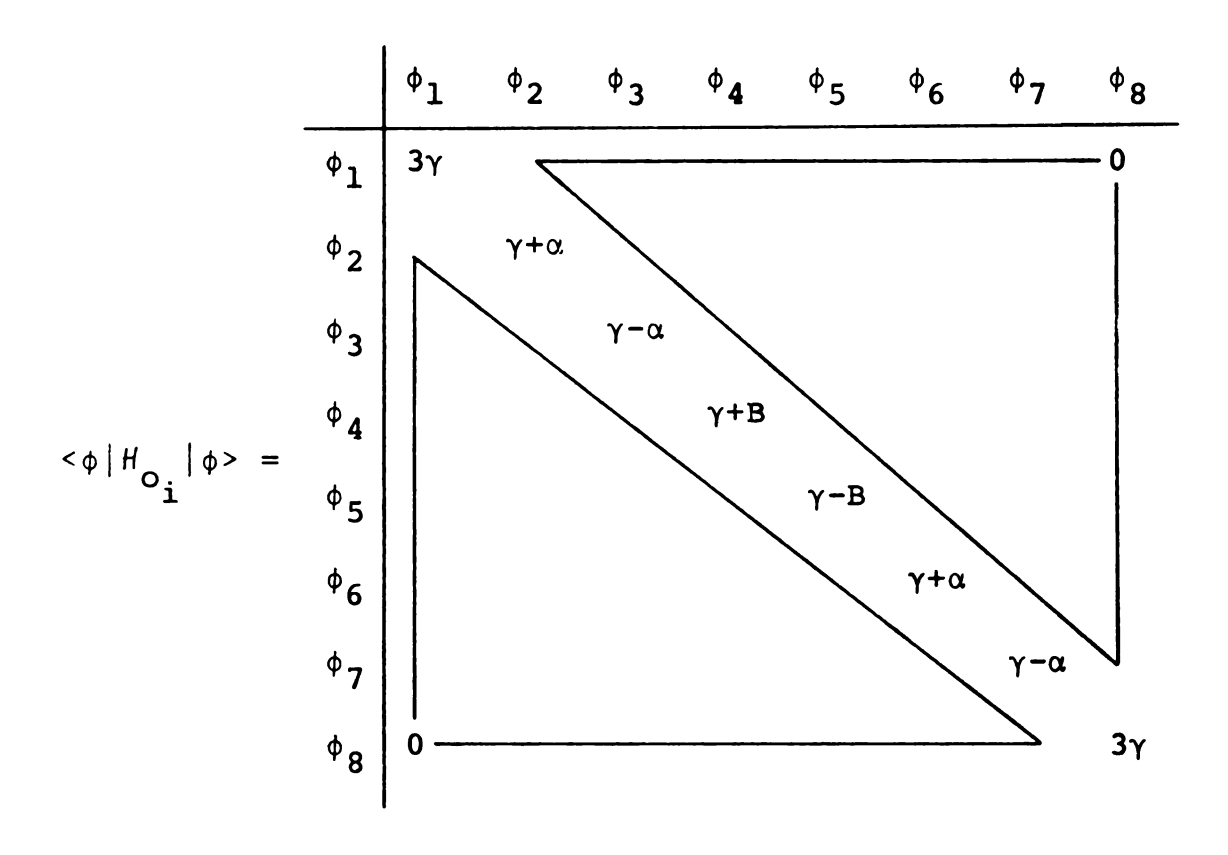
and

$$S \pm |m_s, m_I\rangle = [S(S+1) - m_s(m_s \pm 1)]^{\frac{1}{2}} |m_s \pm 1, m_I\rangle$$

$$I \pm |m_s, m_I\rangle = [I(I+1) - m_I(m_I \pm 1)]^{\frac{1}{2}} |m_s, m_I \pm 1\rangle$$

From an appropriate arrangement of this basis one can form three 2 x 2 subspaces and two 1 x 1 subspaces along the diagonals of the matrix. The entire matrix can no be diagonalized by individually diagonalizing each subspace. The eigenstates of this newly formed matrix comprise the

the desired basis which diagonalizes the hyperfine interaction. One should obtain:



where:

$$\phi_1 = |1/2,3/2\rangle$$

$$\phi_2 = \frac{1}{\sqrt{2\alpha(\alpha+A/2)}} \left\{ \frac{3B^2}{4} \left[ -1/2, 3/2 \right] + (\alpha+A/2) \left[ 1/2, 1/2 \right] \right\}$$

$$\phi_3 = \frac{1}{\sqrt{\frac{2\alpha(\alpha+A/2)}{2\alpha(\alpha+A/2)}}} \{ (\alpha+A/2) | -1/2, 3/2 > \frac{3B^2}{4} | 1/2, 1/2 > \}$$

$$\phi_4 = \frac{1}{\sqrt{2}} \{ |-1/2,1/2\rangle + |1/2,-1/2\rangle \}$$

 $\alpha = \frac{1}{2} (A^2 + 3B^2)^{\frac{1}{2}}$ 

$$\phi_5 = \frac{1}{\sqrt{2}} \{ |-1/2, 1/2\rangle - |1/2, -1/2\rangle \}$$

$$\phi_6 = \frac{1}{\sqrt{2\alpha(\alpha+A/2)}} \{ (\alpha+A/2) |-1/2, -1/2\rangle + \frac{3B^2}{4} |1/2, -3/2\rangle \}$$

$$\phi_7 = \frac{1}{\sqrt{2\alpha(\alpha+A/2)}} \{ \frac{3B^2}{4} |-1/2, -1/2\rangle - (\alpha+A/2) |1/2, -3/2\rangle \}$$

$$\phi_8 = |-1/2, -3/2\rangle$$
and  $\gamma = A/4$ 

One can now utilize this basis by expanding the formal trace operation into a sum over the eigenstates of  $\mathcal{H}_{O_i}$ . Although this expansion can rapidly become very complicated, especially when evaluating the term involving the dipolar coupling, the calculation can be carried through to obtain the susceptibility results presented on page 122. It is useful for the purposes of this calculation to express the dipolar coupling interaction in terms of raising and lowering operations  $^{67}$ . For each calculation, the perturbative term will separate into a product the original unperturbed susceptibility  $(\chi_{O_i})$  and  $(\chi_{O_i})$ , and a lattice summation of the dipole interaction over the crystal  $(\Delta_i)$  and  $(\Delta_i)$ .

The lattice summations were carried out over the CuTPP crystal lattice within a spherical region centered about the ith site using the method proposed by J. R. Peverely<sup>68</sup>. His technique involves using a convergence factor to enhance the convergence of the lattice summation without having to carry the calculation over an extremely large number of unit cells. The summation was carried out over several different radii to ensure that covergence had been obtained. The results indicated the lattice summations had converged correctly.

The effect of the superhyperfine coupling has not yet been determined in detail. This calculation rapidly becomes extremely complicated and one must resort to the more powerful Laplace transform computation technique presented by P.H.E. Meijer<sup>58</sup>. Despite using this technique we have only been able to estimate the superhyperfine coupling effect in the special case of B=0 along the parallel and perpendicular axes.

APPENDIX D

## APPENDIX D

## TABULATION OF PERTINENT DATA

The measurement of temperature within the dilution refrigerator is intimately connected with the CR-100 germanium resistor. The results of a careful calibration of this resistor over the temperature range .3K to 3.0K is tabulated in this appendix. Also, the experimental magnetic susceptibility data obtained for copper tetraphenylporphine is presented here. Both the raw experimental data and the single crystal data after application of the demagnetization corrections has been tabulated. The effective powder susceptibility as calculated from the demagnetization corrected data is also listed.

Table D.1. Results of the CR-100 Germanium Resistor Calibration.

B - = ! = !	*	<b>.</b>	*
Resistance	Inverse T	Resistance	Inverse T
(ohms)	(K <sup>-1</sup> )	(ohms)	(K <sup>-1</sup> )
207.1	.312	2054.2	1.439
231.1	.348	2323.1	1.512
256.2	. 385	2626.2	1.584
282.8	.421	2966.4	1.657
310.5	.457	3351.2	1.730
339.3	.494	3785.5	1.802
370.1	.530	4276.5	1.875
402.3	.566	4832.7	1.948
436.3	.603	5465.0	2.020
471.6	.639	6180.0	2.093
510.2	.675	6989.7	2.166
549.8	.712	7906.7	2.239
592.0	.748	8946.3	2.311
636.3	.785	10,123.0	2.384
683.2	.821	11,464.0	2.457
732.1	.857	12,977.0	2.529
783.5	.894	14,706.0	2.602
839.6	.930	16,661.0	2.675
898.0	.966	18,882.0	2.747
959.6	1.003	21,383.0	2.820
1094.0	1.075	24,260.0	2.893
1244.3	1.148	27,505.0	2.966
1413.5	1.221	31,120.0	3.038
1603.1	1.293	35,210.0	3.111
1816.5	1.366		

Table D.2. The Magnetic Susceptibility Data for CuTPP-Single Crystal, Parallel Axis (Not Corrected
for Demagnetization Effects)

.6 mg Single Crystal		1.25 mg Single Crystal	
ХII	Inverse T*	xII	Inverse T
(emu/mole)	$(K^{-1})$	(emu/mole)	(K <sup>-1</sup> )
.725	1.634	.390	.874
.738	1.662	.471	1.067
.864	1.964	.546	1.243
1.000	2.256	.707	1.583
1.098	2.483	.839	1.881
1.242	2.798	1.007	2.258
1.343	3.042	1.192	2.693
1.532	3.468	1.186	2.682
2.183	4.989	1.226	2.769
4.613	10.526	1.316	2.966
5.974	13.737	1.510	3.401
7.663	17.746	2.271	5.118
9.610	22.571	3.965	8.978
12.745	30.718	6.165	14.044
16.898	42.122	11.169	26.111
20.023	51.964	15.953	38.793
22.303	59.388	23.890	62.946
24.942	68.829	31.544	93.333
26.324	74.370	31.905	96.159
27.623	79.384	34.977	109.550
28.706	83.291	40.004	137.910
30.406	90.394	40.465	140.290
33.343	102.980	42.882	164.130
35.262	113.050		
41.621	151.670		
43.122	170.720		
43.744	177.300		
44.339	183.960		

Table D.3. The Magnetic Susceptibility Data for CuTPP-Powder and Single Crystal, Perpendicular Axis
(Not Corrected for Demagnetization Effects)

1.25 mg Single Crystal		<u>Powder</u>	
$x_\perp$	Inverse T*	X <sub>pow</sub>	Inverse T*
(emu/mole)	(K <sup>-1</sup> )	(emu/mole)	$(\kappa^{-1})$
.602	1.656	.233	.584
.644	1.793	.290	.732
.740	2.042	.354	.892
<b>. 7</b> 85	2.186	.665	1.670
.897	2.490	.769	1.928
.970	2.695	.883	2.218
1.034	2.862	1.003	2.521
1.123	3.105	1.045	2.629
1.118	3.093	1.132	2.849
1.357	3.816	1.990	5.021
1.294	3.590	2.147	5.436
1.821	4.931	3.971	10.214
3.129	8.924	7.730	20.276
4.961	14.020	7.910	20.728
6.855	19.387	11.332	30.999
9.082	26.400	14.452	41.357
11.999	36.984	16.853	51.506
14.966	51.080	19.817	66.094
16.612	62.346	22.555	83.358
17.987	75.443	24.313	96.711
18.969	93.526	25.793	110.310
19.299	110.800	28.657	140.580
19.287	135.380	31.291	170.880
19.242	146.130	33.013	191.510
19.104	167.430	34.955	224.600
18.740	186.470	35.497	233.840

Table D.4. The Magnetic Susceptibility Data for CuTPP-Single Crystal, Parallel Axis, (Corrected for
Demagnetization Effects)

.6 mg Single Crystal		1.25 mg Single Crystal	
x	Inverse T*	×II	Inverse T*
(emu/mole)	(K <sup>-1</sup> )	(emu/mole)	$(\kappa^{-1})$
.726	1.634	.390	.874
.739	1.662	.471	1.067
.866	1.964	.546	1.243
1.002	2.256	.708	1.583
1.101	2.483	.840	1.881
1.245	2.798	1.008	2.258
1.347	3.042	1.194	2.693
1.537	3.468	1.188	2.682
2.194	4.989	1.228	2.769
4.661	10.526	1.318	2.966
6.054	13.737	1.513	3.401
7.796	17.746	2.277	5.118
9.819	22.571	3.985	8.978
13.116	30.718	6.213	14.044
17.554	42.122	11.327	26.111
20.954	51.964	16.278	38.793
23.465	59.388	24.625	62.946
26.404	68.829	32.839	93.333
27.958	74.370	33.230	96.159
29.428	79.384	36.576	109.550
30.660	83.291	42.110	137.910
32.607	90.394	42.621	140.290
36.008	102.980	45.311	164.130
38.257	113.050		
45.858	151.670		
47.687	170.720		
48.449	177.300		
49.180	183.960		

Table D.5. The Magnetic Susceptibility Data for CuTPP-Powder and Single Crystal, Perpendicular
Axis (Corrected for Demagnetization Effects)

1.25 mg Single Crystal		Powder	
xΤ	Inverse T*	$\chi_{ t pow}$	Inverse T*
(emu/mole)	$(K^{-1})$	(emu/mole)	(K <sup>-1</sup> )
.601	1.656	.233	.584
.643	1.793	.290	.732
.739	2.042	.354	.892
.784	2.186	.665	1.670
.895	2.490	.769	1.928
.968	2.695	.883	2.218
1.031	2.862	1.003	2.521
1.120	3.105	1.045	2.629
1.145	3.093	1.132	2.849
1.352	3.816	1.990	5.021
1.290	3.590	2.147	5.436
1.812	4.931	3.971	10.214
3.103	8.924	7.730	20.276
4.897	14.020	7.910	20.728
6.734	19.387	11.332	30.999
8.870	26.400	14.452	41.357
11.632	36.984	16.853	51.506
14.399	51.080	19.817	66.094
15.916	62.346	22.555	83.358
17.175	75.443	24.313	96.711
18.068	93.526	25.793	110.310
18.367	110.800	28.657	140.580
18.356	135.380	31.291	170.880
18.315	146.130	33.013	191.510
18.190	167.430	34.955	224.600
17.859	186.470	35.497	233.840

Table D.6. The Effective Powder Susceptibility as

Determined by the Demagnetization Corrected

Single Crystal Data

.6 mg Single Crystal		1.25 mg Single Crystal		
eff.	Inverse T	eff.	Inverse T	
$\chi_{pow}$	_	$\chi_{pow}$	_	
(emu/mole)	$(K^{-1})$	(emu/mole)	$(K^{-1})$	
.650	1.634	.352	.874	
.662	1.662	.427	1.067	
.780	1.964	.494	1.243	
.898	2.256	.634	1.583	
.988	2.483	.751	1.881	
1.114	2.798	.900	2.258	
1.209	3.042	1.068	2.693	
1.379	3.468	1.066	2.682	
1.978	4.989	1.100	2.769	
4.042	10.526	1.181	2.966	
5.298	13.737	1.354	3.401	
6.833	17.746	2.037	5.118	
8.627	22.571	3.477	8.978	
11.374	30.718	5.439	14.044	
14.685	42.122	9.884	26.111	
17.025	51.964	13.762	38.793	
18.601	59.388	19.266	62.946	
20.277	68.829	23.390	93.333	
21.116	74.370	23.595	96.159	
21.851	79.384	24.767	109.550	
22.400	83.291	26.743	137.910	
23.250	90.394	26.900	140.290	
24.627	102.980	27.691	164.130	
25.458	113.050			
27.923	151.670			
28.414	170.720			
28.606	177.300			
28.780	183.960			

MICHIGAN STATE UNIVERSITY
DEPARTMENT OF PHYSICS
EAST LANSING, MICHIGAN

